POLITECNICO DI MILANO
School of Industrial and Information Engineering
Master of Science in Mechanical Engineering

POLITECNICO
MILANO 1863

A numerical investigation on the impact of turbulence and combustion modeling in predicting mixing-controlled Diesel combustion

Supervisor:
Prof. Tommaso Lucchini

Master Thesis by:
Federico Ramognino
920116

Academic Year 2020-2021

Ringraziamenti

Arrivato al termine di questo mio elaborato, e di questo percorso di studi, voglio esprimere i miei più sentiti ringraziamenti a tutte le persone che mi sono state vicine in questo lungo percorso, rendendo tutto questo possibile.

In primo luogo, mi sento in dovere di ringraziare il Prof. Lucchini, che mi ha dato la possibilità di mettere alla prova le mie capacità, dandomi carta-bianca su un lavoro di discreta mole e rilevanza scientifica, e per la sua estrema disponibilità nonostante tutte le problematiche che si sono verificate in questi due lunghi anni. Vorrei inoltre ringraziare tutto il dipartimento per avere messo a disposizione i mezzi informatici che mi hanno permesso di svolgere le simulazioni.

In secondo luogo vorrei ringraziare tutta la mia famiglia, che mi è sempre stata vicina e mi ha incoraggiato e supportato in tutte le mie scelte, e a cui dedico il raggiungimento di questo mio importante traguardo.

In fine vorrei ringraziare (senza andare a fare nomi per non rischiare di scordarmi di qualcuno nell'emozione del momento) tutti i miei amici, da quelli di lunga data a tutti quelli che mi sono fatto tra le mura del Politecnico. Devo ringraziare soprattutto loro se sono riuscito ad arrivare a questo punto ancora (quasi) sano di mente.

Contents

List of Tables

List of Figures

Nomenclature

Acronyms

CAD	Crank angle degree
CFD	Computational fluid dynamics
CI	Compression ignition
CIV	Combustion Image Velocimetry
CN	Cetane Number
DPRF	Diesel Primary Reference Fuel
ECN	Engine Combustion Network
EGR	Exhaust gas re-circulation
EVC	Exhaust valve closing
EVO	Exhaust valve opening
GHG	Green-House gases
HCCI	Homogeneous Charge Compression Ignition
HDV	Heavy-Duty Vehicles
HPDI	High Pressure Direct Injection
HRR	Heat release rate
ICE	Internal combustion engine
IMEP	Indicated mean effective pressure
IVC	Inlet valve closing
IVO	Inlet valve opening
LDV	Light-Duty Vehicles
LHV	Lower Heating Value
LOL	Lift-off length
LTC	Low Temperature Combustion

KHRT	Kelvin-Helmholtz and Rayleigh-Taylor
ODE	Ordinary differential equation
PIV	Particle Image Velocimetry
PPC	Partially Premixed Combustion
PRF	Primary Reference Fuel
RCCI	Reactivity Controlled Compression Ignition
RIF	Representative Interactive Flamelet
RNG	Re-Normalization Group
SI	Spark Ignition
SR	Swirl ratio
SSE	Start of solenoid energizing
TDC	Top dead center
TKE	Turbulent kinetic energy
TWM	Tabulated Well-Mixed

Variables

c	Normalized progress variable
C	Progress variable
D	Bore
h	Enthalpy
k	Turbulent kinetic energy
l	Connecting rod length
p	Pressure
r	Compression ratio
S	Stroke
T	Temperature
$\mathbf{U}$	Eulerian velocity vector field
x_i	Molar fraction i-th specie
y_i	Mass fraction i-th specie
Z	Mixture fraction

Z''^2	Variance of mixture fraction
ϵ	Turbulent dissipation
ϕ	Equivalence ratio
μ_t	Turbulent dynamic viscosity
ρ	Density
χ	Scalar dissipation rate
$\dot{\omega}_i$	Reaction rate of i-th specie
Pr	Prandtl number
Sc	Schmidt number
We	Weber number

Abstract

In the present work, extensive investigations have been performed, via numerical simulations, to understand the combined impact of turbulence and combustion modeling in the description of mixing-controlled Diesel combustion, with a split-injection strategy. Turbulence models investigated were the standard k-ε closure and its RNG variant, while the combustion models were the Representative Interactive Flamelet (RIF) model and the Well-Mixed model with tabulation of chemical kinetics (TWM). Their performances were investigated under multiple operating conditions, assessing the sensitivity of the models to injection timing and spray structure. Moreover, the sensitivity of the RIF model to the number of flamelet domains used for the main injection event was assessed. Validation is performed through the small-bore optical diesel engine of Sandia National Laboratories, for which a wide and well-documented experimental database is available. Both turbulence and combustion models showed satisfactory results in terms of overall combustion dynamics in case of early and intermediate injection timing, while the RIF model shower poor performances with late injection. Moreover, only the TWM model was capable of describing flame development and stabilization during main injection event, even though it experienced misfire issues in pilot combustion due to inhibition of reaction rate in fuel-rich regions. The standard k-ε model showed negligible sensitivity to both injection timing and spray spreading angle, proving its poor performances in describing shear flows. The overall best results were obtained with the combination of RNG k-ε and RIF models, with a spray spreading angle of 10°. Moreover, the RIF model was not capable to reproduce flame stabilization even with multiple flamelet domains, due to the really short ignition delay in main combustion. Simulations have been performed with OpenFOAM, an open-source software for multidimensional CFD simulations, and Lib-ICE, a library of models and solvers for internal combustion engine (ICE) simulations, developed by the ICE Group of Politecnico di Milano.

Key-words: CFD, Diesel, turbulence, combustion

Sommario

Nel presente lavoro di tesi, si è svolta un'ampia indagine sull'impatto che hanno la modellazione della turbolenza e della combustione, sulla capacità di descrivere il processo di combustione in motori Diesel, in un contesto "mixing-controlled" e con iniezioni sequenziali. I modelli di turbolenza studiati sono il k-ε standard e la sua variante RNG, mentre quelli di combustione sono il Representative Interactive Flamelet (RIF) ed il Well-Mixed con tabulazione della cinetica di reazione (TWM). Si sono studiate le loro sensitività rispetto alle tempistiche di iniezione e alla struttura dello spray. Inoltre, si è studiata la sensitività del modello RIF rispetto al numero di flamelet utilizzate per descrivere la combustione principale. La validazione è stata svolta tramite il motore ottico di piccola cilindrata dei Sandia National Laboratories, per il quale è disponibile un vasto database di misurazioni sperimentali. Entrambi i modelli di turbolenza e combustione si son dimostrati capaci di riprodurre in maniera soddisfacente il processo di combustione, sebbene il modello RIF abbia mostrato prestazioni carenti in caso di iniezione ritardata. Inoltre, solamente il modello TWM è stato capace di decrivere il processo di propagazione e stabilizzazione della fiamma, sebbene abbia riscontrato problematiche durante la combustione pilota, a causa dell'inibizione del progredire delle reazioni nelle zone di miscela ricca. Il modello standard k-ε ha mostrato bassa sensitività rispetto alla tempistica di iniezione e all'angolo di apertura dello spray, provando le sue basse prestazioni nel descrivere flussi di taglio. I migliori risultati sono stati ottenuti utilizzando assieme i modelli RNG k-ε e RIF, con un angolo di apertura dello spray di 10°. Inoltre, il modello RIF non è stato capace di riprodurre la stabilizzazione della fiamma nemmeno con flamelet multiple, a causa del basso tempo di accensione della fiamma principale. Le simulazioni sono state svolte tramite OpenFOAM, un programma open-source di simulazione CFD, e Lib-ICE, una libreria di modelli e solutori per la simulazione di motori a combustione interna, sviluppata dal ICE Group del Politecnico di Milano.

Introduction

Thanks to their high power density and high efficiency, internal combustion engines (ICE) have been widely adopted as power sources in many applications, and their market share is expected to steadily grow over the next decade [1]. These can be split into two categories, depending on the strategy adopted for fuel ignition - in spark ignition (SI) engines a premixed air-fuel charge is ignited by means of an electrical discharge, while in compression ignition (CI) engines highly pressurized fuel is injected inside the cylinder at the end of compression stroke, and it achieves self-ignition thanks to the high bulk-gas temperature and pressure. Thanks to their high thermal efficiency and high torque output, the latter are widely used in several applications:

- Light-duty vehicles (LDV) - Although CI engines are characterized by generally lower power-to-weight ratio with respect to SI engines, due to the higher mechanical loads, the introduction of turbocharging and the subsequent engine downsizing allowed to sensibly reduce this gap in medium/light-duty application [30], to the point that in 2016 in the EU almost half of the LDVs registered mounted Diesel engines [40];

- Heavy-duty vehicles (HDV) - As in HDVs minimization of operating costs is more important than weight and space utilization, Diesel engines are extensively applied in this field;

- In general, Diesel engines are applied in all fields where high output power and torque are required, such as off-road heavy-duty applications (tractors, earth-moving equipment, construction machinery, mining machinery, etc.), or high thermal efficiencies due to the high operating costs, like power production, rail and naval transportation, etc.

However, since the ‘50s there have been increasing awareness of the damages caused by usage fossil fuels as energy sources - mainly the production of harmful compounds and green-house gases (GHG) - and in the last decades increasingly

strong restrictions were imposed on the quality of exhaust gases produced by ICEs. For this reason, there is strong interest in decarbonization of the transport sector and looking for more sustainable and environmentally-friendly alternatives to ICEs (electrification, power-cells, alternative fuels, etc.). Therefore, in the next years it is expected to see increasing electrification, especially in the form of hybridization with SI engines in LDVs, thanks to the high efficiencies achieved - comparable to those of equivalent CI engines - and the low level of pollutant production [31, 40]. Hence, CI are expected to progressively disappear over the next decades in LDV applications. On the other hand, the current technological limitations of batteries in terms of energy density, specific cost, and recharging time, make prohibitive the full battery electrification of heavy-duty applications, characterized by very high energy consumption over long periods of time, and Diesel engines are expected to keep their dominant role in these fields (HDVs, long-range marine transports, etc.) [31].

Therefore, strong effort shall be put in reducing the environmental impact of Diesel engines, which can be achieved by improving the following aspects [30]:

- Further reduction of the specific fuel consumption, by optimizing the overall combustion process, and achieving values of thermal efficiency over 50%;
- Development of renewable fuels, such as biodiesel or synthetic fuels (DME), to be used alone or as additives to improve combustion properties of conventional diesel fuel [37, 11];
- Development of new combustion modes able to improve the quality of exhaust gases, without affecting the overall performances. Research mainly focuses on Low Temperature Combustion (LTC) modes - like Partially Premixed Combustion (PPC) and Homogeneous Charge Compression Ignition (HCCI) - and dual fuel combustion modes - like Reactivity Controlled Compression Ignition (RCCI) and High Pressure Direct Injection (HPDI).

To achieve improvements in these fields, further research is required to have a better understanding on the several aspects involved in the combustion process, like fuel ignition, dynamics with multiple-injection strategies, the effect of piston bowl geometry, the evolution of the spray, etc. To investigate these aspects, research is based on the following tools:

- Investigations in optical engines, in which accurate optical measurements are performed thanks to a transparent piston head;
- Detailed simulations with multi-dimensional Computational Fluid Dynamic Dynamics (CFD) models.

The main limitations of the former are associated to the capability of performing optical measurements, which often requires to adopt simplified piston geometries, and the costs and time required to perform the experiments. On the other hand, CFD simulations are characterized by high versatility, which allows them to be applied both as design and diagnostic tool, to understand the mechanisms of air-fuel mixture formation, flame diffusion, and formation of pollutants.

However, CFD modeling of CI ICEs has to face an extremely high level of complexity, especially for what concerns the combustion process. Specifically, combustion modeling has to deal with the complex chemistry involved in combustion of complex hydrocarbons (two-stage ignition), and properly account for the effect of turbulence on the combustion process (turbulence-chemistry interaction), as turbulence can sensibly affect the reaction rates and flame structure in both premixed and non-premixed combustion [45, 14]. Therefore, the CFD codes require to be extensively validated, to assess their capability in describing the dynamics of the combustion process in engine applications.

The objective of this thesis is to validate two combustion models, the Representative Interactive Flamelet (RIF) model and the Well-Mixed model with tabulation of chemical kinetics (TWM), against the measurements taken in an optical engine with geometry of the combustion chamber really close to the one of real engines. The main contribution of this study is to validate the models in real engine conditions, as in the past most of experimental data were taken in constant-volume vessels - without the capability to account on the effect of piston bowl geometry - or in simplified optical engines, not fully reproducing the dynamics of real engines (impact of turbulent flow structures due to jet/wall interaction).

In the present work, extensive investigations have been performed via numerical simulations to understand the combined impact of combustion modeling and turbulence modeling in capability to predict the dynamics of combustion process in CI ICEs. Moreover, the sensitivity with respect to injection parameters has been studied, for all the models under investigation. Simulations have been performed with OpenFOAM [3], an open-source software for CFD simulations, and LibICE, a toolkit developed by the ICE Group of Politecnico di Milano in which specific models and solvers for simulation of internal combustion engines are implemented, which has been extensively validated by the developers. Results are validated through the small-bore optical diesel engine of Sandia National Laboratories, for which a wide and well documented experimental database is available on Engine Combustion Network website [2].

In chapter one, the past experimental investigations with the above mentioned

facility will be briefly described, along with the findings of some simulation studies. Then, the second chapter will be dedicated to a detailed description of the numerical models investigated in this work, with their respective strengths and weaknesses. Third chapter will be dedicated to the description of the model setup, and the critical aspects that were faced in this preliminary stage of the work. In chapter four the sensitivity of the numerical models will be investigated, by assessing the impact of turbulence modeling and combustion modeling on prediction of heat release, sensitivity to injection parameters, and other model parameters. Last chapter will summarize the most relevant considerations from the analysis performed.

Chapter 1

The experimental facility

1.1 ECN small-bore Diesel engine

The present study was developed on the basis of the extensive experimental campaign performed on a single-cylinder, small-bore optical Diesel engine of the Sandia national laboratories. Many researches have been performed to characterize the impact of piston bowl geometry on the combustion dynamics and levels enhancement of mixing controlled combustion. The two shapes analyzed are a conventional re-entrant piston bowl, derived from a GM 1.9 L piston head, and a stepped-lip piston bowl, derived from the pistons employed in the Ford 6.7L Scorpion™ engine. Information about the engine is summarized on the Engine Combustion Network website [2], along with a detailed database of measurements from experimental studies performed with the facility. Specifically, two operating conditions were investigated:

- CDC9 - A conventional partial load, mid-range speed, diesel combustion mode, adopting a split pilot-main injection strategy and lightly boosted. This condition is representative of the cruise speed operation of a Diesel engine for transport applications;
- LTC3 - A highly diluted low temperature combustion mode, adopting single injection in late stage of compression, thus involving an high level of premixed combustion. This operating point is representative of idle operation and can be used to study advanced combustion modes for compression ignition engines.

In this work of thesis, only the former of the two operating conditions has been studied. This choice is driven by the importance of the operating point in engine applications. In fact, cruise speed and load is expected to be the operating

condition most often experienced by internal combustion engines for transport applications. Therefore, studying this condition is of great interest for engine designers, in order to maximize thermal efficiency and limit production of noxious pollutants (namely NOx and particulate matter). Moreover, in this thesis simulations have been performed only with the conventional re-entrant piston bowl geometry.

Specifically for this operating condition, extensive experimental investigations have been performed by many authors, each of them dedicated to specific aspects of charge and combustion dynamics in CI engines. Busch et al. [47] and Zha et al. [38] performed an injection-timing sweep, where both pilot and main injection were block-shifted with constant dwell of about 10 crank angle degrees (CAD). In these studies the pilot injection mass was kept constant and the mass of main injection was adjusted to keep a constant load of 9 bar indicated mean effective pressure (IMEP). Of the analyzed operating conditions, the authors identified three injection timings, which are representative for the overall effect of injection timing:

- SSEp17b - An early injection timing, where the the main injection occurs when the piston is almost at top dead center (TDC). In this condition, the thermal efficiency is about at its maximum and the spray targeting directs almost all of the fuel inside the piston bowl. Here no significant differences were observed by changing the piston geometry;

- SSEp07b - An intermediate injection timing, where the start of main injection is such that the fuel spray hits the piston rim, leading high level of spray-wall interaction and mixing controlled combustion. This injection timing was chosen because a significant increase in thermal efficiency was observed adopting the stepped lip geometry with respect to the conventional one, along with significant reduction in soot production. Enhancement of mixing controlled combustion was hypothesized to be the reason of these experimental findings;

- SSEp02a - A late injection timing, where the main injection happens during expansion stroke. In this condition, most of the spray is directed towards the squish region, and bulk gas temperature and pressure are significantly lower then those at TDC. For this reason, this injection condition is expected to reproduce the dynamics of low temperature combustion strategies (longer ignition delay, higher level of premixed combustion, lower NOx and higher CO and products of partial oxidation).

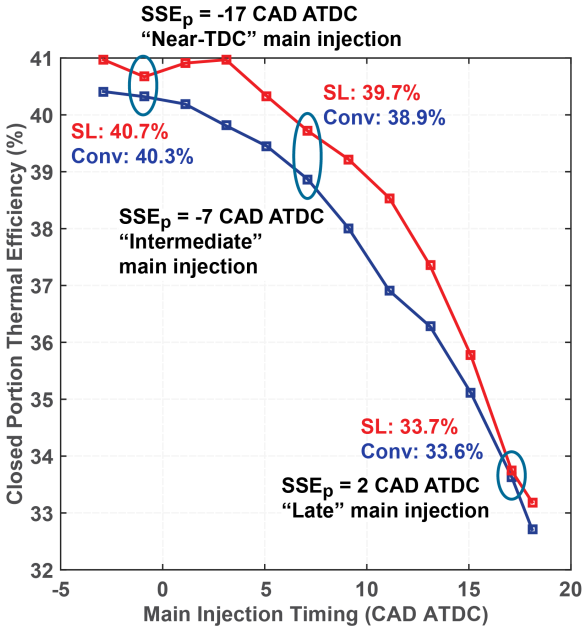

Figure 1.1: *Behavior of thermal efficiency with respect to injection timing for the re-entrant (blue) and stepped-lip (red) piston blow geometries [47]. The three reference injection timing conditions are highlighted.*

Sahoo et al. performed planar laser-induced fluorescence (PLIF) measurements to study the vaporization and mixing behavior of pilot injection [13]. In their work, they measured the evolution of mixture fraction field on three planes parallel to the piston head, and they studied the impact of injection parameters (injected mass and rail pressure) and in-cylinder conditions (bulk gas temperature and swirl intensity) on it. From their findings, the pilot injection is expected to penetrate up to the bowl rim, and to produce significant fuel-rich mixture, particularly in the region at the tip of the jet. For the late injection case, characterized by a lower bulk gas temperature, the fuel from pilot injection is expected to have a high level of premixed combustion, with risk of over-lean zones and low combustion efficiency. Moreover, jet-to-jet variations in fuel distribution were observed in the experiments.

Utilizing high-speed soot natural luminosity (NL) imaging, Zha et al. reconstructed the in-cylinder velocity field during combustion, adopting the Combustion Image Velocimetry (CIV) technique [38]. Analyzing the development of CIV-resolved swirl ratio, the authors observed substantial swirl amplification after CA50[1] for early and intermediate injection timings, therefore deducing that

[1]Instant when 50% of the injected fuel has burnt.

in these conditions the mixing process is driven by spray-wall interaction rather than squish/reverse squish flow processes. From these measurements they were also able to compute the charge flows on piston walls in late stage of combustion and to identify the regions of soot formation.

Dynamics of in-cylinder flow structures during compression stroke were analyzed by Zha et al., through Particle Image Velocimetry (PIV) measurements on multiple swirl planes [39]. The authors were able to characterize the morphology of flow structures inside the cylinder, in terms of tilting and eccentricity of the swirl axis, and the effect of intake port geometry. From the measurements, a significant tilting and eccentricity of the swirl axis was observed, and their evolution during compression was analyzed in depth by the authors. A similar evolution of swirl structure was observed for different steady state swirl ratio, from which the authors deduced that the intake port geometry is not of main importance for late compression mean flow asymmetry.

Finally, Bush and Miles performed an experimental study to characterize the fuel injection system and assess the reliability of the fuel flow measuring system adopted [49]. This was done by assessing the impact of many parameters on the measured mass flow rates. Therefore, reliability of the injection rate profiles and injected mass in each operating condition studied has been proven.

1.2 Previous simulation studies

Thanks to the extensive and various experimental campaigns that have been performed on the above cited optical engine, and to the level of detail with which boundary conditions of each test are reported, the ECN experimental database has been used by many authors for validation of numerical models.

Full-cycle simulations with detailed geometry of the engine have been performed by many authors, in order to have insights of the in-cylinder flow structures generated during induction and compression strokes [20, 22, 23]. The authors observed that, with the conventional piston bowl geometry, a strong swirl vortex is sustained along the compression stroke, and it is enhanced when entering the bowl at TDC. By decomposing the flow field into squish and swirl velocity component, in [20, 22] a strong swirl-squish interaction was observed: the axis of the swirl vortex is close to the piston axis and a strong, azimuthally symmetric, toroidal vortex is generated from the squish flow. Perini et al. also observed marginal impact of engine speed and compression ratio on flow structures, as “bulk flow and turbulence quantities scale smoothly with these parameters” [22]. Principal Component Analysis was used on the validated CFD cold-flow simulations to give

quantitative characterization of the evolution of the swirl vortex inside the cylinder during intake and compression stroke [23].

Non reacting simulations were performed by Busch et al. on the early and intermediate injection timings, to understand the flow structures generated inside the cylinder due to the interaction between spray and piston surface [48]. The authors observed that spray-wall interaction plays a dominant role: impingement of the spray onto the bowl rim leads to splitting of the fuel jet among squish and bowl regions. Inside the bowl region, a strong toroidal vortex is generated, while no stable recirculating flow structures are formed in the swish region, where the spray is just slightly deflected upwards and continues to propagate outwards. For the re-entrant piston bowl geometry, the authors observed limited variations in the flow topology among the two injection timings studied, having in both cases dominance of the long-lasting bowl vortex. Recently, some authors have also investigated the combustion dynamics, by performing reacting spray simulations [26, 32]. Perini et al. observed that ignition and combustion of the pilot injection behaves like in an homogeneous adiabatic reactor, while the main injection's ignition and combustion development are sensible to local in-cylinder flows [26]. Specifically, the fuel delivered during the main injection is ignited when fuel vapor interacts with the high-temperature mixture from pilot flame. By performing simulations with different swirl intensities, the authors deduced that pilot-main clocking mainly affects ignition timing of main injection, being also responsible for the high cyclic variability of premixed heat release rate.

Some authors also studied the impact of geometric details of combustion chamber on the characteristics of in-cylinder flow properties, by comparing full-cycle simulations with sector mesh simulations [20, 25]. The main differences that were observed between the two cases are the following:

- Noticeable difference was observed between the predicted tangential velocity profiles, especially approaching the TDC. The sector simulations preserved the Bessel-like behavior all along the compression stroke, while the full-engine mesh captured the velocity profiles both in shape and absolute values;
- The sector mesh over-predicted tangential velocities in the bowl region (see Figure 1.3). This was primarily consequence of the in-cylinder flow initialization in the sector simulations, where a constant swirl ratio was assumed along the cylinder axis. However, this assumption was showed to be incorrect due to limited penetration of the swirl vortices generated by intake ports;
- Due to non-symmetric intake port design, the swirling flow shows a non-axisymmetric structure. The authors suggested that this might lead to jet-to-jet differences in terms of air entrainment and mixture formation;

- Due to strong flow non-uniformities generated during induction stroke, the full mesh simulation predicted a steady reduction of swirl ratio during compression stroke, along with higher turbulence intensity;
- Strong differencies were observed in the evolution of in-cylinder swirl ratio and turbulence intensity. Geometric details on cylinder head showed to have a strong impact on the velocity fields. These acted as a barrier for the air flow, especially when the piston is close to the TDC, and tended to increase the dissipation of mean flow into turbulent flow. For this reason, the peak swirl ratio at TDC was over-predicted with the sector mesh simulations (see Figure 1.2);
- By performing simulations with a 360 sector mesh with initial velocity field mapped from the full-cycle simulations, Perini et al. observed that engine geometry details have a stronger impact on in-cylinder flows and turbulence distribution than initial flow conditions [25].

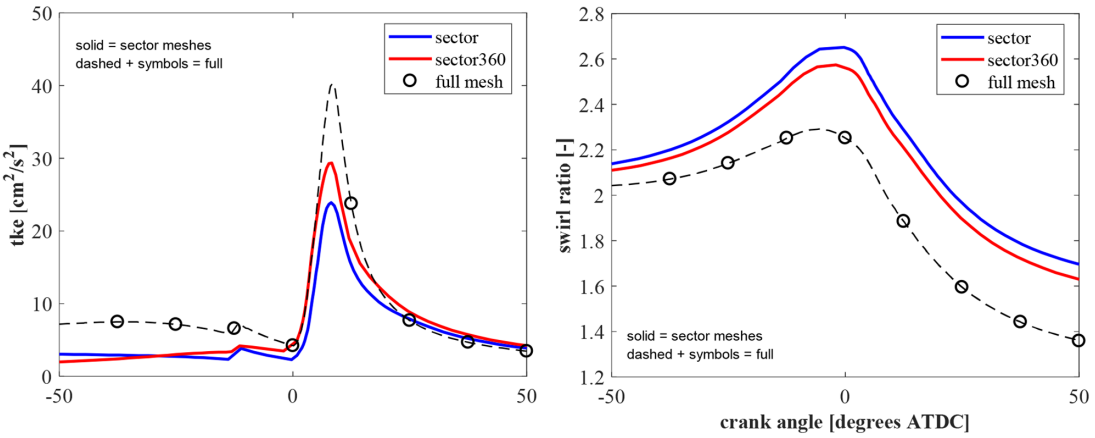

Figure 1.2: *Plots of temporal evolution of swirl ratio (SR) and turbulent kinetic energy (TKE), showing the impact of sector mesh modeling with respect of full engine mesh approach [25]*

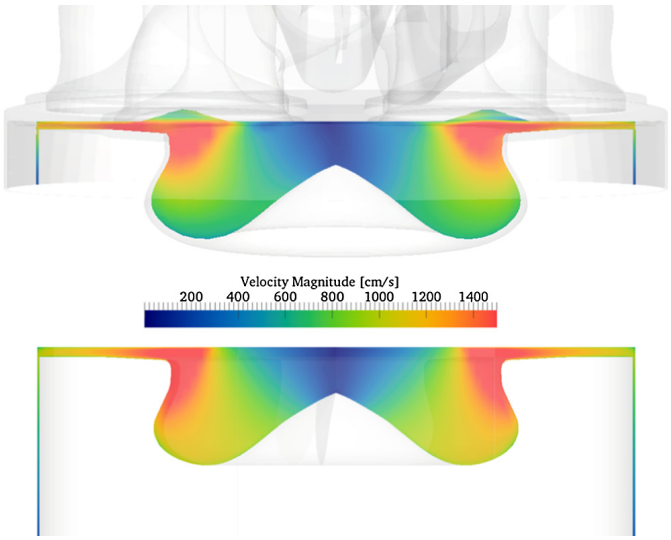

Figure 1.3: *Overprediction of flow speed inside the bowl at TDC as a consequence of initialization of homogeneous swirl with sector mesh approach [20]*

Chapter 2

Numerical models

Modeling of compression ignition internal combustion engines has always been challenging, due to the variety of physical and chemical processes involved and their complex interaction. A comprehensive multidimensional CFD model for this applications should be able to predict the dynamics of gas exchange, evolution of turbulent flow structures, liquid fuel injection and the consequent spray evolution, dynamics of the combustion process, production of noxious substances, etc. To handle the extremely high level of complexity of the overall problem, several models and sub-models are required, each describing a specific aspect. Among these, the following groups of models have a strong impact on describing the overall combustion process [45, 14]:

- Spray models - They have the purpose to predict the evolution of the liquid fuel when injected inside the combustion chamber. Several sub-models are involved in describing this process, from generation of fuel droplets, to their progressive degradation into smaller particles due to aerodynamic interaction with gas phase and, eventually, evaporation;

- Turbulence models - These are required to close the turbulent flow components generated when performing Reynolds averaging of the Navier-Stokes equations. This aspect is crucial for predicting turbulent flow structures, degradation of mean-flow energy into turbulence, diffusion and mixing of chemical species and other quantities relevant for the combustion process, etc.;

- Combustion models - These have to describe the chemical processes happening during combustion of the air-fuel mixture. The main problems that these models have to face are related to the complex dynamics of combustion in

compression ignition engines, the number of species and reactions involved, and the interaction of chemistry with the flow dynamics.

As far as the first of the three aspect is concerned, both simulations in constant volume vessel and operating engine seem to agree that the most suitable approach for describing the mechanics of spray formation is the model proposed by Beale and Reitz considering both combined Kelvin-Helmholtz and Rayleigh-Taylor instabilities [36], and variants of this model with different sub-models. For this reason all the simulations in this thesis are performed with the above cited breakup model. No such strong agreement was found in the case of the other modeling aspects.

Many turbulence models have been proposed in the literature, and their performances in Diesel engine applications have been studied by many authors [41, 60, 24, 9]. From their studies, the k-ε turbulence closure and its variants seemed to give the best results. However, each of them did not show the same performances when studying individually the relevant phenomena happening in CI engines (flow structures generated during induction and compression strokes, prediction of mass flow rate through valves, turbulence level in spray region and at wall impingement, liquid and vapor penetration, mixture fraction distribution, etc.). For this reason, no wide agreement is found in the literature, but researchers seem to be polarized around two main turbulence models: the standard k-ε model, and its Re-Normalisation Group (RNG) variant. In the current work of thesis, simulations are performed with both these turbulence models, to assess their performances in predicting the dynamics in mixing-controlled diesel combustion.

Combustion models can be divided into two main groups: those that describe the combustion phenomena by adopting detailed chemistry solvers, and those that rely on simplified models to predict ignition and combustion of air-fuel mixture. Some authors compared these two branches of combustion modeling [51, 42], observing that those not solving detailed chemistry had limited capability to predict combustion features in both single and multiple injection strategies, being really sensitive to model constants and giving good results only in narrow ranges of operating conditions. For this reason, in this work only combustion models with detailed chemistry are taken into account. According to literature, the most widespread combustion models adopting detailed chemistry for CI ICEs applications are the Well-Mixed model and the Representative Interactive Flamelet model (RIF). The variant with off-line tabulation of Well-Mixed model is assessed in this work (TWM), and compared in performances with the multiple-flamelet version of RIF model (mRIF), both implemented in the LibICE and previously validated in different works [29, 28, 54].

This chapter is dedicated to a brief description of the turbulence and combus-

tion models assessed in the present work, reporting some considerations on their strengths and weaknesses that were observed in past studies.

2.1 Combustion models

2.1.1 Representative Interactive Flamelet model

The RIF model is based on the laminar flamelet concept: the flame is modeled as a set of thin diffusive flamelets, and combustion takes place in the regions where mixing produces a nearly stoichiometric air-fuel mixture. This model has seen good agreement in CI engine applications, since conventional Diesel combustion is mostly diffusive. Its derivation has been widely discussed in the literature [34, 45, 14] and here the most important aspects are reported. The explanation of how the model is implemented in the LibICE code can be found in Colombi and D'Errico et al.[44, 28], along with the description of the modifications introduced to enhance its performances and reduce the computational time.

The first step of this model is the introduction of a new non-dimensional scalar quantity, called mixture fraction Z: it can be derived by performing suitable variable changes on the transport equations of temperature and mass fraction of reacting chemical species, and it is normalized in order to be 1 in the fuel stream and 0 in the oxidizer stream. Equation 2.1 shows the averaged balance equation that Z follows; for its closure, another variable has to be introduced, the variance of mixture fraction Z''^2, which transport equation is given by 2.2. In these, the Sc_Z and $Sc_{Z''^2}$ are the Schmidt numbers of mixture fraction and its variance respectively, both assumed to be equal to 0.7 in this work. $\dot{S}$ is a source term from spray, whereas μ_t is the turbulent dynamic viscosity, calculated from the turbulence model, and χ is the scalar dissipation rate, a sink term due to turbulence, given by equation 2.3. C_χ is a model constant and it is assumed to be equal to 2.

$$\frac{\partial \rho \widetilde{Z}}{\partial t} + \nabla \left(\rho \mathbf{U} \widetilde{Z} \right) - \nabla \cdot \left(\frac{\mu_t}{Sc_Z} \nabla \widetilde{Z} \right) = \dot{S} \tag{2.1}$$

$$\frac{\partial \rho \widetilde{Z''^2}}{\partial t} + \nabla \left(\rho \mathbf{U} \widetilde{Z''^2} \right) - \nabla \cdot \left(\frac{\mu_t}{\widetilde{Z''^2}} \nabla \widetilde{Z''^2} \right) = 2 \frac{\mu_t}{Sc_{Z''^2}} \left| \nabla \widetilde{Z} \right|^2 - \rho \chi \tag{2.2}$$

$$\chi = C_\chi \frac{\varepsilon}{k} \widetilde{Z''^2} \tag{2.3}$$

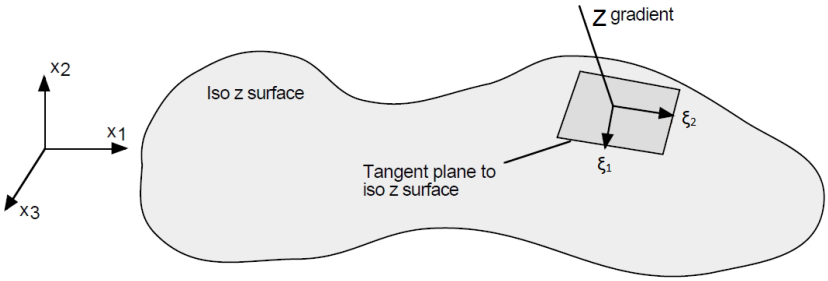

Figure 2.1: *Schematic of coordinate change from a Cartesian set* $\{x_1, x_2, x_3\}$ *to iso-Z surfaces* $\{\xi_1, \xi_2, Z\}$*. A single iso-Z surface is represented, with a generic tangent plane*

The introduction of mixture fraction Z allows to perform a change of variables in the description of the flame structure, moving from a Cartesian set of coordinates x_i to a new one defined with respect to the iso-Z surfaces (depicted in Figure 2.1). Under assumption of thin diffusive flames, in this new set of coordinates the dominant variable is the mixture fraction, having that gradients in $\xi_{1,2}$ directions are negligible with respect to those in Z direction. Therefore the flame can be considered locally one-dimensional, and energy (h) and mass fraction (y_i) balance equations can be solved on a 1D domain depending only by a single variable: the mixture fraction.

$$\rho \frac{\partial y_i}{\partial t} = \rho \frac{\chi_Z}{2} \frac{\partial^2 y_i}{\partial Z^2} + \dot{\omega}_i \tag{2.4}$$

$$\rho \frac{\partial h_s}{\partial t} = \rho \frac{\chi_Z}{2} \frac{\partial^2 h_s}{\partial Z^2} + \dot{q}_s \tag{2.5}$$

Here, ω_i and y_i are respectively the chemical source term and mass fraction of generic i-th species, h_s is the sensible enthalpy, and $\dot{q}_s$ is the heat release by chemical reactions. χ_Z is the scalar dissipation rate in the mixture fraction space, which is obtained as an average over the CFD domain assuming β-PDF distribution on sub-grid scale [44]. This parameter models the effect of turbulent mixing on combustion, thus binding the flow and combustion dynamics. Detailed description of equations used by CFD code to compute χ_Z can be found in [44], and here are not reported being out of the scope of this work.

However, modeling of combustion as an individual diffusive flamelet introduces and excessive oversimplification of the real combustion dynamics in CI engines. Limitations of this model are caused by the following aspects:

- Non-uniformity in turbulence is not considered, because the scalar dissipation rate is averaged on the overall domain, and local flow structures may

have a significant impact on combustion development and prediction of pollutant formation;

- In case of long ignition delay, the portion of premixed combustion tends to drastically increase (condition typical of low temperature combustion strategies, with high levels of exhaust-gas recirculation (EGR)). In this condition, flame structure is far from being diffusive: ignition takes place in several auto-ignition spots inside the premixed air-fuel mixture, and propagates within the premixed region. This feature cannot be represented by the conventional RIF model, since once ignition condition is reached, the premixed charge is ignited all at once, being characterized by the same values of mixture fraction. For this reason, heat release rate (HRR) in premixed combustion is strongly overestimated by RIF model in these conditions;

- By looking at the conceptual model of stabilized mixing-controlled combustion proposed by Dec [15] depicted in figure 2.2, the flame is not attached to the injector hole, but a fuel-rich premixed flame is formed at a stable distance from the injector nozzle, where fuel is vaporized and mixed with air. This flame stabilization mechanics cannot be represented by the conventional RIF model, because it is not able to predict flame propagation in premixed mixtures, the charge is ignited up to the injector nozzle.

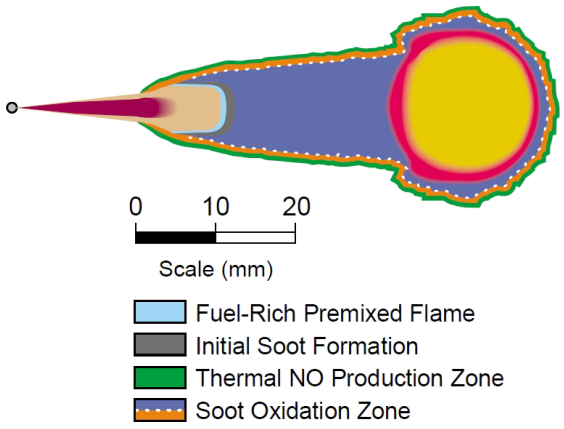

Figure 2.2: *Scheme of stabilized mixing-controlled flame in conventional Diesel combustion. [15]*

To improve the performances of the RIF model, a multiple number of flamelets have been used, each of them is representative of a certain portion of the injected fuel mass and is tracked by a marker M_j, following a transport equation analogue

to 2.1. Each marker is representative of the portion of mixture fraction in the corresponding flamelet, thus the following identity must hold, where N_f is the number of flamelets.

$$Z = \sum_{j=1}^{N_f} M_j \tag{2.6}$$

Figure 2.3 summarizes the operation of the RIF model with multiple flamelets (mRIF) combustion model, illustrating the mutual interactions between the CFD and flamelet domains.

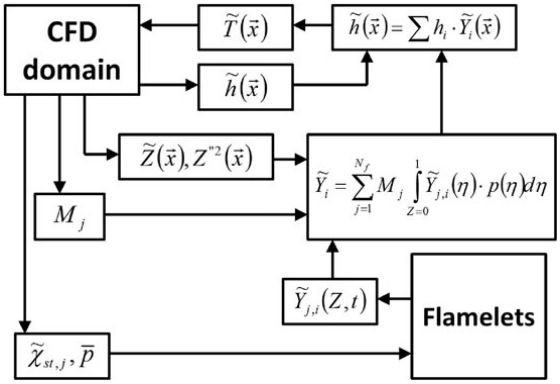

Figure 2.3: *Scheme of mRIF model, showing interaction between CFD and flamelets domains [29]*

It has been shown that this extension of the conventional RIF model has the capability to mitigate the limitations mentioned above, thanks to its capability to account on non-homogeneities in flow structures and turbulence. Moreover, past studies showed that when partitioning of flamelets is performed according to injection time (or mass), and interaction among flamelet domain is neglected, the mRIF model is also able to predict flame stabilization phenomenon [28, 29, 44]. However, authors suggested that a maximum delay of 0.1 ms among change in flamelet injected is needed, to correctly describe flame stabilization and predict the lift-off length[1] (LOL) [28]. This improvement may come at the cost of strong increment of computational time, because tens of flamelets may be needed in case of long injections, thus strongly increasing the number of calculations required.

[1]The flame generated by direct injection Diesel combustion is an example of lifted fame. The distance between the injector nozzle and the stabilized flame is called 'lift-off length'.

2.1.2 Well-mixed model with tabulated kinetics

The second combustion model that is considered in this work is a modification of the Well-Mixed model, where chemistry is not computed at each time step, but it is extrapolated from a table containing the chemical kinetics in a set of several thermodynamic conditions. Validation of the model has been performed by Lucchini et al. [54]; a description of the model and its implementation in the LibICE code can be found in [4]. The fundamental assumptions of this model will be summarized, with its fundamental equations and related strength and weaknesses.

In standard Well-Mixed model, each cell of the CFD domain is treated as a closed homogeneous system, thus neglecting any sub-grid scale turbulence-chemistry interaction. By assuming that chemical time scale is much smaller then the fluid-dynamic one (condition that generally holds in CI engine combustion applications) solution of chemistry and fluid-dynamics can be can be decoupled. The chemical kinetics is integrated by an ODE stiff solver within the CFD time-step, starting from the current conditions in the control volume. In each cell, evolution of mass fraction of each chemical species and energy are described by the following first order, non-linear, ordinary differential equations:

$$\frac{dy_i}{dt} = \frac{\dot{\omega}_i M_i}{\rho} \tag{2.7}$$

$$\frac{dT}{dt} = -\frac{\sum_i^{n_s} \dot{\omega}_i h_i}{\rho c_p} \tag{2.8}$$

Where $\dot{\omega}_i$, h_i, y_i and M_i are respectively the reaction rate, internal enthalpy, mass fraction and molecular weight of i-th specie. c_p is the specific heat capacity at constant pressure of the mixture and n_s is the number of chemical species in the mixture. These equations are solved within the time-step, and the concentrations of chemical species due to reaction are provided to the CFD code. The other quantities, included temperature distribution, are computed from the CFD code by solving their transport equations.

It can be observed that the number of ordinary differential equations to be solved scales up with the number of species in the reaction mechanism. This puts a limit to the accuracy to which chemistry is described, due to the strong increase in computational time when larger mechanisms are used. One of the strategies that have been proposed and validated in literature to overcome this limitation is tabulation of chemical kinetics. In this work, off-line tabulation of chemistry is adopted, on the basis of the work developed in [4]. Figure 2.4 shows the a

schematic of how tabulation of chemistry is performed, and here the process will be summarized.

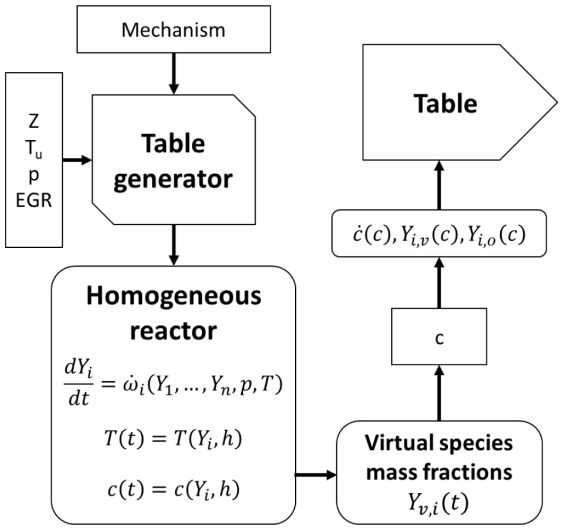

Figure 2.4: *Schematic of tabulation procedure [4]*

First, an input file is defined, which contains information about:

- The reaction mechanism to be used in calculations;
- A range of initial conditions for each variable required to compute the chemistry (ambient pressure p, initial reactor temperature T_u, mixture fraction Z, initial air composition).

Unburned gas temperature T_u can be computed in two different ways, whether mixing of oxidizer and fuel is considered or not (mixing-line assumption). In the first case, fuel is injected at liquid state at a given temperature T_f, and the initial temperature is computed from the enthalpy of the mixture:

$$h_0(Z) = (1 - Z)h_{Z=0}(T_{Z=0}) + Z\ h_{Z=1}(T_{Z=1}) - Z\ h_l(T_{Z=1}) \tag{2.9}$$

Where h_l is the latent heat of evaporation of the fuel. Therefore, T_u is a function of Z and the initial air and fuel temperatures. In the second case fuel and air are assumed perfectly mixed and both in gaseous state at same temperature. Hence, initial mixture temperature is not dependent from the mixture fraction and it is given from the data for T_u in the input file. These two approaches have been shown to be equivalent [4], since in both cases all possible thermochemical states of the system are covered. Differences in the results with these two methods are only due

to interpolation from different sets of table points, and the this effect is negligible if the ranges of initial conditions have a sufficiently refined discretization. In this work, mixing line was not considered to perform the tabulation.

Once that the set of initial conditions is defined, for each one combustion is simulated under assumption of homogeneous constant pressure reactor, i.e. equations 2.7 and 2.8 are solved. Equations are integrated by an ODE solver until either combustion is completed or a reasonably long end time, defined in the input file, is reached. This second end condition is required for those cases in which complete combustion is never reached, i.e., at low temperature. Contemporary to the resolution of the ODE system, which yields the evolution of the state (y_i, T) with respect to time, other relevant variables are computed at each time-step, required to the coupling with the CFD solver:

- A *progress variable* (C), which is a function of the state of the system, and measures the combustion's advancement;
- A set of *virtual species* $(y_{v,i})$ representative of the mixture composition. These are introduced to minimize the memory required to store the table, since having that storage of evolution of all chemical species in the mechanism would be unfeasible. They are defined so that the most important physical and thermochemical properties of the mixture are preserved.

In this model, the progress variable is calculated from the enthalpy of formation at reference conditions[2] of the mixture at the given time-step, also known as h_{298}. The minus sign in Eq. 2.10 is needed so that C increases through combustion, as the enthalpy of formation decreases as combustion progresses.

$$C(t) = -\sum_{i=1}^{n_s} y_i(t) h_{298,i} \tag{2.10}$$

The adopted definition of the progress variable guarantees that it uniquely characterizes each point in the thermochemical state-space ad it is appropriate for a transport equation. At the end of the calculations, the progress variable is normalized with respect to its minimum and maximum values, i.e., those at initial conditions and equilibrium respectively, and then stored. Thus, C_{min} and C_{max} are tabulated as well. The reaction rate is computed from the normalized progress variable through a forward differencing scheme.

$$c(t) = \frac{C - C_{min}}{C_{max} - C_{min}} \tag{2.11}$$

[2] $T_{ref} = 298.15K$, $p_{ref} = 1bar$

$$\dot{c}(t_i) = \frac{c(t_{i+1}) - c(t_i)}{t_{i+1} - t_i} \tag{2.12}$$

As mentioned before, to limit the dimension of the table imported in the CFD solver, composition at each time-step is expressed through a set of virtual species, which are representative of the real mixture. The virtual composition is defined to guarantee conservation of mass and main thermochemical properties: number of atoms for each atomic species, mixture molecular mass, enthalpy and specific heat.

$$\begin{cases} \sum_{i=1}^{n_{s,v}} y_{v,i} = 1 \\ \sum_{i=1}^{n_{s,v}} N_{k,i}\ x_{v,i} = \sum_{j=1}^{n_s} N_{k,j}\ x_j \qquad \forall k \in \{C, H, O, N, \dots\} \\ \sum_{i=1}^{n_{s,v}} h_i(T)\ y_{v,i} = \sum_{j=1}^{n_s} h_j(T)\ y_j \\ \sum_{i=1}^{n_{s,v}} c_{p,i}(T)\ y_{v,i} = \sum_{j=1}^{n_s} c_{p,j}(T)\ y_j \end{cases} \tag{2.13}$$

In equation 2.13 it is shown the algebraic linear system to be solved to find mass fractions of virtual species; $N_{k,i}$ is the number of atoms of atomic species k in i-th chemical specie, x_i is the mole fraction of i-th specie, and subscript v indicates that the quantity refers to the set of virtual species.

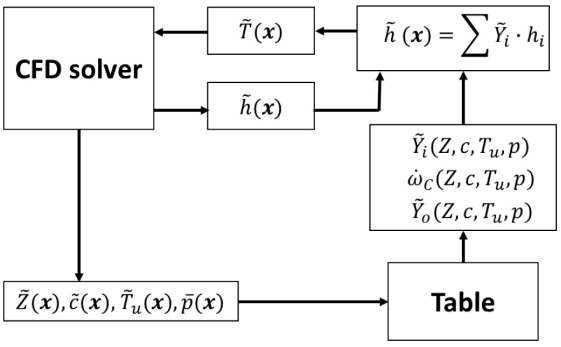

Figure 2.5: *Scheme of tabulated Well-Mixed model, showing how the CFD model retrieves information about chemistry from the tabulation [54]*

To link the CFD solver to the tabulation, the following transport equations for mixture fraction, enthalpy, unburned gas temperature and progress variable

have to be solved in the CFD domain, thus the table is accessed with the local cell values.

$$\frac{\partial \rho \widetilde{Z}}{\partial t} + \nabla \left(\rho \mathbf{U} \widetilde{Z} \right) - \nabla \cdot \left(\frac{\mu_t}{Sc_Z} \nabla \widetilde{Z} \right) = \dot{S}_Z \tag{2.14}$$

$$\frac{\partial \rho C}{\partial t} + \nabla \left(\rho \mathbf{U} C \right) - \nabla \cdot \left(\frac{\mu_t}{Sc_Z} \nabla C \right) = \rho \dot{C} \tag{2.15}$$

$$\frac{\partial \rho h_u}{\partial t} + \nabla \left(\rho \mathbf{U} h_u \right) - \nabla \cdot \left(\alpha_t \nabla h_u \right) = \rho \dot{Q}_s + \frac{\rho}{\rho_u} \cdot \frac{Dp}{Dt} \tag{2.16}$$

$$\dot{C} = \left(C_{max} - C_{min} \right) \cdot \dot{c} \tag{2.17}$$

In eq. 2.14 $\dot{S}_Z$ is the source term due to spray evaporation; in eq. 2.15 $\dot{C}$ is the progress variable source term due to combustion, retrieved from the table; in eq. 2.16 α_t is the turbulent thermal diffusivity, ρ_u is the unburned gas density, and $\dot{Q}_s$ is a source term due to spray evaporation, whose expression changes whether the mixing-line were assumed or not in the table generation process [4]. Figure 2.5 shows a block-scheme describing the interaction between CFD code and tabulation.

Lucchini et al. [54] observed that, although tabulation of chemical kinetics allows strong reduction of computational time and utilization of wider reaction mechanisms, it also introduces a significant level of simplification in the system, being that a $n_s + 1$ dimensional problem is reduced to only 4 dimensions (Z, C, p, T_u). This aspect was shown to be critical in the ignition process when highly rich regions are present ($\phi > 3$), which are characterized by long ignition delays and fast single-stage combustion:

1. Low temperature combustion reactions begin in regions with nearly stoichiometric composition ($\phi \sim 1$), thus progress variable ramps up to a intermediate nearly steady level while cold flame reactions proceed;

2. Progress variable is diffused from these regions toward the center of the vapor cloud, where highly rich mixture is present ($\phi > 3$);

3. As soon as there is a progress variable increase in the rich region, ignition takes place with highly reactive, single stage combustion. Therefore, normalized progress variable rapidly ramps up;

4. High values of progress variable are diffused back to lean regions, thus high-temperature combustion of air-fuel mixture starts.

The overall result of this mechanism is that as soon as low-temperature ignition delay is reached in stoichiometric regions, the whole jet ignites, therefore the ignition delay was strongly under-predicted. In order to limit this behavior and being able to describe the two stage ignition process, the reaction rate $\dot{C}$ is set to zero in highy rich regions, with a threshold value of $\phi = 3$.

Validation of the Tabulated Well-Mixed combustion model was performed in [54], by means of the constant volume spray and engine simulations. The model is also compared with direct integration of Well-Mixed model and other combustion models with the same tabulation. The authors observed that TWM model correctly predicts HRR during mixing-controlled combustion, slightly under-predicts ignition delay and over-predicts HRR during cold flame combustion. The conventional WM model overestimates the lift-off length, as a consequence of neglecting turbulence-chemistry interaction. The TWM predicts a shorter LOL with respect to the WM model with direct integration, because diffusion of progress variable allows ignition of rich mixture further upstream. With regards to real engine simulations, the model achieved satisfactory agreement with experimental data.

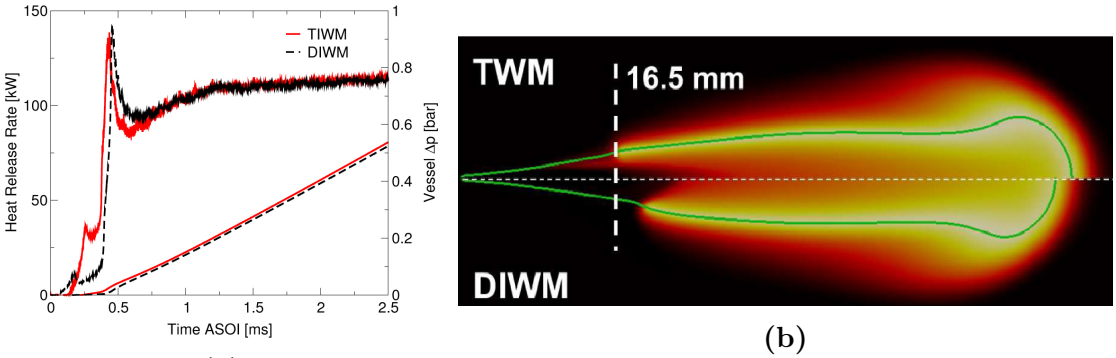

(a) **(b)**

Figure 2.6: *Comparison of TWM model and WM model with direct integration in constant volume spray simulations [54] - (a): HRR and pressure rise - (b): Flame structure and LOL*

2.2 Turbulence models

Turbulence modeling is required as a consequence of performing Reynolds average[3] on Navier-Stokes equations. Let us consider the momentum equation:

$$\frac{\partial \rho \mathbf{U}}{\partial t} + \nabla \cdot (\rho \mathbf{U}\mathbf{U}) = -\nabla p + \nabla \cdot \sigma + \rho \mathbf{g} + \mathbf{F_s} \tag{2.18}$$

$$\sigma = \mu \left[\underbrace{\nabla \mathbf{U} + (\nabla \mathbf{U})^T}_{2S} - \frac{2}{3} \nabla \cdot \mathbf{U} I \right] \tag{2.19}$$

Where $\mathbf{F_s}$ is the production term due to spray and I is the identity matrix. Thus, by averaging equation 2.18, the following is obtained:

$$\frac{\partial \bar{\rho} \widetilde{\mathbf{U}}}{\partial t} + \nabla \cdot \left(\bar{\rho} \widetilde{\mathbf{U}} \widetilde{\mathbf{U}} \right) = -\nabla \widetilde{p} + \nabla \cdot \widetilde{\sigma} - \nabla \cdot \left(\bar{\rho} \widetilde{\mathbf{U}'' \mathbf{U}''} \right) + \bar{\rho} \mathbf{g} + \widetilde{\mathbf{F}}_\mathbf{s} \tag{2.20}$$

We can observe that an additional source term is found, where $\widetilde{\mathbf{U}'' \mathbf{U}''}$ is the so-called Reynolds stress tensor, which is closed by the turbulence model. This is generally described trough Boussinesq hypothesis of linear stress-strain relationship, in an analogue way to the viscous tensor σ for Newtonian fluids (Eq. 2.19):

$$\bar{\rho} \widetilde{\mathbf{U}'' \mathbf{U}''} = -\mu_t \left[2\widetilde{S} - \frac{2}{3} \nabla \cdot \widetilde{\mathbf{U}} I \right] + \frac{2}{3} \bar{\rho} k I \tag{2.21}$$

$$k = \frac{1}{2} \mathrm{Tr} \left(\widetilde{\mathbf{U}'' \mathbf{U}''} \right) \tag{2.22}$$

Where k is the turbulent kinetic energy, expressed by eq. 2.22, and μ_t is turbulent dynamic viscosity. The turbulence models studied in this work are of the class of two-equations models, which means that turbulence is closed by means of transport equations. Regarding k-ε models, a new variable is introduced, the turbulence dissipation rate ε, and two transport equations are introduced for k and ε respectively. These depend on the specific formulation of the turbulence model, and will be described later for the two variants treated in this work. Then, transport of mass and momentum due to turbulence are modeled thorough an

[3] In engine applications, where compressibility cannot be neglected, Favre averaging is performed instead, which is a variant of Reynolds average weighted with respect to the density: $\varphi = \tilde{\varphi} + \varphi''$ $\quad$ $\widetilde{\varphi} = \frac{\overline{\rho \varphi}}{\bar{\rho}}$

increment of the dynamic viscosity of the fluid. The turbulent eddy viscosity is expressed with respect to k and ε as follows:

$$\mu_t = \bar{\rho} C_\mu \frac{k^2}{\varepsilon} \tag{2.23}$$

Where C_μ is a model constant.

2.2.1 Standard k-ε model

The derivation of the standard k-ε model for incompressible and compressible flows was widely discussed in the literature [27, 8], and an overview of its application in diesel engine simulations is available in Nordin [43], where also spray interaction is taken into account. Turbulent kinetic energy and turbulence dissipation rate are hence modeled with the following transport equations:

$$\frac{\partial \bar{\rho} k}{\partial t} + \nabla \cdot \left(\bar{\rho} \widetilde{\mathbf{U}} k \right) = \nabla \cdot \left[\left(\mu + \frac{\mu_t}{\mathrm{Pr}_k} \right) \nabla k \right] - \bar{\rho} \widetilde{\mathbf{U}'' \mathbf{U}''} : \nabla \widetilde{\mathbf{U}} - \bar{\rho} \varepsilon + \dot{W}_s \tag{2.24}$$

$$\begin{aligned} \frac{\partial \bar{\rho} \varepsilon}{\partial t} + \nabla \cdot \left(\bar{\rho} \widetilde{\mathbf{U}} \varepsilon \right) = \nabla \cdot \left[\left(\mu + \frac{\mu_t}{\mathrm{Pr}_\varepsilon} \right) \nabla \varepsilon \right] + C_{\varepsilon 3} \bar{\rho} \varepsilon \nabla \cdot \widetilde{\mathbf{U}} + \\ + \frac{\varepsilon}{k} \left(C_{\varepsilon 1} \bar{\rho} \widetilde{\mathbf{U}'' \mathbf{U}''} : \nabla \widetilde{\mathbf{U}} - C_{\varepsilon 2} \bar{\rho} \varepsilon + C_s \dot{W}_s \right) \end{aligned} \tag{2.25}$$

Where $\dot{W}_s$ is the term accounting for spray interaction, Pr_k and Pr_ε are the Prandtl numbers for turbulent kinetic energy and turbulence dissipation rate respectively, and $(C_{\varepsilon 1}, C_{\varepsilon 2}, C_{\varepsilon 3}, C_s)$ are model constants, whose values were computed by Pope [8] and here are reported in table 2.1. $C_{\varepsilon 1}$ has been raised from 1.44 to 1.5, a common practice in simulating spray and turbulent gas jet, leading to better agreement in liquid and vapor penetration for constant volume spray simulations.

2.2.2 RNG k-ε model

This turbulence model is a variant of the one described before, but Re-Normalization Group analysis is performed on the k and ε equations, which involves systematically removing infinitesimal bands of small scale flow components and accounting for them through the presence of an eddy viscosity in the mean-flow equations [57]. The overall result of this analysis are two equations for k and ε analogue to

2.24 and 2.25, but an additional sink term R is present in the ε equation. This term has been closed by Yakhot et al. [58], with the following formula:

$$R = \frac{C_\mu \rho \eta^3 \left(1 + \eta/\eta_0\right)}{1 + \beta\eta^3} \frac{\varepsilon^2}{k} \tag{2.26}$$

$$\eta = \sqrt{2} \left\| \widetilde{S} \right\|_F \frac{k}{\varepsilon} \tag{2.27}$$

Where $\| \cdot \|_F$ is the Frobenius norm, and β and η_0 are two model constants, whose value is shown in table 2.1. Han and Reitz [60] extended the work of Yakhot et al. by considering also compressibility and interaction with spray, and thus expressing the ε equation as follows:

$$\begin{aligned} &\frac{\partial \bar{\rho}\varepsilon}{\partial t} + \nabla \cdot \left(\bar{\rho}\widetilde{\mathbf{U}}\varepsilon\right) = \nabla \cdot \left[\left(\mu + \frac{\mu_t}{\mathrm{Pr}_\varepsilon}\right)\nabla\varepsilon\right] + C_{\varepsilon 3}\bar{\rho}\varepsilon\nabla\cdot\widetilde{\mathbf{U}} + \\ &+ \frac{\varepsilon}{k}\left[\left(C_{\varepsilon 1} - C_\eta\right)\bar{\rho}\widetilde{\mathbf{U}''\mathbf{U}''} : \nabla\widetilde{\mathbf{U}} - C_{\varepsilon 2}\bar{\rho}\varepsilon + C_s\dot{W}_s\right] \end{aligned} \tag{2.28}$$

$$C_\eta = \frac{\eta\left(1 + \eta/\eta_0\right)}{1 + \beta\eta^3} \tag{2.29}$$

An important difference in this formulation of the k-ε model and the conventional one is that here $C_{\varepsilon 1}, C_{\varepsilon 2}, C_\mu$ constants are directly obtained through the RNG procedure, without the necessity to apply dimensional analysis or empirical reasoning. Moreover, $C_{\varepsilon 3}$ is computed through the following expression:

$$\begin{aligned} C_{\varepsilon 3} = \frac{-4 + 2C_{\varepsilon 1}}{3} + &\frac{1}{\nabla\cdot\widetilde{\mathbf{U}}}\frac{1}{\nu_0}\frac{d\nu_0}{dt} + \frac{\sqrt{6}}{3}C_\mu C_\eta \eta (-1)^\delta \\ &\begin{cases} \delta = 1 & \text{if } \nabla\cdot\widetilde{\mathbf{U}} \leq 0 \\ \delta = 0 & \text{if } \nabla\cdot\widetilde{\mathbf{U}} > 0 \end{cases} \end{aligned} \tag{2.30}$$

All model constants for both turbulence models are reported in table 2.1. Next section will be dedicated to summarize the findings of some studies in which these two models have been compared.

Model	C_μ	$C_{\varepsilon 1}$	$C_{\varepsilon 2}$	$C_{\varepsilon 3}$	Pr_k	Pr_ε	C_s	η_0	β
Standard k-ε	0.09	1.5	1.92	−1.0	1.0	1.3	1.5	–	–
RNG k-ε	0.0845	1.42	1.68	Eq. 2.30	0.7194	0.7194	1.5	4.38	0.012

Table 2.1: *Turbulence models' constants. [8, 60]*

2.2.3 Comparison of two models

Choice of turbulence model was shown to be a key aspect while performing CFD simulations in CI engines. For this reason, in past works many authors focused on validating and comparing the turbulence models; here their findings regarding the two before mentioned turbulence models will be briefly reported.

Due to the complexity involved in performing measurements in engine applications, validation of turbulence models has been mainly performed on simplified experiments, representative of the main phenomena happening inside diesel engines, for which detailed measurements are feasible.

- Prediction of valve permeability was assessed by Bianchi et al [41] with steady flow experiments through intake ports, where discharge coefficient was measured. Due to its under-dissipative nature, the RNG k-ε model overestimated the port permeability much more than the linear k-ε model, leading to a higher underestimation of the valve discharge coefficient;

- Flow through valves is characterized by complex flow structures, with separated flows and recirculating regions. To assess the description of these phenomena, authors performed validation with both vertical and 45 degree-inclined backward-facing step experiments [41, 24], for which detailed measurements of velocity fields are available. The authors observed that both models had good agreement with experimental data in terms of axial velocity profile. However, RNG model better predicted flow reattachment, therefore confirming the better performance of this model in presence of high mean strain and recirculating flows, thanks to reduction of the mean-flow energy over-dissipation induced by standard ε-equation [41].

- PIV measurements in optical engine running in motored conditions were used by Perini et al. to assess the capability of the turbulence model to predict the flow structures generated in cylinder during induction stroke [24]. Acceptable agreement with experimental data was found for both turbulence models, with the best results given by the standard k-ε model. Indeed, the latter was the only one capable to capture correctly the tangential and radial speed profiles in the region close to the fire-deck;

- Capability to describe jet-wall interaction is assessed with impinging gas jet stream experiments, where an air flow descending from a long circular channel impacts against a wall normal to the stream direction. Validation was performed by Perini et al. in terms of mean and turbulent flow quantities in the impinging zone [24]. Turbulent kinetic energy at stagnation point was

significantly over-predicted by both models, but overall results in terms of mean and turbulent velocity fields were better with the RNG model;

- Non-reacting spray experiments in constant volume chamber were performed to assess capability in predicting spray dynamics, air-fuel mixture formation, and, therefore, the flame structure. Non-reacting spray simulations performed by Perini et al. showed little sensitivity of liquid spray penetration with respect to the turbulence model, while vapor phase showed higher sensitivity [24]. Comparison of mixture fraction distribution in axial and radial direction highlighted that RNG model performed better, while the conventional one showed excessive mixture spreading and reduced penetration. However,this limitation is overcome increasing $C_{\varepsilon 1}$ constant in standard k-ε model to 1.5 [46]. Yet both models still tend to under-predict vapor penetration.

From these studies, both turbulence models seem eligible to achieve good results in diesel engine simulations, if properly tuned. For this reason, both are tested in this work, to assess their performance in real engine conditions, where all the above mentioned phenomena interact.

Chapter 3

Case setup

3.1 Operating conditions

Here the engine geometry, spray targeting, operating conditions, and injection parameters will be summarized for the three cases studied, namely SSEp17b, SSEp07b and SSEp02a. Data were taken from the website of Engine Combustion Network [2], while an accurate description of the engine geometry, boundary conditions and operating conditions can be found in Zha et al. [38].

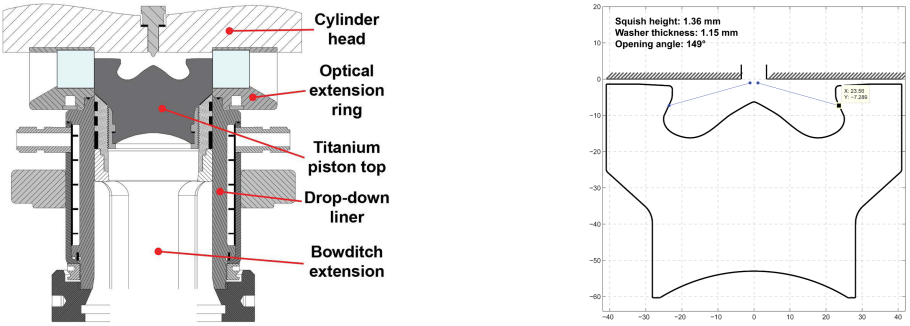

(a) **(b)**

Figure 3.1: *(a): Schematic of ECN optical engine assembly [47] - (b): Re-entrant piston bowl geometry, with spray targeting for SSEp07b case [2]*

A schematic of ECN small-bore optical engine assembly is depicted in figure 3.1a. The engine is equipped with a transparent fused silica piston, resembling the cylinder head from a General Motors 4-cylinder, 4-valve 1.9 L light-duty DI diesel engine, which is mounted on a piston extender to allow optical access. To exclude

the effect of valve cut-outs on the piston crown, the original shape was modified to flat piston top. Table 3.1 summarizes the most relevant engine geometrical parameters, while the piston bowl geometry is shown in figure 3.1b.The engine is equipped with a Bosh CRIP 2.2 injector, whose parameters are listed in table 3.2.

Bore	D	82	mm
Stroke	S	90.4	mm
Compression ratio	r	15.8	
Connecting rod length	l	166.67	mm
Pin offset	x_o	1.588	mm
Squish height	H_s	1.36	mm
Crevice height	H_c	29.57	mm
Crevice width	ΔD	0.182	mm

Table 3.1: *Engine geometrical parameters.*

Number of holes	n_h	7	
Hole diameter	D_h	139	µm
Nozzle conicity	k_s	1.5	
Included angle	l	149	deg

Table 3.2: *Bosh CRIP 2.2 injector parameters. [2]*

The engine is run at constant speed of 1500 rpm, in a part-load conventional diesel combustion mode with 9 bar IMEP. Split-injection strategy is adopted, with fixed pilot-main injection dwell of 1200 µs. Three injection strategies were considered, where both injections are block-shifted; pilot-injection mass was kept constant, while main-injection mass was adjusted to maintain constant load. Injection rate profiles are represented in figure 3.2a, while start-of-injection timings (SOI) and mass per injection in all three cases are reported in table 3.3.

For each engine testing point, the same intake charge composition was used (Table 3.5), resembling a value of EGR around 10%, with constant intake mass flow rate of 8.51 g/s. Intake charge temperature and pressure were fixed to 80 ℃ and 1.5 bar respectively, reproducing mid-boosted conditions, while motored TDC temperature was kept at 895.3 K.

The fuel used during the experimental investigations was the diesel primary reference fuel DPRF58, composed of 42 vol% n-hexadecane and 58 vol% 2,2,4,4,6,8,8-heptamethylnonane, having auto-ignition properties close to conventional diesel fuels. Its main properties are listed in table 3.6.

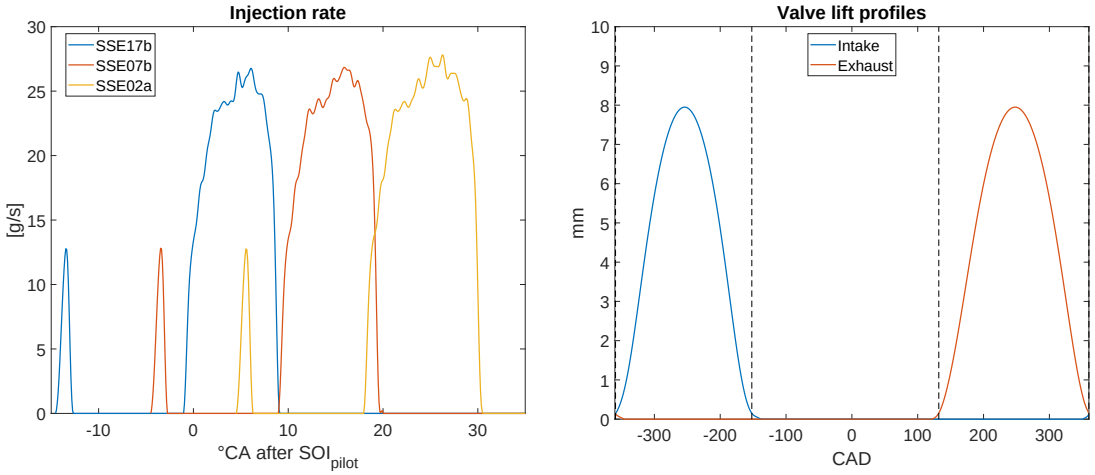

(a) **(b)**

Figure 3.2: *(a): Injection rate profiles for the three testing points - (b): Valve lift profiles for intake (blue) and exhaust (red).*

Case	SOI [CAD]		mass [mg]	
	pilot	main	pilot	main
SSE17b	-14.4	-0.9	1.4	22.61
SSE07b	-4.4	9.1	1.4	24.36
SSE02a	9.1	18.1	1.4	29.57

Table 3.3: *Injection parameters in the three cases considered in this work.*

3.2 Setup of CFD model

Simulations were performed with OpenFOAM [3], an open-source object-oriented software for multidimensional CFD simulations, and Lib-ICE, a well validated toolkit developed by the ICE Group from the Energy Departement of Politecnico di Milano in the OpenFOAM environment, containing state-of-the-art models and

solvers for engine applications.

Although past studies have shown that full engine simulations are mandatory to correctly predict turbulent flow structures and pollutant formation when applied to this engine [26, 20], the conventional sector mesh approach was used in this study. This choice was driven by the necessity to minimize the turn-over time of each simulation, due to the high variety of conditions assessed in this work. Moreover, it has been shown by past authors that sector meshes are still able to correctly reproduce the overall combustion dynamics. Hence, the computational domain reproduces a seventh of the combustion chamber, where a structured hexahedral mesh is used. Detailed description of the mesh structure and its parameters will be presented in section 3.4.

3.2.1 Initial and boundary conditions

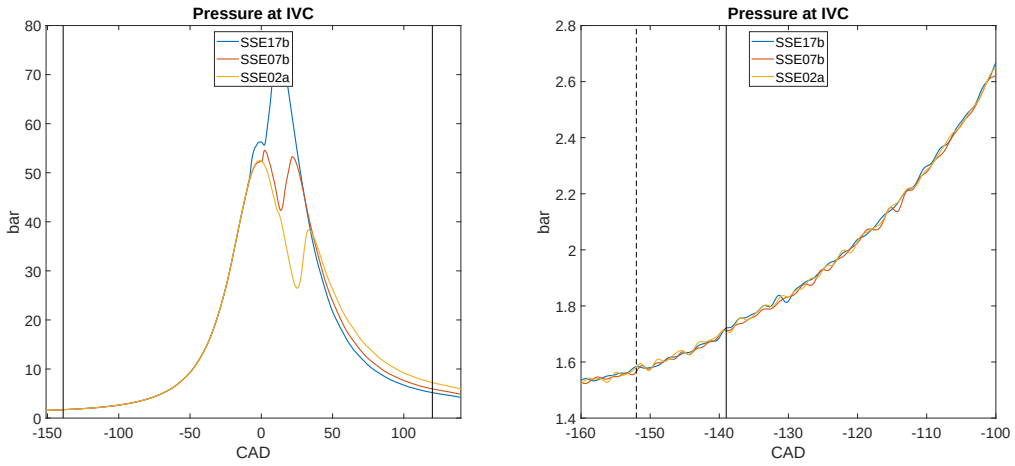

(a) **(b)**

Figure 3.3: *(a): Experimental pressure profiles in the three considered cases. Beginning and ending of simulations are indicated by the black lines. - (b): Nominal IVC (-151 CAD) and begin of simulation (-139 CAD), indicated by the dotted and the continuous black line respectively.*

The first step in setting up the CFD model was to estimate the in-cylinder conditions at inlet valve closing instant (IVC). Although the nominal IVC timing is at 151 crank-angle degrees before firing TDC, the start of simulation was set

to -139 CAD, to reduce uncertainties on pressure measurements due to dynamic perturbations generated by valve closure. For the sake of simplicity, from now on the attribute "IVC" will be referred to the instant of beginning of numerical simulation, rather than nominal IVC.

At intake pressure and temperature conditions, fresh charge can be modeled as an ideal gas, therefore the following equation holds at IVC:

$$pV = R_a^* m_a T \tag{3.1}$$

Where R_a^* is the mass-specific gas constant for the inlet air composition and m_a is the air mass inside the cylinder. By knowing that the average mass flow rate of fresh air is 8.51 g/s, the average air mass trapped inside the cylinder every cycle can be calculated[1]. Therefore, the temperature at IVC can be estimated from the available experimental parameters:

$$m_a = \dot{m}_a \frac{2 \cdot 60}{n} \tag{3.2}$$

$$T(\theta_{IVC}) = \frac{p_{IVC} V(\theta_{IVC})}{m_a R_a^*} \tag{3.3}$$

Where n is the engine speed, expressed in revolutions per minute, and $V(\theta)$ is the volume law, given by equation 3.12.

The in-cylinder flow field at IVC was set as a Bessel-shaped swirling vortex, with swirl ratio equal to the measured steady state value of 2.2. The overall IVC conditions and charge composition are summarized in tables 3.4 and 3.5 respectively.

Crank-shaft position	θ_{IVC}	-139	CAD
Pressure	p_{IVC}	1.7	bar
Temperature	T_{IVC}	386	K
Swirl ratio	$R_{s,IVC}$	2.2	
Surface temperature	Piston	440	K
	Cylinder	430	K
	Liner	440	K
Engine speed	n	1500	rpm

Table 3.4: *Initial and boundary conditions*

	x_i	y_i
O_2	0.792	0.765
N_2	0.197	0.218
CO_2	0.011	0.017

Table 3.5: *Air composition.*

[1]The "2" coefficient in equation 3.2 is accounting for being a 4 stroke engine, thus the induction stroke happens once every two cycles

Other operating conditions and boundary conditions are listed in table 3.4. Surface temperatures are the same used in past simulation studies on this engine, and are assumed to be reliable [48]. The surfaces inside the crevice were assumed to be adiabatic, while Angelberger heat transfer model [10] was used for piston and cylinder surfaces.

3.2.2 Fuel modeling

When setting up the case, no reduced mechanism for DPRF58 was immediately available, therefore it was chosen to use normal-heptane as fuel in simulations, being typically used as a surrogate for conventional diesel fuels. Hence, a reduced mechanism for n-heptane was used in this work, derived from the detailed reaction mechanism proposed by Curran et al. [35].

Detailed comparison in terms of auto-ignition properties and evaporation between DPRF58 and different PRF blends was performed in past studies [21]. Figure 3.4 shows the results of shock-tube simulations for the analyzed fuel blends. Similar ignition delay is observed in the high-temperature region, while the curves progressively diverge while moving to lower temperatures, especially in lean mixture conditions, where ignition delay of PRF0 (pure n-heptane) is significantly lower than the one of DPRF58. This aspect is confirmed also by the higher cetane number of n-C_7H_{16}, reported in table 3.6. Therefore, increasing differences between the simulated and experimental HRR and pressure profiles are expected when injections are postponed, due to decreasing bulk-gas temperature. Good agreement can potentially be achieved in the SSEp17b and SSEp17b cases, where fuel is injected when in-cylinder temperature is around 900 K.

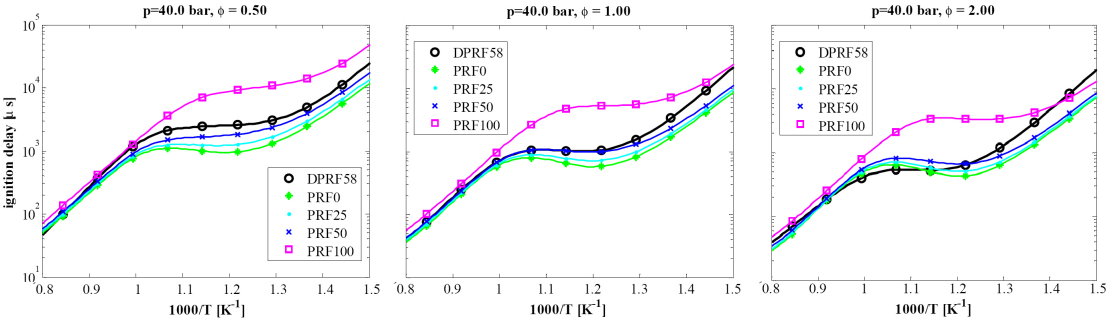

Figure 3.4: *Comparison of self-ignition properties for DPRF58 and many PRF fuel blends, for lean, stoichiometric, and fuel-rich mixtures. [21]*

	LHV [MJ/kg]	CN
DPRF58	43.892	50.7
n-C_7H_{16}	44.566	56

Table 3.6: *Fuel properties for DPRF58 and n-C_7H_{16}*

To compute the thermophysical properties of the liquid phase, the model from Sazhin was used [50], resembling the most important physical and thermal properties of conventional diesel fuels.

To facilitate the quantitative comparison between experimental and calculated heat release rate profiles, the injected fuel mass was scaled with respect to the Lower Heating Value (LHV) of the injected fuel, while the shape of the experimental fuel flow rate is preserved. Hence, the chemical energy injected inside the combustion chamber is the same for experiments and numerical simulations.

$$m_{\text{n-C}_7\text{H}_{16}} = m_{\text{DPRF58}} \frac{LHV_{\text{DPRF58}}}{LHV_{\text{n-C}_7\text{H}_{16}}} \tag{3.4}$$

However, it could be objected that even if the injected chemical energy is preserved, changing the injected fuel mass flow rate and fuel thermophysical properties could potentially affect the spray dynamics. In fact, the fuel speed at injector orifice is computed from the fuel mass flow rate, through the continuity equation at the outlet section of injector:

$$\dot{m}_f = \rho_f U_f A_{eff} \tag{3.5}$$

$$U_{surr} = U_{exp} \underbrace{\left(\frac{LHV_{exp}}{LHV_{surr}}\right)}_{\sim 0.985} \underbrace{\left(\frac{\rho_{exp}}{\rho_{surr}}\right)}_{\sim 0.91} \sim 0.9 U_f \tag{3.6}$$

Where A_{eff} is the effective nozzle area, subscript *exp* refers to the real fuel used in experiments (DPRF58), and subscript *surr* to the surrogate fuel. Equation 3.6 highlights that while changes in LHV have a negligible effect, the density difference between conventional diesel fuel ($\sim$ 860 g/l) and the real fuel mixture ($\sim$ 780 g/l) leads to a reduction of injected fuel speed of about 10%. This may lead to underestimation of fuel penetration and differences in spray/wall interaction.

3.2.3 Injector and spray modeling

Fuel spray was modeled with the Lagrangian parcel approach; coupling of the Eulerian and Lagrangian fields is performed with the procedure proposed by Nordin

in [43]. Due to its small mass, only 5 000 parcels were used for the pilot injection, while 30 000 were used for main injection. Parcels injected were initialized with the same size of the injector hole, being that past numerical studies observed that discharge coefficient of injectors with k_s type nozzles is really close to 1 [16].

Spray primary and secondary breakup were modeled with the hybrid Kelvin-Helmholtz and Rayleigh-Taylor instability model proposed by Han and Reitz [60]; both KH and RT breakup were inhibited on stripped parcels, to avoid that an excessive number of parcels is generated. Values of spray sub-models' constants used in this work are listed in table 3.7. To reduce the computational time, also considering that the spray is evaporating and plume to plume interaction is negligible, no collision model was used in this study. To simulate the liquid fuel film generated from impinging of liquid spray on piston wall, spray/wall interaction was modeled as an anelastic collision with elasticity coefficient of 0.1; hence, particles have really low residual velocity after they hit the the piston surface. The set of sub-models to describe the fuel spray is summarized in table 3.8.

KH model constant	B_0	0.61
KH model time constant	B_1	25
RT model time constant	C_τ	0.2
RT model size constant	C_{RT}	0.2
Stripped parcel mass limiter	$m_{s,lim}$	0.03
Threshold Weber number	We_{lim}	6
Breakup constant	C_b	25

Table 3.7: *Values of KHRT model constants*

Although multiple correlations are available to model the spray cone angle with respect to injection conditions (the reader can refer to [18] for an overview of spray models proposed in literature), in this study an injector model with constant spray cone angle was used. This choice was driven by the following considerations:

- Correlations are mainly based on fuel properties, such as fuel density, which have already been proven to differ from those of the real fuel used in experiments. Moreover, the ratio between injector nozzle length and diameter is usually required, which is not known in the present study;
- Predicted spray cone angle can significantly change depending on the model used, thus impacting on air-fuel mixture formation and liquid jet penetration;

- Most of the models are based on empirical correlations, which have been developed with cylindrical injector nozzles and do not account on the internal injector shape. However, past experimental and numerical studies have shown that nozzle tapering and rounding of inlet edge can have significant impact on the spray topology. Injectors with k-s shape, like the one used in ECN engine, tend to produce more collimated sprays with respect to cylindrical ones, with increased penetration and reduced cone angles [16, 52].

Hence, spray cone angle was set as an independent parameter. For the first cases, a baseline value of 15° spray spreading angle will be considered. Then, the sensitivity of the numerical models studied in this work will be assessed, and an optimal value for cone angle will be deduced.

Injector	Constant angle
Breakup	Hybrid Kelvin-Helmholtz, Rayleigh-Taylor instability
Collision	None
Heat transfer	RanzMarshall
Evaporation	Standard
Drag	Standard
Turbulent dispersion	None
Wall interaction	Reflection (elasticity = 0.1)

Table 3.8: *Set of spray sub-models used in this work*

3.2.4 Combustion models' parameters

For what concerns the RIF model, it was chosen to use a single flamelet per injection in the first analyses, while the sensitivity of the model to the number of flamemets will be assessed separately. As mentioned in section 1.2, past numerical studies performed on this engine proved that ignition in the main injection is driven by the interaction with the hot gases generated by the pilot flame. Moreover, Felsch et al. studied the performances of RIF combustion model applied to a split-injection Diesel combustion mode similar to the one investigated in this thesis, and observed that without interaction among flamelets from different injection events the ignition delay of main injection were strongly over-predicted [12] . For this reason it was chosen to account on energy and mass transfer among flamelets through the Attack flamelet interaction model, by them proposed. A detailed description of the formulas describing interaction between flamelet domains and their implementation in the LibICE code can be found in Colombi [44].

However, it was also proven that mRIF model is able to reproduce flame stabilization mechanism only if with non-interacting flamelets. Therefore, when the effect of number of flamelets will be assessed, no interaction will be allowed among flamelets associated to the same injection event. This trade-off is expected to allow prediction of pilot-main interaction and stabilization of the main combustion event.

Concerning the TWM model, the ranges of initial pressure, unburned gas temperature, and mixture equivalence ratio[2] used for table generation are listed in table 3.9. As mentioned before, during tabulation the air-fuel mixture was assumed as a perfectly stirred gaseous mixture (no mixing-line assumption), thus the T_u in the tabulation is independent from Z, and assumes the values listed in the input file. A single tabulation was used for all the operating conditions, since they have the same air composition at IVC.

p [bar]	20, 30, 40, 50, 60, 70, 80
T_u [K]	500, 525, 550, 575, 600, 650, 700, 750, 800, 850, 900, 950, 1000, 1100, 1250
ϕ	0.00, 0.05, 0.10, 0.15, 0.20, 0.25, 0.30, 0.35, 0.40, 0.45, 0.50, 0.60, 0.65, 0.70, 0.75, 0.80, 0.85, 0.90, 0.95, 1.00, 1.05, 1.10, 1.15, 1.20, 1.25, 1.30, 1.35, 1.40, 1.45, 1.50, 1.55, 1.60, 1.70, 1.80, 1.90, 2.00, 2.25, 2.50, 2.75, 3.00, $1 \cdot 10^{15}$

Table 3.9: *Ranges of input conditions for tabulation of chemical kinetics*

To prevent extrapolation of reaction rate outside of the ranges in which the tabulation is defined, a threshold value of 500 K for T_u was set, under which the reaction rate is set to zero. Moreover, as anticipated in section 2.1.2, a maximum value of equivalence ration of 3 was set for computation of the reaction rate $\dot{C}$, to prevent underestimation of the ignition delay due to diffusion of progress variable in fuel-rich regions.

[2]It is equivalent to set the initial mixture fraction, being directly related to the equivalence ratio.

3.3 Tuning of volume law

By performing a simulation of the engine running in motored condition, adopting the initial conditions and geometrical parameters of the experimental setup, the obtained pressure trace strongly overestimates TDC temperature and pressure conditions. This behavior is noticeable in Figure 3.5, comparing the motored pressure trace between the experimental measurements and the numerical simulations. The latter strongly overestimates the peak pressure, as it was already observed in many studies [17, 19, 59, 7]. The authors investigated the possible reasons of this sensible misalignment between simulations and experiments: increased exchange due to the presence of deep crevice, thermal expansion of the fused silica piston head, blow-by effect through crevice, etc. However, none of these effects are expected to induce such a strong inconsistency.

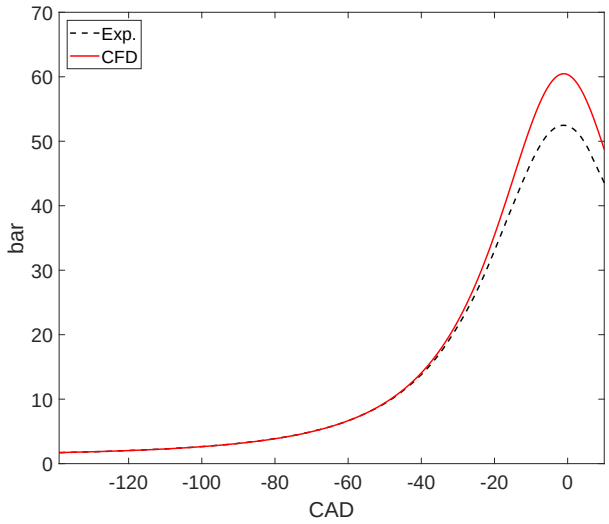

Figure 3.5: *Motored pressure trace with nominal geometry: comparison of experimental measurements (dotted line) and numerical simulation (continuous line).*

By performing measurements on another optical engine, Aronsson et al. [56] observed that squish height was linearly correlated with in-cylinder pressure at TDC when running motored. Hence, the authors inferred that in-cylinder volume traces in this type of engine are significantly distorted due to non-negligible compressibility of the mechanical assembly, and proposed a linear model for piston compressibility to correct the volume law. Perini et al. [19] implemented a linear compressibility model and applied it to the ECN small-bore diesel engine, obtaining good agreement with the experimental motored pressure traces.

At the moment being, no such model has been implemented yet in the software used for this study, and its implementation was out of the scope of this work. Hence, the effect of compressibility of the mechanism was simulated by changing the engine geometrical parameters to fit the pressure profile during the compression stroke. Before describing the methodology used to tune the engine parameters, the fundamental equations describing piston motion and evolution of in-cylinder volume will be briefly summarized.

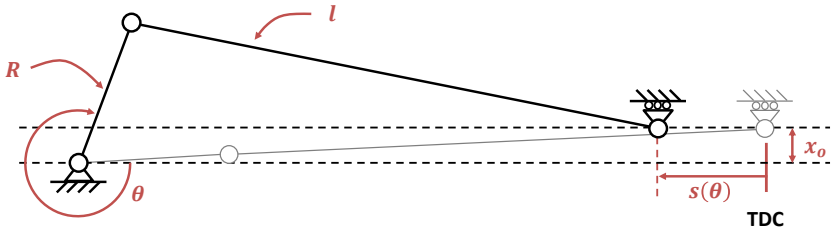

Figure 3.6: *Scheme of engine mechanism*

Figure 3.6 represents the scheme of crankshaft/connecting-rod mechanism, which controls piston motion. The coordinate of piston position is defined to be null when the piston is at TDC, and it is described by the following formula:

$$s\left(\theta\right) = \left(l + R\right)\cos\left(\theta_{TDC}\right) - R\cos\theta - l\cos\left(\sin^{-1}\left(\frac{R\sin\theta + x_o}{l}\right)\right) \tag{3.7}$$

$$S = 2R\cos\left(\theta_{TDC}\right) \tag{3.8}$$

$$\theta_{TDC} = -\sin^{-1}\left(\frac{x_o}{R+l}\right) \sim -0.43\text{CAD} \tag{3.9}$$

Being the cosine of θ_{TDC} really close to unity, and introducing two non-dimensional parameters for connecting rod length and pin offset, $s(\theta)$ can be rewritten as follows:

$$s\left(\theta\right) = S\underbrace{\left\{1 - R\cos\theta + \lambda\left[1 - \cos\left(\sin^{-1}\left(\frac{\sin\theta + \delta}{\lambda}\right)\right)\right]\right\}}_{\psi_s(\theta)} \tag{3.10}$$

$$\lambda = \frac{l}{R} \qquad \delta = \frac{x_o}{R} \tag{3.11}$$

The instantaneous volume inside the cylinder can be expressed as the sum of the combustion chamber volume, i.e., the in-cylinder volume when the piston is at TDC (V_{TDC}), and the instantaneous displacement volume ($V_d(\theta)$), which can be computed from the instantaneous piston position. Then, by exploiting the definition of compression ratio, the volume law can be expressed with respect the geometric coefficients as follows:

$$V(\theta) = \underbrace{\frac{\pi S D^2}{4}}_{V_c} \left[\frac{1}{r-1} + \psi_s(\theta) \right] \tag{3.12}$$

Therefore the shape of in-cylinder volume trace is parametrized with respect to three non-dimensional parameters: r, λ and δ. These parameters have been tuned in order to fit the CFD motored pressure trace to the experimental one. Before setting up the fitting algorithm, the impact of each parameter on the pressure trace was studied independently.

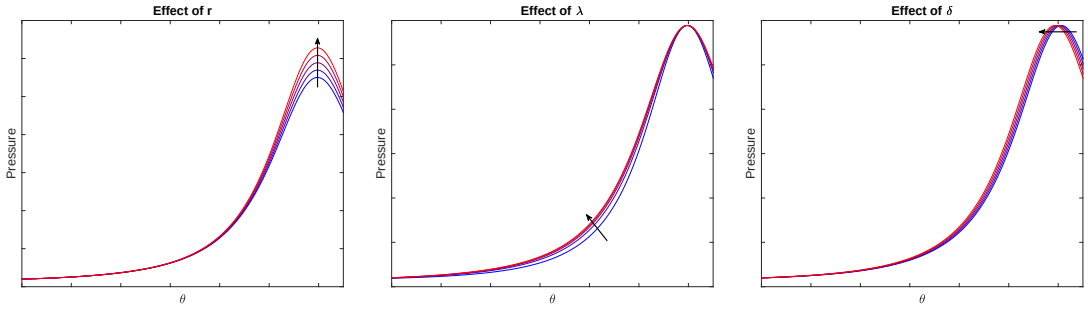

(a) **(b)** **(c)**

Figure 3.7: *Behavior of pressure trace plots when geometrical non-dimensional parameters (a) r, (b) λ and (c) δ are varied. Black arrows indicate increasing values of the parameter, as does the curve color (from blue to red).*

Figure 3.7 shows the overall effect of the aforementioned geometrical parameters on the pressure trace:

- As expected, the compression ratio controls the peak pressure value. By increasing the compression ratio, the maximum pressure is increased;

- λ determines the steepness of pressure profile. By increasing the connecting-rod length parameter, steepness of pressure trace is reduced during compression stroke;
- As anticipated by equation 3.9, δ controls TDC timing. Increasing values of δ lead to anticipation of TDC.

Therefore, r was used as control variable to tune the maximum pressure, λ to fit the rate of pressure rise along compression stroke, and δ to guarantee that peak pressure instant is correctly phased. Hence, the following tuning algorithm was adopted:

1. Values of λ_0, and δ_0 are inizialized to their to nominal values, while a first-attempt value of compression ratio is estimated by assuming polythropic compression from IVC to TDC with index $n = 1.3$:

$$r_0 = 1 + \frac{\left(\frac{p_{TDC}}{p_{IVC}}\right)^{1/n} - 1}{\psi_s(\theta_{IVC})} \sim 13.9$$

2. The compression ratio is tuned so that the difference between experimental and computed pressure at IVC is under a threshold value $\bar{e}_p$;
3. Once the required TDC pressure is achieved, the shape of pressure trace during compression stroke is fitted through the parameter λ, by minimizing the mean squared error between experimental and computed pressure trace (e_{mq}). However, λ slightly affects also the TDC timing and maximum pressure. The former is compensated by acting on the value of δ, which is obtained from equation 3.9, while the second requires to perform an additional tuning loop on the compression ratio.

$$\delta_{j+1} = \delta_j \frac{1 + \lambda_{j+1}}{1 + \lambda_j}$$

4. The algorithm is terminated once conditions on peak pressure error and mean squared error of pressure during compression are both satisfied.

A flow-chart of the tuning algorithm is depicted in figure 3.8a; the geometrical parameters found from the tuning algorithm are listed in table 3.10, while the final pressure trace is shown in figure 3.8b.

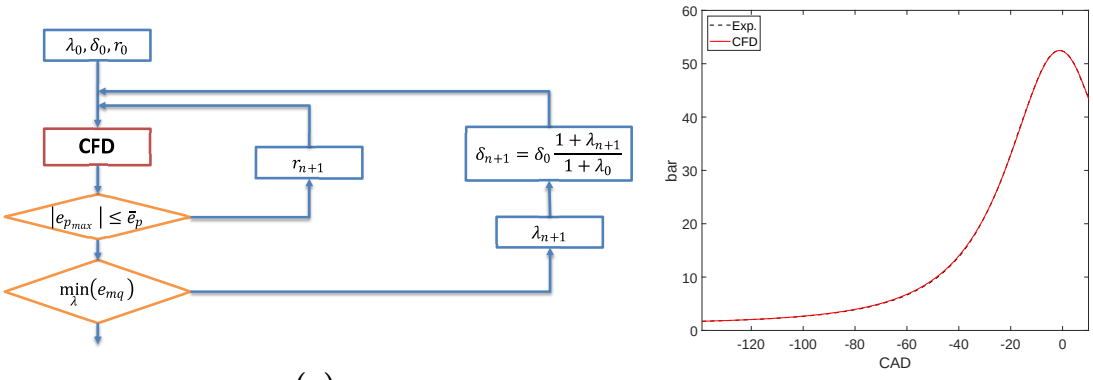

Figure 3.8: *(a): Flow-chart of the tuning algorithm for fitting of pressure trace - (b): Pressure trace obtained from the presented tuning algorithm*

r	14.31	
l	216.67	[mm]
x_o	2.364	[mm]
H_s	2.04	

Table 3.10: *New geometrical parameters from tuning of pressure trace*

Interval [CAD]	Nominal	New
$[-120, -80]$	1.393	1.362
$[-80, -40]$	1.333	1.361
$[-40, -5]$	1.191	1.309
$[-120, -5]$	1.282	1.340

Table 3.11: *Polythropic index along compression stroke*

It should be observed that past studies on this engine deduced an effective compression of this engine in the range $[13.9, 14.5]$, which is consistent with the value obtained from the above mentioned procedure. Moreover, an average equivalent stiffness of the assembly can be computed through the increased squish height and the mechanical loading due to in-cylinder pressure at TDC, obtaining a value of $4.34\,10^7$ N/m, which is consistent to the value of $4.5\,10^7$ N/m found by Perini et al. while tuning their linear stiffness model. Finally, the results were assessed by computing the polythropic index over multiple intervals of compression stroke, which are shown in table 3.11. With the nominal parameters, the polythropic index changes significantly during compression stroke, while with the new ones most of compression has a n close to 1.4, which is consistent with the common assumption of nearly adiabatic compression. Hence, after all these considerations, the results of this tuning procedure were thought to be satisfactory.

For the sake of completeness, it must be pointed out that the evolution of in-cylinder pressure is also sensible to the heat exchange through walls: increased heat transferred to combustion chamber walls leads to reduced peak temperature, and therefore pressure as well. For this reason, results of this procedure are technically sensible to the heat exchange model used to describe heat flux, and to the turbulence model, which affects turbulence levels close to walls. However, it has been observed that both of these effects play a marginal role, and only little difference was found when changing turbulence and heat transfer models for CFD computation of the motored pressure trace. Hence, for the sake of simplicity, tuning has been performed only with the k-ε model, adopting the consequent geometrical parameters for every simulation performed in this work.

3.4 Mesh structure

It is well known in the literature that mesh structure and its refinement can have a significant impact on the results of CFD simulations. This effect is even more critical in simulation of Diesel engines: in addition to the gaseous phase (Eulerian), injection of highly pressurized liquid fuel needs to be modeled. Conventionally this is done by means of a Lagrangian parcel approach [45], where the liquid phase is modeled as an ensemble of small droplets dispersed in a gaseous phase of much wider volume. However, it has been proven that this formulation can have strong sensitivity to the mesh morphology [5, 53, 55], especially in predicting liquid spray penetration and vapor distribution. For this reason, it is noteworthy to briefly discuss the choice of the mesh structure used in this work.

3.4.1 Layering technique

Regarding mesh structure of sector mesh simulations for Diesel engines, two main approaches are conventionally adopted in the literature:

- Polar-Cartesian mesh structure, where in azimuthal cross sections the cell edges are mostly aligned towards radial and axial directions;
- Spray oriented mesh structure, in which the cells in the spray region are aligned with the spray direction, so that parcels cross cell faces almost orthogonally.

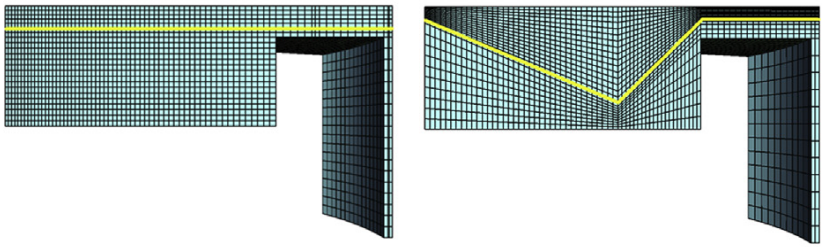

Figure 3.9: *Conventional mesh structures for sector-mesh simulations [5]*

In addition to the mesh structure at TDC, these differ also in how dynamic mesh layering for piston motion is performed. In the former, the surface used for generation of the layering cells is a plane orthogonal to the cylinder axis. In the latter, the mesh is divided into two regions - spray oriented cells, jointed to the cylinder head, and the other cells, moving with the piston surface - and the interface between them is used for mesh layering. Figure 3.9 shows a the concept behind these two mesh structures, while the surfaces used in this work for dynamic mesh layering are represented in figure 3.10.

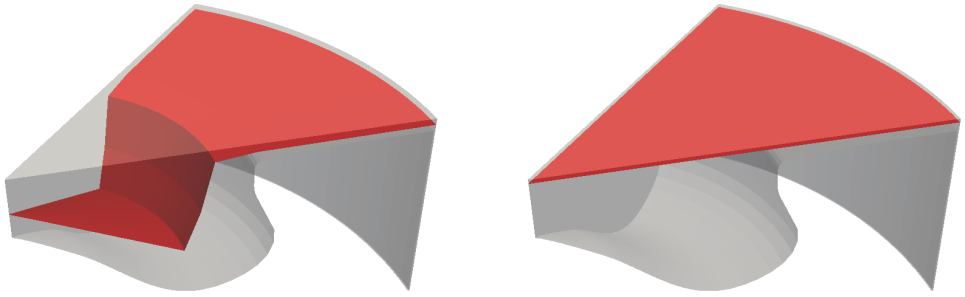

(a) **(b)**

Figure 3.10: *Surfaces used for dynamic mesh layering. (a): Spray-oriented mesh layering - (b): Layering parallel to cylinder head*

These two mesh structures have been assessed by simulating the SSEp07b test condition, and their performances have been compared. Although little differences are observed in terms of liquid spray structure and penetration when the two meshed are applied, the Eulerian fields experience significant dependency on mesh structure (figure 3.11).

First, in the case of spray oriented mesh strong numerical diffusion is induced when the spray crosses the layering cells, and turbulent kinetic energy is significantly spread towards the periphery of the spray. Moreover, the use of a

layering surface parallel to the cylinder head prevented the generation of highly non-orthogonal surface during layering, which are presumed to be the cause of the strong numerical diffusion.

This aspect can significantly affect the air-fuel mixture distribution, as turbulent kinetic energy is directly related to turbulent mixing. With spreading of TKE, fuel vapor is expected to diffuse further from the spray axis. Hence, equivalence ratio in the core of the spray is reduced and degree of premixed combustion is increased. Therefore, this issue could have significant impact on prediction of heat release rate and particulate matter formation.

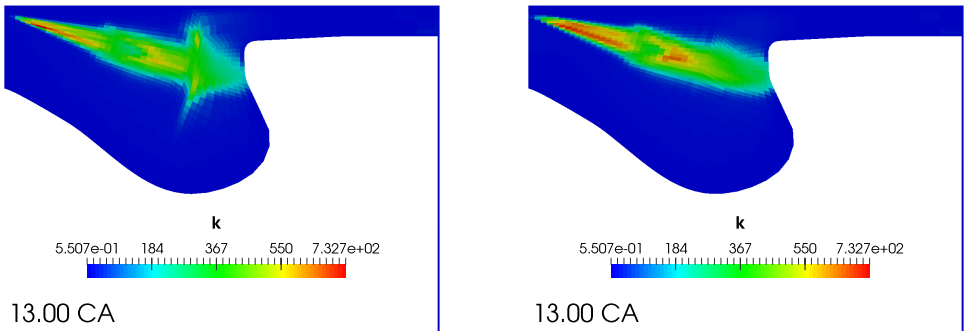

Figure 3.11: *Impact of mesh layering strategy on TKE field in main injection. (a): Spray-oriented mesh layering (b): Planar mesh layering*

For these reasons, although past studies showed that the adoption of spray oriented meshes reduces the mesh dependency of simulations [5] and gives better results in terms of spray penetration, it was chosen to use the polar-Cartesian mesh structure in this work. Moreover, a large portion of this study concerned assessing the impact of turbulence modeling on mixing-controlled combustion, hence a reliable prediction of the distribution of turbulent kinetic energy was mandatory.

3.4.2 TDC mesh structure

Once the mesh structure was chosen, the final step was to optimize mesh the resolution. As previously mentioned, this is not trivial, due to the intrinsic mesh dependency of Lagrangian sprays. Specifically, the source of mesh-dependency is the momentum coupling of Eulerian and Lagrangian fields: computation of momentum exchange is based on the assumption of small droplets, compared to

the volume of cells in which are located. Hence, the choice of the most appropriate level of refinement is driven by two opposing requirements:

- To have correct prediction of momentum transfer due to drag from droplets to the gas, the portion of volume occupied by liquid phase in each cell (void fraction) should be sufficiently low. If this condition is not satisfied, excessive momentum is transferred to the gas phase, and the relative velocity between liquid and gas is underestimated. This significantly impacts on liquid penetration, droplet breakup, and, consequently, on air-fuel mixture formation. Therefore, a limit is imposed on maximum mesh refinement;
- The spray region is characterized by strong gradients orthogonally to the spray axis, especially close to the injector nozzle, thus a sufficiently high level of mesh refinement is required for their correct description. If an excessively coarse mesh is used, numerical diffusion is enhanced, which leads to increased dispersion of mass and momentum further from jet axis, and, consequently, underestimation of the spray penetration.

Therefore, mesh refinement in the near-nozzle region was tuned to achieve a good compromise between capturing local gradients and maintaining a sufficiently low fraction of cell volume occupied by the liquid droplets. Figure 3.12 shows the distribution of void fraction in the spray region, for three different crank angles: in the vast majority of cells on the spray axis have less then 10% of volume occupied by liquid fuel, while only a couple of cells reach values of 20% or more at nozzle orifice.

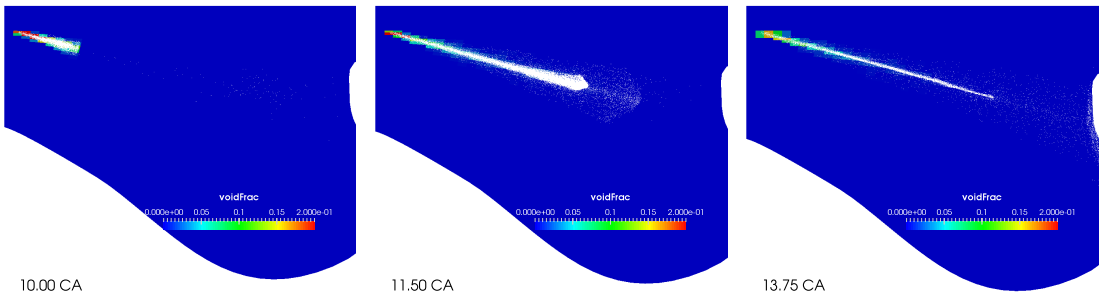

(a) **(b)** **(c)**

Figure 3.12: *Volume fraction occupied by liquid parcels*

Hence, the final mesh structure shown in figure 3.13 is thought to be a good compromise in terms of mesh refinement, achieving globally low values of void

fraction, along with an average mesh size of ~ 0.15 mm in the near nozzle region. Dynamic mesh layering is performed through a graded function, with minimum cell height of 0.15 mm close to TDC and maximum height of 1 mm at mid-stroke. The number of elements in tangential direction was set at 20, which is a compromise between resolution in squish region and computational load. The overall mesh size ranges from nearly 40 000 cells at TDC to about 110 000 at IVC.

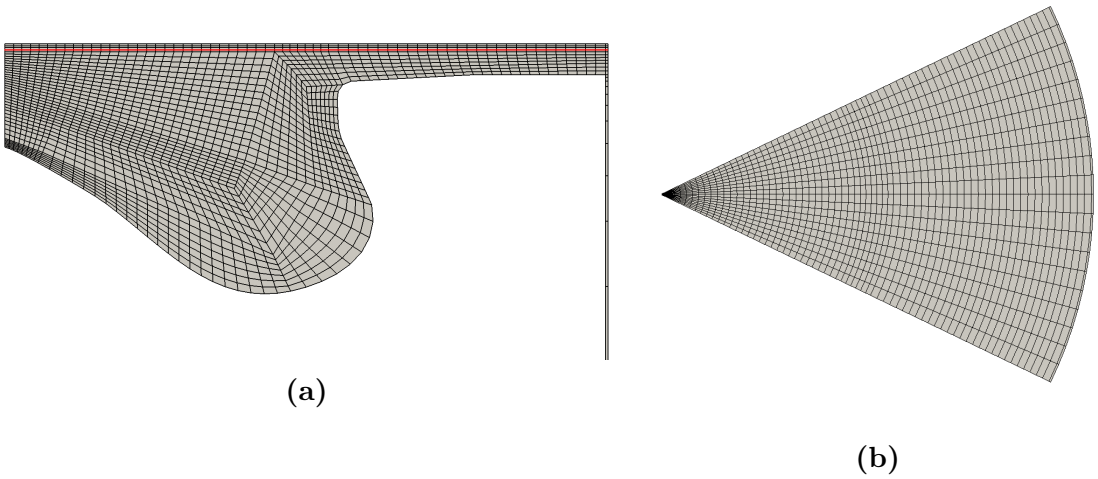

(a) **(b)**

Figure 3.13: *TDC mesh structure. (a): Azimuthal cross section, with the axis-orthogonal layering plane represented by the red line - (b): Top view*

Chapter 4

Sensitivity analysis

This chapter will be focused on understanding how combustion and turbulence modeling affect ignition and flame development in mixing-controlled diesel combustion, and assessing their sensitivity to several parameters. Specifically, the analysis will be organized as follows:

1. The two combustion models are compared in a baseline case, to assess their differences in describing the main features of this combustion strategy;

2. Afterwards, the effect of turbulence modeling are studied. To understand its impact on combustion development, the results are post-processed in terms of in-cylinder distribution of turbulent quantities, which drive spray structure and air-fuel mixture formation;

3. Once that the main features of the turbulence and combustion models are well-known, the models are assessed in multiple injection conditions, and they are validated against the experimental pressure traces and heat release rate curves;

4. The fourth section is focused on assessing the sensitivity of each model with respect to the spray spreading angle imposed at the outlet of injector orifice. This gives a measure of the capability of each model to appreciate changes in spray structure and injector design;

5. As previously observed in section 2.1.1, the capability of RIF model to fully appreciate the flame structure in burning sprays is affected by the number of flamelet domains used to model the injected fuel. To this end, in last section the sensitivity of this model with respect to the number of flamelet domains is studied.

4.1 Effect of combustion modeling

First of all, it was chosen to analyze in depth the behavior of the two combustion models applied to part-load diesel combustion with split-injection. Precisely, the objective is to assess the capability to reproduce ignition and combustion of pilot injection, its role in ignition of fuel from main injection, and development of mixing-controlled combustion. This preliminary study has been performed by simulating the SSEp07b injection strategy, adopting a baseline spray cone angle of 15°, and modeling turbulence with the standard k-ε closure. Regarding the RIF model, a single flamelet domain has been used for each injection, and the Attack interaction model has been used to describe heat and mass exchange among flamelets.

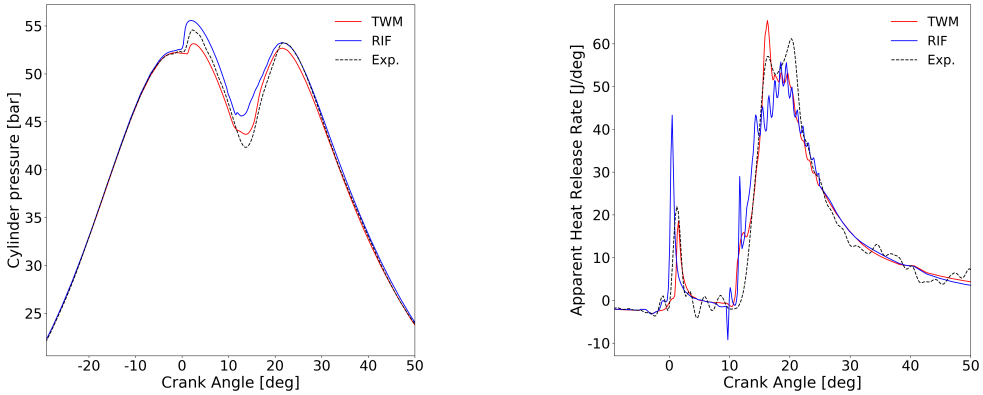

(a) **(b)**

Figure 4.1: *Comparison of TWM and RIF models: pressure and aHRR profiles*

Figure 4.1 illustrates the results of TWM and RIF combustion models, in terms of pressure traces and apparent heat release rate[1] curves, compared with data from experimental measurements. Although both models show a fairly good agreement with the experimental curves, especially with regards to aHRR, some peculiar differences are present:

- RIF model shows shorter ignition delay in pilot injection, with strongly overestimated peak of aHRR and pressure rise, while TWM has the completely opposite behavior;

[1]The instantaneous aHRR is computed by post-processing the in-cylinder pressure trace through a simple 0-D thermodynamic model, which is briefly reported in Appendix A.

- Both combustion models show slightly anticipated ignition of main injection. Even though none of the two models seem to be capable of correctly describe the "double-peak" shape of aHRR curve during main combustion, only TWM model has at least first peak correctly phased.

To identify the root causes of these dissimilarities, a deeper analysis of combustion development is required. This will be done in the two following paragraphs, by post-processing the local distribution of main physical quantities.

4.1.1 Pilot injection

Combustion of complex hydrocarbons, like those used in CI engines, is characterized by a two stage combustion. During the first one, called cold flames, complex molecules break into simpler ones and are partially oxidated. In this step of combustion the temperature rise is minimal, because most of the energy released is used for sustaining chemical reactions. Once a high enough portion of fuel is partially oxidated, a positive net energy balance is reached, and main ignition starts.

In the set of species available for post-processing, carbon monoxide is representative of the products of partial oxidation. Hence, it can be used as a measure for development of low/medium temperature reactions. Figure 4.2 shows the azimuthal distribution of CO mass fraction on a plane slicing the spray through its axis (see figure 4.7).

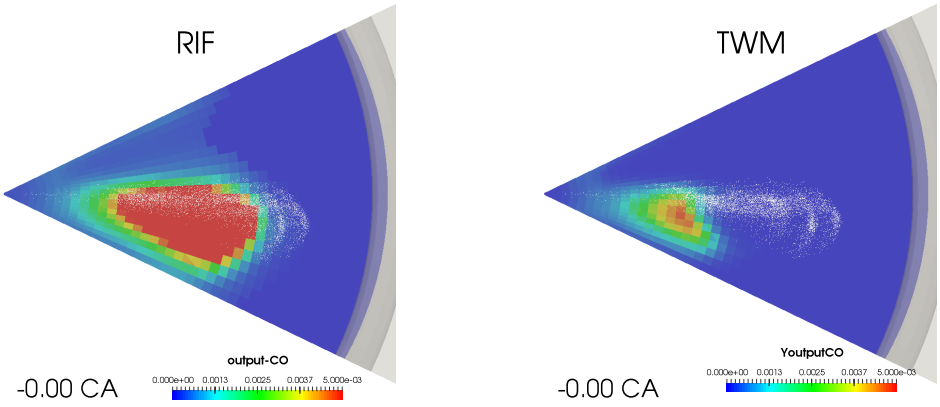

Figure 4.2: *Development of cold flames in pilot injection - Distribution CO mass fraction slightly before ignition*

Looking at the results for the RIF model, cold flame reactions are widely spread

in the air-fuel mixture, with increasing production of CO in central region of the spray. Significant differences are observed in the case of TWM model, where CO is found only in the region close to the injector nozzle. The reason why cold flames develop from the root of the spray with this combustion model can be deduced by looking at the in-cylinder distribution of equivalence ratio, depicted in figure 4.3. Evaporation of liquid spray generates a relatively wide area with fuel-rich mixture. However, as described in section 2.1.2, in TWM model reaction rate is set to zero in cells where $\phi > 3$, to prevent anticipated ignition or rich regions due to transport of progress variable. Therefore, development of partial oxidation reactions is inhibited in the center of air-fuel mixture cloud, which contains the majority of injected fuel, until the charge is sufficiently diluted.

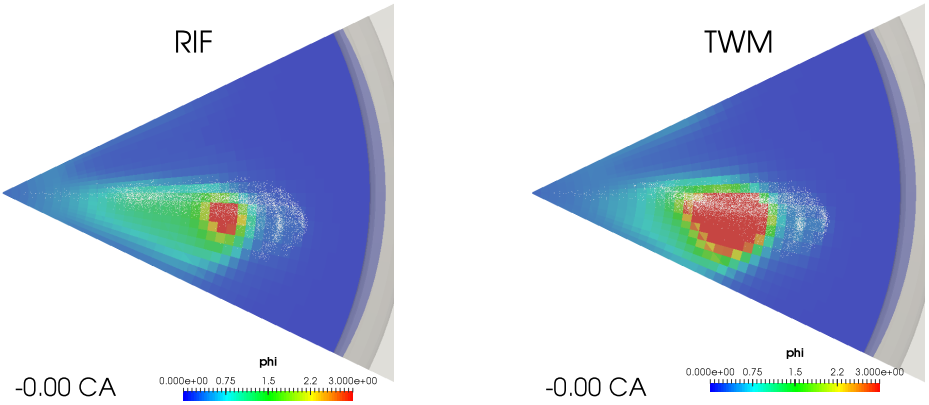

Figure 4.3: *Equivalence ratio distribution in pilot injection*

Likewise, the differences in peak aHRR and pressure rise are induced by this artificial delaying of chemical reactions, but it is not the only aspect involved. Looking at figure 4.4, sensible differences can be observed in the in-cylinder temperature distribution generated from combustion of pilot injection. With the RIF model the hot gases from pilot combustion are more widespread inside the bowl, while with TWM they are confined in a smaller region. The probable reason of this significant difference is the absence of turbulence-chemistry interaction in the TWM model, which reduces the capability of the flame to propagate towards leaner regions. This issue is enhanced by the increased ignition delay, because fuel had more time to diffuse, further reducing capability of flame diffusion. Therefore, a significant portion of fuel introduced in pilot injection is not burnt with TWM combustion model. On the contrary, because only one flamelet domain is used with the RIF model, capability of flame propagation toward diluted mixtures is enhanced. Therefore, combustion efficiency is overestimated, and excessive thermal energy is released.

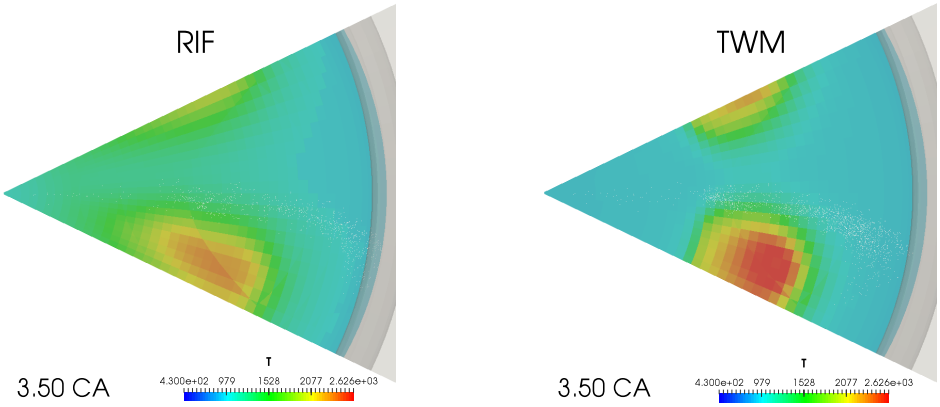

Figure 4.4: *Combustion of pilot injection - temperature distribution*

4.1.2 Main injection

Even though the two combustion models showed significant differences in ignition timing of pilot injection, and in the subsequent in-cylinder temperature distribution, they predicted the same instant of ignition for the main injection. This is due to the fact that, although differences in temperature stratification are present, location of the hot gases from first combustion event is the same with the two combustion models. Hence, being that ignition of the fuel from main injection is driven by its interaction with the these hot gases [26], the same phasing is observed.

Figure 4.5 shows the evolution of temperature distribution during ignition of main injection, represented on a vertical cross section passing through the axis of the spray. As above mentioned, combustion starts when the spray reaches the region of preheated gases. While the TWM model is capable to predict the propagation of premixed flame towards the injector nozzle, with RIF combustion model the whole premixed charge is ignited simultaneously. This also justifies the sharp peak in aHRR experienced by the RIF model immediately after ignition.

To be observed that this really similar description of ignition phenomenon between the two models also demonstrates the capability of flamelet interaction models to describe the influence of pilot injection on ignition of the following one. In fact, when no interaction model was used, the spray from main injection crossed the hot gases undisturbed and ignition delay was severely over-predicted, with a strong peak of aHRR from premixed combustion.

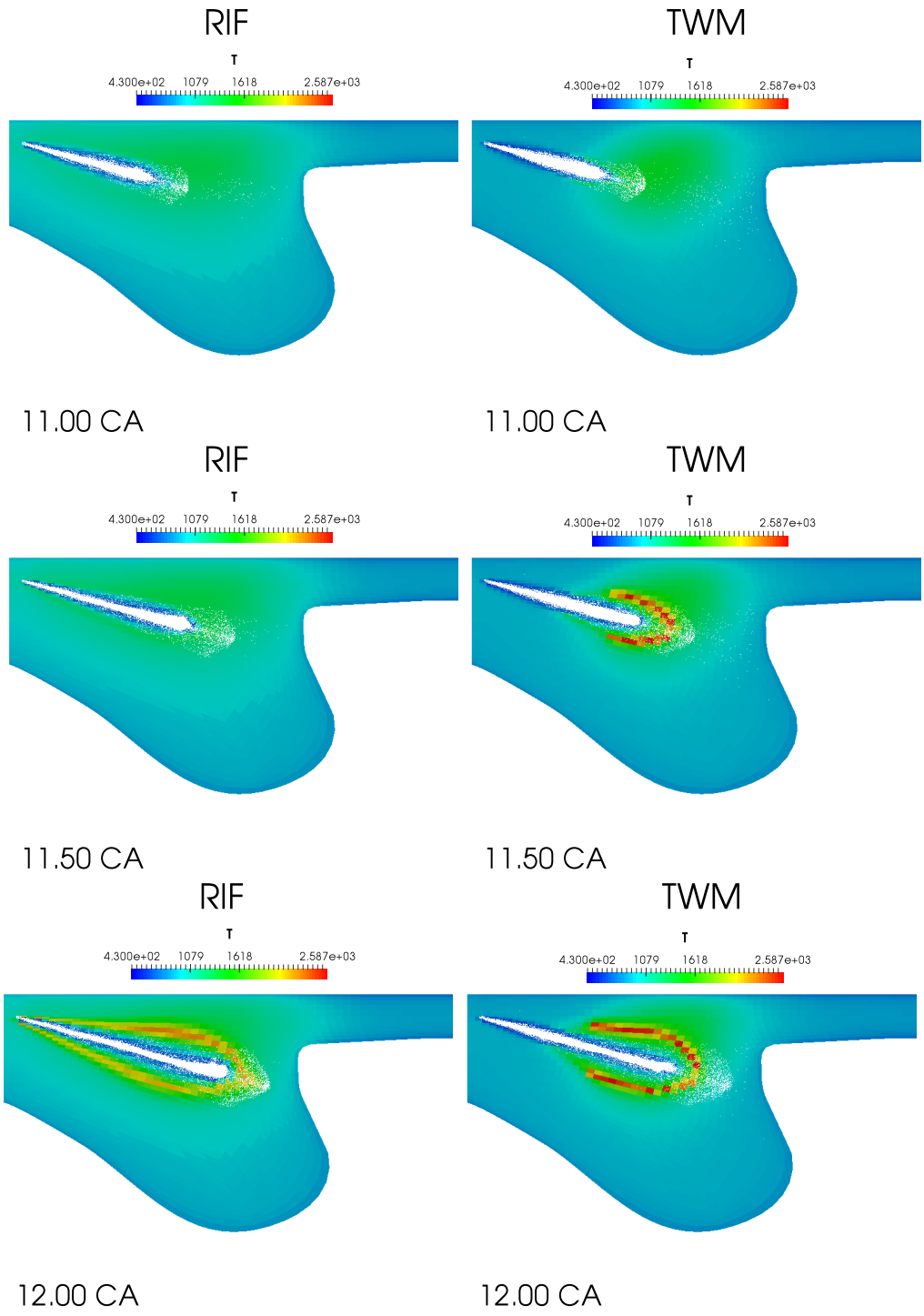

Figure 4.5: *Ignition of main injection - Temperature distribution*

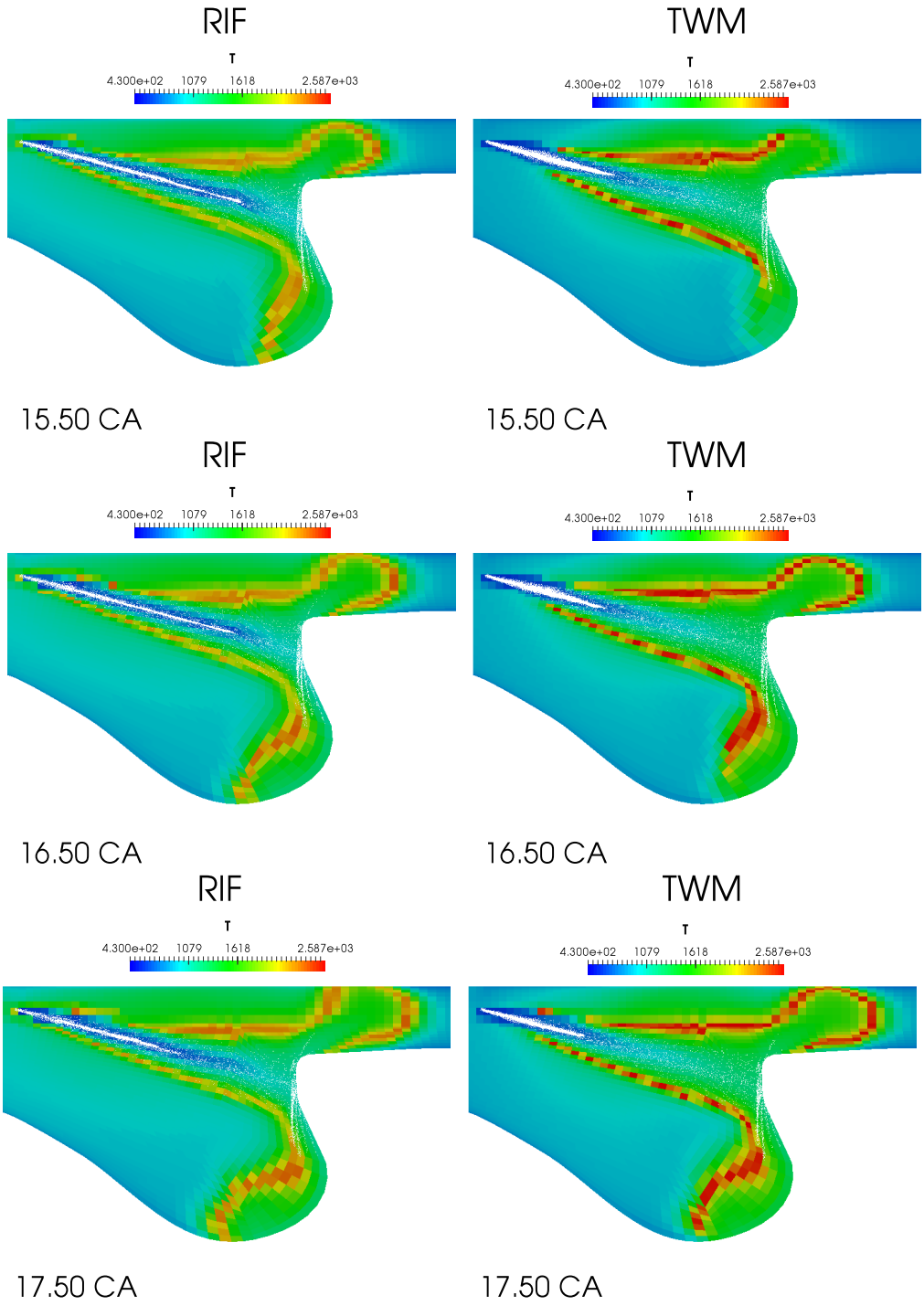

Figure 4.6: *Flame development in main injection - Temperature distribution*

Likewise, analysis of the evolution of temperature distribution can help understanding the origin of differences in peak aHRR between the two combustion models. Figure 4.6 shows the evolution of temperature field during the ramp of aHRR, for both combustion models. Sensible differences are observed between the two models:

- With RIF combustion model the flame is attached to the piston surface. Hence, the flame is diffusive and combustion is mainly mixing-controlled, driven by the high momentum of injected fuel;
- Concerning TWM model, the temperature field clearly shows that the flame structure experiences a smooth transition from propagation of premixed flame to mixing-controlled diffusive flame.

Therefore, the latter predicts constantly increasing aHRR until the flame reaches the piston surface, and fully-developed diffusive flame is reached. On the contrary, RIF model is not able to predict this behavior, and the increase of apparent heat release rate is slowed down earlier. Hence, the first peak of aHRR is assumed to be related with this flame development mechanism, while the second peak is probably driven by mixing. Therefore, the capability to predict the second peak is probably constrained by correctly describe the flow field generated by fuel injection.

After this transition, both RIF and TWM models experience fully-developed, mixing-controlled diffusive combustion, with a really similar flame structure. For this reason, their curves of aHRR almost overlap in the post-injection phase.

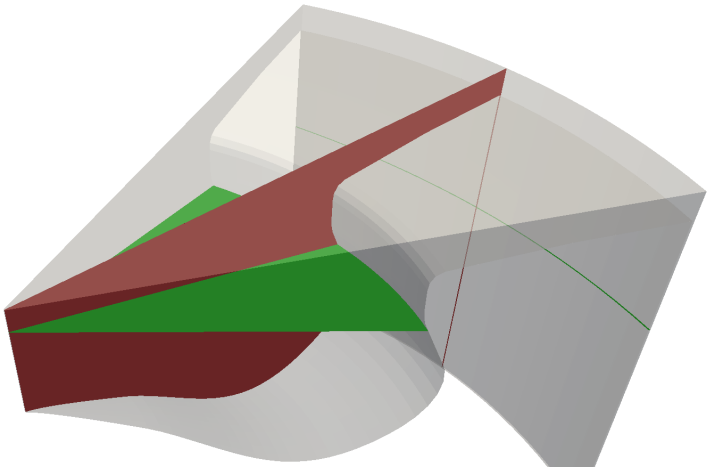

Figure 4.7: *Planes used for visualization of Eulerian fields*

4.2 Effect of turbulence modeling

As discussed in section 2.2, many studies can be found in the literature on understanding the effect of turbulence modeling in the context of compression ignition combustion. Among the changes observed when different turbulence closure are used, the most relevant in terms of combustion dynamics are those directly impacting on in-cylinder air-fuel mixture distribution. Hence, it is fundamental to investigate the evolution of spray structure and turbulence distribution to explain the variations in combustion development. As would be expected, spray structure and distribution of turbulent quantities were observed to be marginally affected by combustion modeling. Therefore, for the sake of avoiding redundancy, here they are reported only for the case of TWM combustion model.

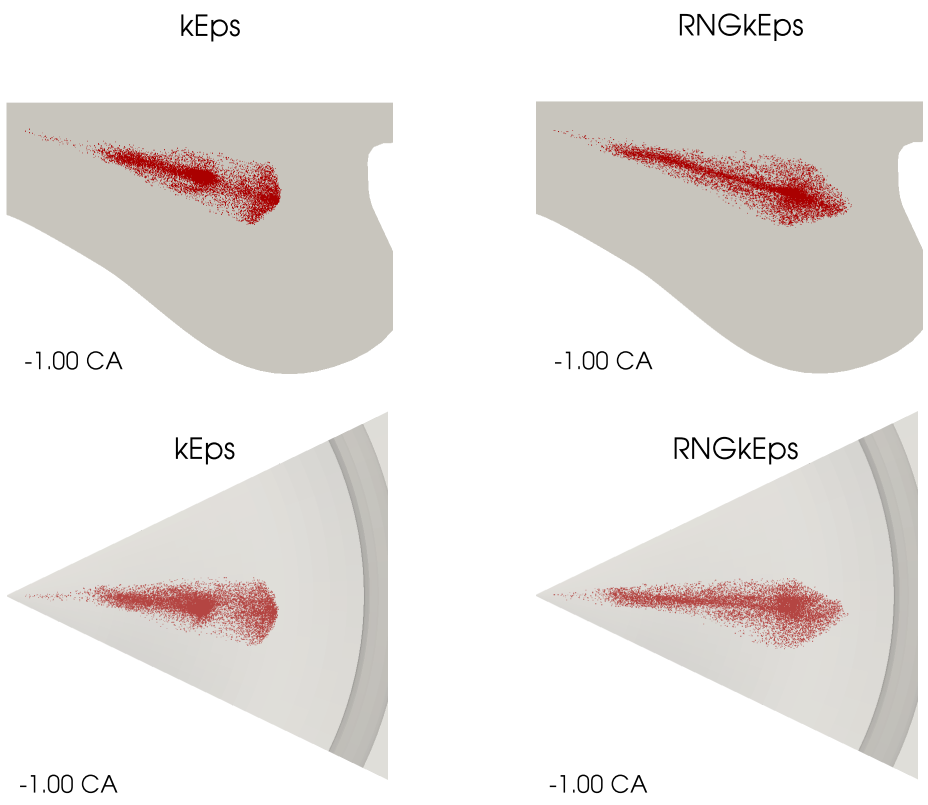

Figure 4.8: *Effect of turbulence modeling on spray structure (pilot injection)*

Figure 4.8 shows the spray structure of pilot injection for each of the two turbulence models assessed in this work. It is immediately noticeable that droplets

distribution is significantly changed when switching from the standard k-ε model to its RNG variant. While the parcels on the periphery of the spray experience similar penetration with the two models, the liquid core of the spray is projected further from the injector nozzle when the RNG k-ε turbulence model is used.

The reason of the different liquid fuel penetration can be identified when looking at the distribution of turbulent kinetic energy in the region of the spray, represented in figure 4.9. With the standard k-ε model, high TKE is observed in the central region of the spray, and it is widely dispersed in radial direction with respect to the spray axis. On the other hand, RNG k-ε model predicts globally lower TKE, and distributed closer to the liquid core of the spray.

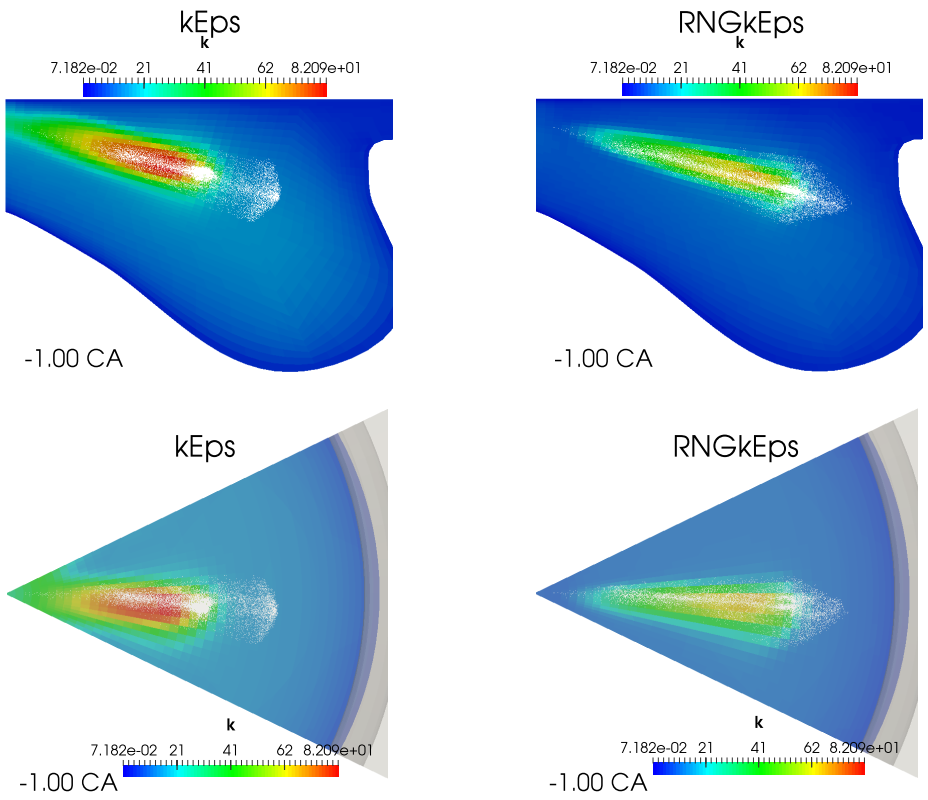

Figure 4.9: *Effect of turbulence modeling on TKE distribution (pilot injection)*

This involves that the former predicts a stronger diffusion of momentum towards the periphery of the spray. Hence, liquid parcels experience higher drag forces and their penetration is reduced. In the latter, the gradient of TKE is inside the spray region, which means that the parcels at spray boundary experience

strong drag forces, while the liquid core undergoes smaller dissipation of momentum. This behavior is in agreement with results of past studies, that showed that RNG k-ε model is less dissipative than the conventional one, and performs better in describing shear flows. The same behavior is observed during the main injection, as depicted in figure 4.10. Additionally, high turbulence is observed in the region of jet impingement, which is in agreement with the results of Perini et al. [24].

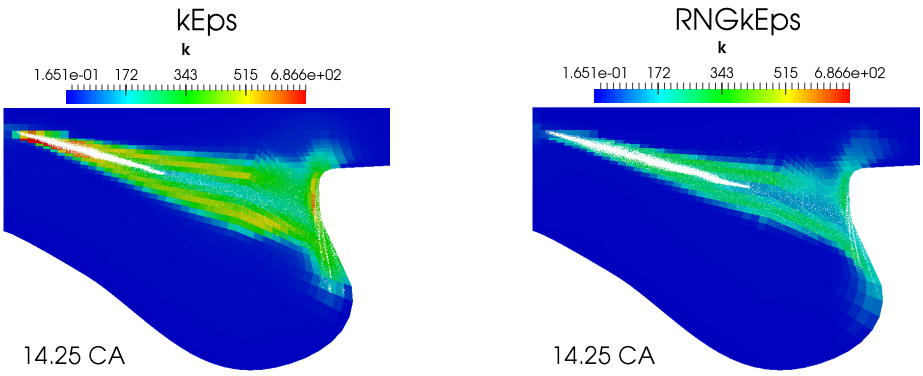

Figure 4.10: *Effect of turbulence modeling on TKE distribution (main injection)*

To fully describe the impact of turbulence modeling on air-fuel mixture formation and mixture fraction distribution, it is required to study the changes in eddy viscosity distribution, being a measure of turbulent diffusivity[2]. To this end, figure 4.11 depicts the in-cylinder distribution of turbulent dynamic viscosity (μ_t) during pilot injection, for both turbulence models. It can be seen that with RNG k-ε model μ_t is significantly lower, especially in the spray region. Hence, diffusion of chemical species due to turbulence is sensibly lower, leading to formation of a less dispersed fuel vapor cloud with locally higher equivalence ratio. This is proven in figure 4.12, which shows a comparison of the stoichiometric iso-surface (ensemble of points with equivalence ratio ϕ equal to one) during main injection. It can be seen that, in the case of RNG model, fuel vapor experiences increased penetration and reduced radial diffusion with respect to spray axis.

[2] $D_t = \frac{\mu_t}{\rho Sc_t}$

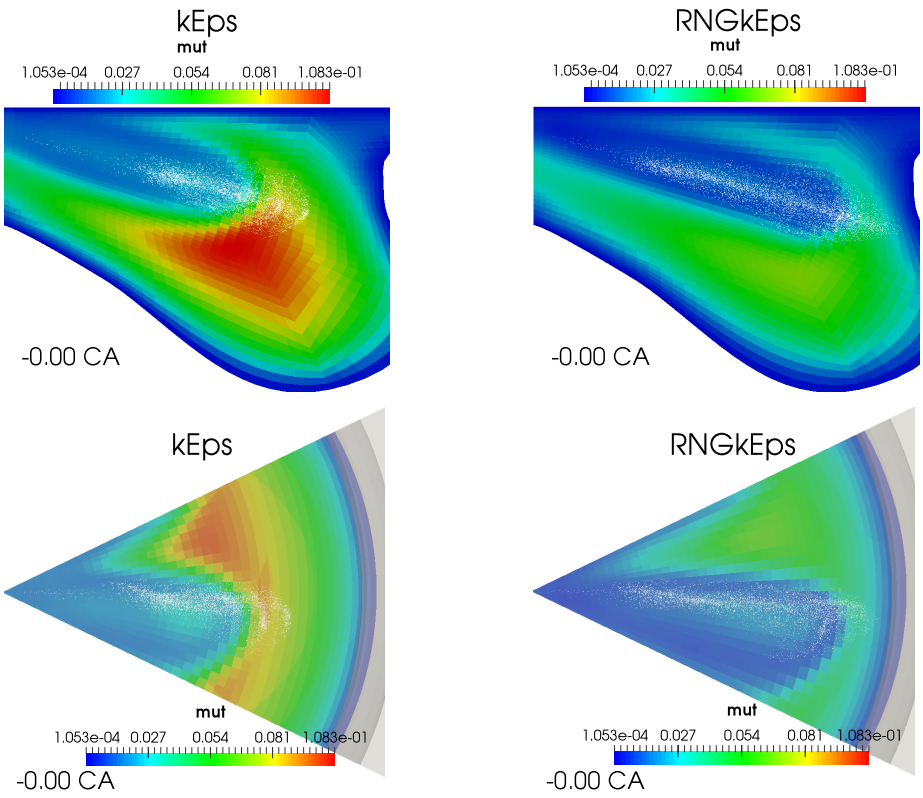

Figure 4.11: *Effect of turbulence modeling on distribution of turbulent dynamic viscosity (pilot injection)*

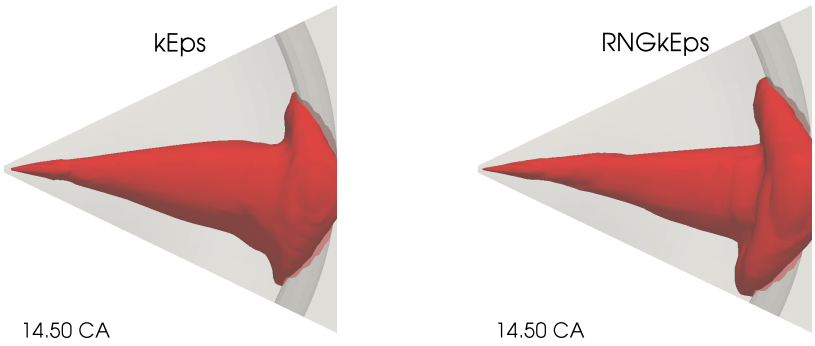

Figure 4.12: *Effect of turbulence modeling on the development of stoichiometric iso-surfaces ($\phi = 1$) in main injection*

After this detailed analysis of the impact of turbulence modeling on spray structure, liquid fuel penetration, and mixture fraction distribution, it is possible to make comparisons in terms of combustion dynamics. Figure 4.13 shows how the in-cylinder pressure trace and aHRR in the SSEp07b condition are affected by turbulence modeling, for both TWM and RIF combustion models. These graphs highlight that both combustion models are sensitive to turbulence modeling, and it is noteworthy to discuss the origin of their behavior.

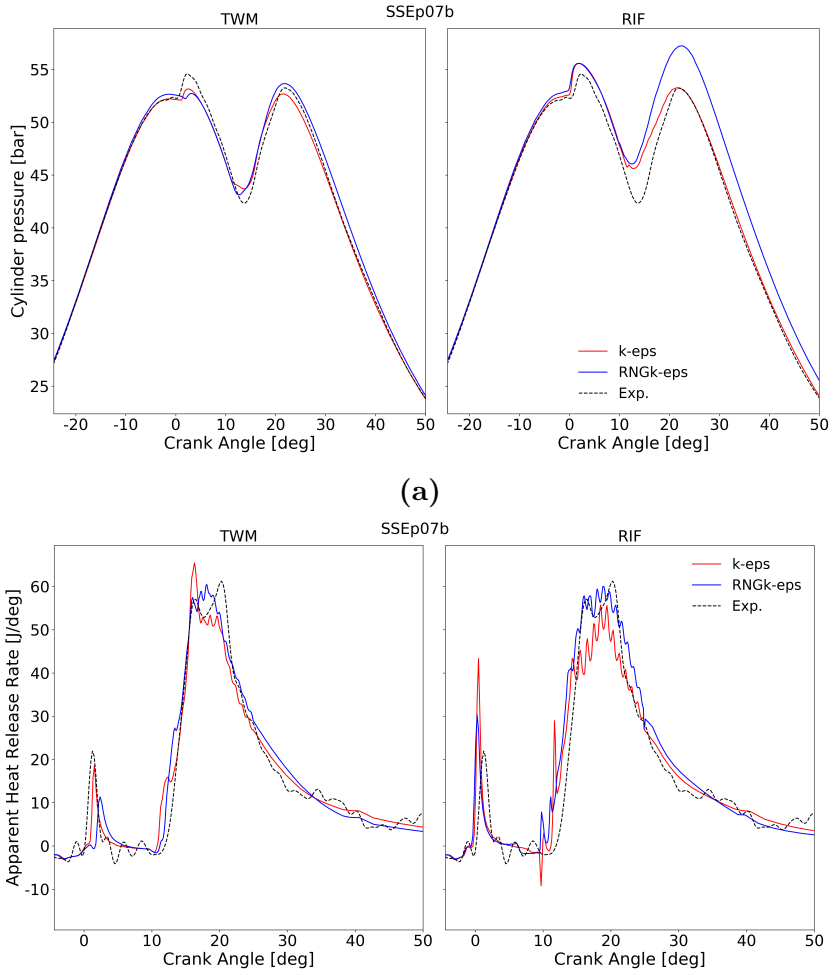

Figure 4.13: *Effect of turbulence modeling: pressure and aHRR profiles*

Concerning the TWM combustion model, the main impact of turbulence modeling is on ignition and combustion of fuel during pilot injection. Both graphs

show an increased ignition delay and reduced combustion efficiency. The origin of this behavior can be understood by reminding that the over-prediction of ignition delay from TWM model is induced by inhibition of reaction rate in the fuel-rich regions. This issue is further worsened in the case of RNG k-ε turbulence modeling, because its reduced turbulent diffusivity further increase the fuel vapor concentration in the spray region.

As regards the main injection, the slightly increased ignition delay experienced with TWM combustion model is justified by the reduced combustion efficiency of pilot injection, being ignition of fuel from main injection driven by the hot gases from pilot combustion. Differences in peak apparent heat release rate are related to enhancement of air-fuel mixing. More precisely, the standard k-ε turbulence model experiences lower mixing due to higher dissipation of mean flow momentum into turbulence, which reduces the jet penetration.

About the RIF combustion model, the major differences among the two turbulence models are observed during main combustion, in the region of maximum aHRR. In particular, in addition to an overall increase of mixing controlled combustion when using RNG k-ε turbulence closure, an additional peak of aHRR emerges in correspondence of the one in experimental measurements. At first sight, this would seem in contradiction with the observations made in section 4.1.2, where it was deduced that the first peak of aHRR is caused by flame propagation in the premixed region, which theoretically cannot be reproduced by single-flamelet RIF model. However, a more detailed analysis of the in-cylinder distribution of Eulerian fields shows a problematic when these two turbulence and combustion models are used together. More precisely, looking at figure 4.14 the onset of numerically instability is observed during the main injection, which induces perturbation in mixture fraction distribution and flame structure. After analyzing in depth the evolution of flow fields and mixture fraction distribution, and comparing the results of simulations with both combustion models, it was deduced that instabilities are trigger by having ignition of fuel directly attached to the injector nozzle (as in single-flamelet RIF model), and they are amplified by the lower stability of RNG k-ε with respect to the standard one (as a consequence of the additional non-linear term in the ε equation). To be precise, the following destabilizing mechanism was observed:

1. Before ignition, flow fields and mixture fraction distribution predicted by RIF and TWM combustion models are almost identical, meaning that instabilities are not started yet;

2. With single-flamelet RIF model, propagation of premixed flame cannot be

reproduced, and the whole premixed charge is ignited simultaneously up to the injector nozzle;

3. At ignition, gases experience a severe expansion, which induces perturbations in the mean velocity field. In the region close to the injector nozzle, these perturbations can induce some fuel to be transported in the region above the injector nozzle, where it then ignites;

4. Nonphysical expansion of fuel in the region above the nozzle induces more instabilities in the flow fields, which are propagated downstream;

5. The new instabilities in the velocity field increase the probability that fuel is transported towards the region above injector, and a self-feeding feedback loop is induced.

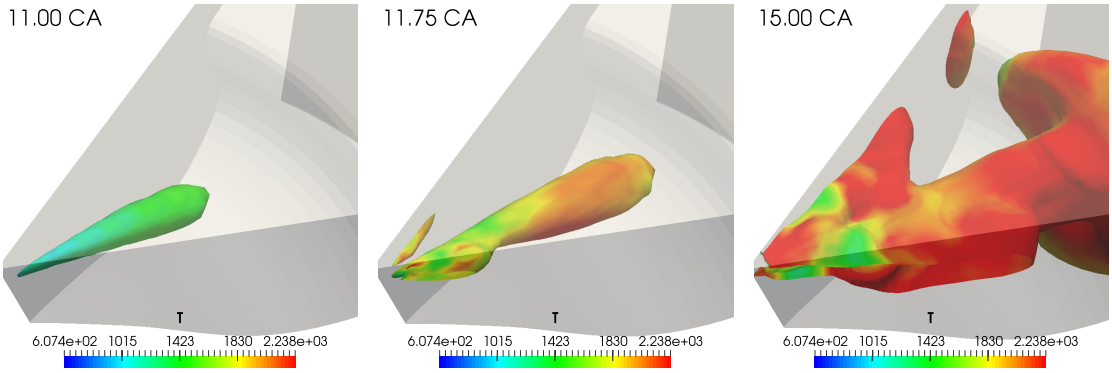

Figure 4.14: *Effect of numerical instability on flame structure when using RIF combustion model with RNG k-ε turbulence model*

The overall effect of these numerical instabilities is increasing the air entrainment and the overall flame surface area, which is probably the cause of that additional peak in aHRR.

According to the proposed assumptions on the origin of numerical instabilities, it is expected that they could be mitigated by adopting multiple flamelet domains to model the main injection, because it would prevent the flame to be attached to the injector nozzle. This aspect will be investigated in section 4.5, dedicated to assessment of the sensitivity of RIF model to the number of flamelet domains.

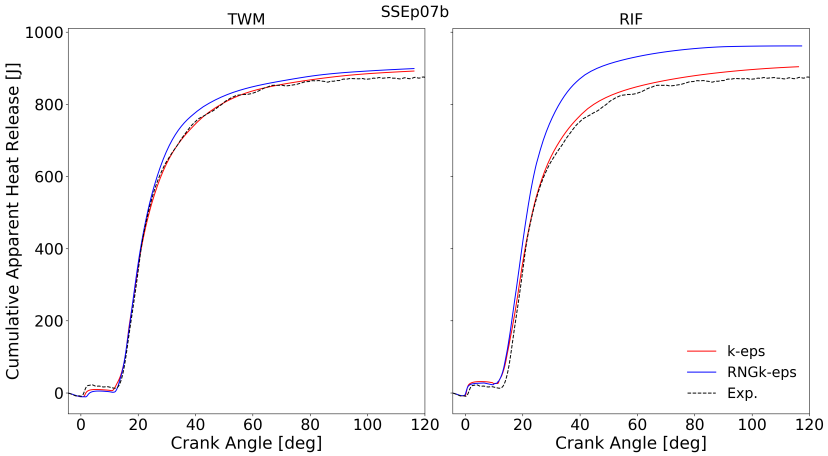

Figure 4.15: *Effect of turbulence modeling: cumulated aHRR*

Finally, the behavior in late stages of combustion should be investigated. Figure 4.15 shows the curves of cumulated aHRR curves with the two turbulence models, compared with the one from experimental measurements. Despite the fact some instability issues were observed during main injection, the dynamics of mixing-controlled and post-injection stages of combustion seem to be, as the shapes of aHRR (Fig. 4.13b) and their cumulative (Fig. 4.15) are similar for the two turbulence models. This happens because after the end of injection these instabilities disappear, and combustion develops only due to mixing.

However, it can be noticed that with RNG k-ε turbulence model the heat released after end of main injection is somewhat enhanced, as the curve of cumulated aHRR better describes the asymptotic behavior of experimental data. This is a consequence of the lower dispersion of mean flow momentum, as it leads to turbulent flow structures of stronger intensity, which last longer during expansion. Therefore, combustion of partially oxidated compounds is promoted by enhanced mixing. To be pointed out that the increase in total aHRR (end of cumulated aHRR curve) is just a consequence of the overall overestimation in the pressure trace, as the heat release rate is proportional to the in-cylinder instantaneous pressure (Eq. A.1), therefore in this case the the curve of cumulated aHRR is to be assessed qualitatively, rather then quantitatively.

4.3 Injection timing

Once the behavior of each turbulence and combustion model in CDC9 operating point is adequately understood, it is possible to investigate how their performance

change with injection conditions. However, to facilitate the interpretation of simulations' results, in the first place it is preferable to briefly analyze the data from experimental measurements, and make some considerations on how the combustion dynamics are affected by injection timing.

Figure 4.16 depicts the curves of apparent heat release rate with the three injection timings, highlighting the time intervals during which pilot and main injections take place. Moreover, to have a better comparison of how the shape of aHRR curve is affected by injection timing, figure 4.17a shows the three profiles time-shifted to have "zero" crank angle at the beginning of their pilot injection. It can be immediately observed from these graphs that combustion dynamics are significantly affected by injection timing, as the shape of aHRR curve during the two injections shows remarkable changes.

First, let us discuss the behavior of pilot combustion. From the comparison of HRR curves given in figure 4.17a, it is seen that ignition of fuel from pilot injection shifts when changing injection timing. The SSEp07b testing condition is characterized by the lowest ignition delay, about 4 CAD after SOI, while the other two have similar ignition timing, about 6 CAD after SOI. Likewise, the peak aHRR during pilot injection is sensibly affected by SOI timing. Pilot combustion in SSEp07b shows the highest peak of aHRR, while SSEp02a testing case has the lowest one, but the longest lasting. These dissimilar behaviors are a consequence of the different thermodynamic conditions inside the cylinder at start of injection. the intermediate timing, pilot injection starts when piston is almost at TDC, thus when in-cylinder pressure and temperature are almost at their maximum. Therefore, fuel experience fast evaporation and short ignition delay. In SSEp17b testing condition, pilot injection starts at -14.4 CAD, and the piston is still going through compression stroke. This means that bulk gas temperature is still quite lower than at TDC, and, consequently, ignition delay is longer. Likewise, the late-injection case experience longer ignition delay due to lower in-cylinder temperature at SOI. However, in this case combustion is further penalized by taking place during expansion stroke, thus when bulk gas temperature is decreasing. This is detrimental for sustaining of combustion reactions, leading to less heat released.

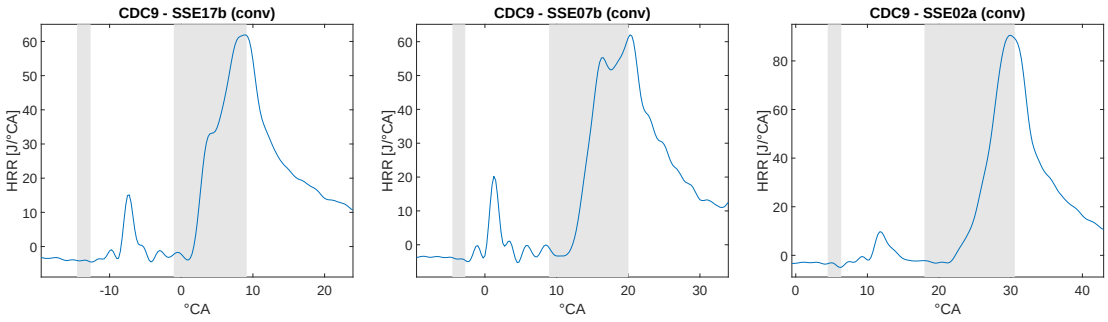

(a) **(b)** **(c)**

Figure 4.16: *Graphs of HRR curves for the three injection timing; the regions highlighted in gray identify the intervals during which pilot and main injections take place.*

Subsequently, the dynamics of main combustion are to be discussed. In this case, ignition timing experiences little sensitivity, with just the late-injection case having slightly longer ignition delay with respect to the other two. This is driven by the fact that during main injection fuel is ignited by the hot gases generated during pilot injection, as it was demonstrated in previous numerical studies on this engine. Therefore, pilot-main injection dwell and intensity of swirling flow are the most relevant parameters affecting ignition delay of main injection, which are the same in the three testing conditions. The slightly increased delay of SSEp02a case can be justified by the smaller temperature increase during pilot injection, the reduced intensity of the swirl vortex due to viscous dissipation, and the reduced reactivity due to lower in-cylinder temperature.

Concerning the shape of aHRR profile in main injection, significant differences are observed with changing of injection timing, denoting a sensible variation of combustion dynamics with delaying of fuel injection. As observed in section 4.1.2, main combustion develops in two stages. After the fuel is ignited by the hot gases coming from pilot combustion, the flame starts propagating in the premixed region on the periphery of the vapor-fuel jet. During this stage, the heat release rate constantly increases due to the increased surface area of the flame. The aHRR curve momentarily stops increasing when the flame is completely attached to the piston walls, and fully diffusive flame is established. In this stage combustion is driven by air-fuel mixing, and the development of HRR curve depends on the intensity of turbulent flow structures generated by jet-wall interaction. After the end of main injection, the HRR begins to decrease, while combustion of the remaining fuel is completed.

Figure 4.17a highlights how the flame-development mechanism is affected by

injection timing. It can be observed that the time span required for development of fully diffusive flame progressively increases with delaying of main-injection timing, with SSEp02a testing case experiencing propagation of premixed combustion until the end of main injection (Fig. 4.16c). Moreover, the overall steepness of the aHRR curve is reduced by postponing injection timing, suggesting that the premixed flame propagates with lower speed. Reduction of bulk gas pressure and temperature are again presumed to be the reason of these outcome. First, reduction of in-cylinder temperature leads to lower fuel reactivity and lower laminar flame speed, thus slowing the propagation of the premixed flame front. Moreover, lower bulk gas pressure leads to diminished penetration of the liquid spray, due to higher drag forces acting on fuel droplets. This as a consequence, when injection timing is closer to TDC, at the onset of main combustion the portion of premixed fuel is smaller, and it takes less time to the flame to propagate to the whole premixed charge.

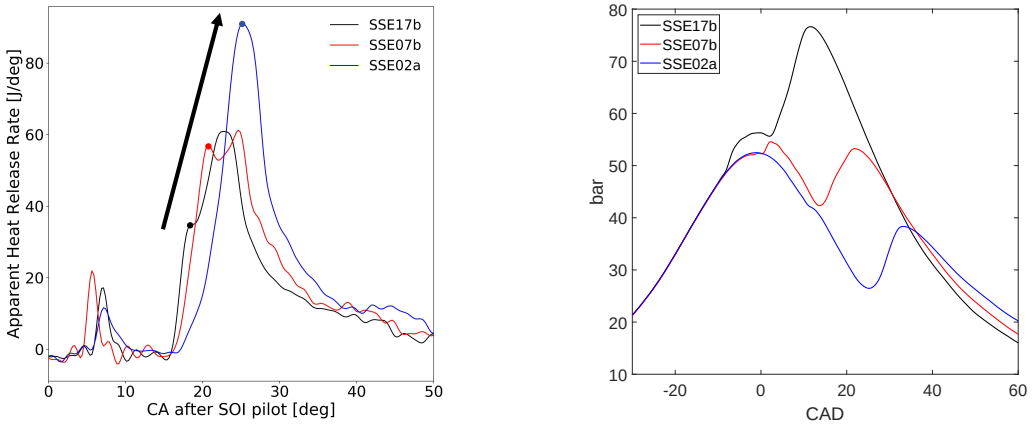

Figure 4.17: *(a): Experimental aHRR profiles phased with respect to the start of pilot injection - (b): Comparison of the pressure traces with the three injection timings*

From this preliminary investigation, it can be foreseen that RIF combustion model will show poor performances in describing combustion development in SSEp02a testing case, for its intrinsic inability in predicting propagation of premixed flames. Therefore, TWM combustion model is expected to show better results in that injection timing.

4.3.1 k-ε turbulence model

Once that the combustion behavior in the three testing conditions is better known, it is possible to investigate, for each of the turbulence and combustion models investigated in this thesis, the sensitivity with respect to injection timing. Here, it has been chosen to assess separately the two turbulence models, and for each one compare the capability of TWM and RIF combustion models to describe the three cases. In this section, the performances with standard k-ε model will be assessed.

Figure 4.18 gives a summary of the performances of the two combustion models in the three injection timings, in terms of the temporal evolution of three global variables: the cylinder pressure (a), the apparent heat release rate (b), and the cumulated aHRR (c).

Looking at the results of RIF combustion model, some considerations can be made. First, for all injections timings, ignition delay of fuel introduced during pilot injection is always under-predicted, with best results achieved in the intermediate timing, and worse in the late-injection case. These results can be justified by the fact that the surrogate fuel used for simulations (n-heptane) was proven to experience shorter ignition delay with respect to the real fuel used during experiments (DPRF58), especially with diminishing of bulk gas temperature. Moreover, the maximum aHRR in pilot combustion is repetitively overestimated by the RIF combustion model. This is probably a consequence of the long ignition delay compared with the duration of pilot injection, as shown in figure 4.16. In fact, this may involve that at onset of combustion a significant portion of the injected fuel is already premixed, and, as already described, RIF model has the tendency to overestimate aHRR during ignition of premixed charge.

Always referring to RIF model, ignition timing during the main injection seems to have discrete agreement with experimental, although it tends to be progressively underestimated with delaying of start of main injection. The possible causes of this behavior are the higher reactivity at low temperature of the surrogate fuel with respect the real one, and the increasing amount of premixed combustion, which is critical for this combustion model. Moreover, for the same reason the RIF model shows really poor performances in the SSEp02a testing condition, which is a further proof of its inadequacy when simulating operating conditions with a significant portion or premixed combustion.

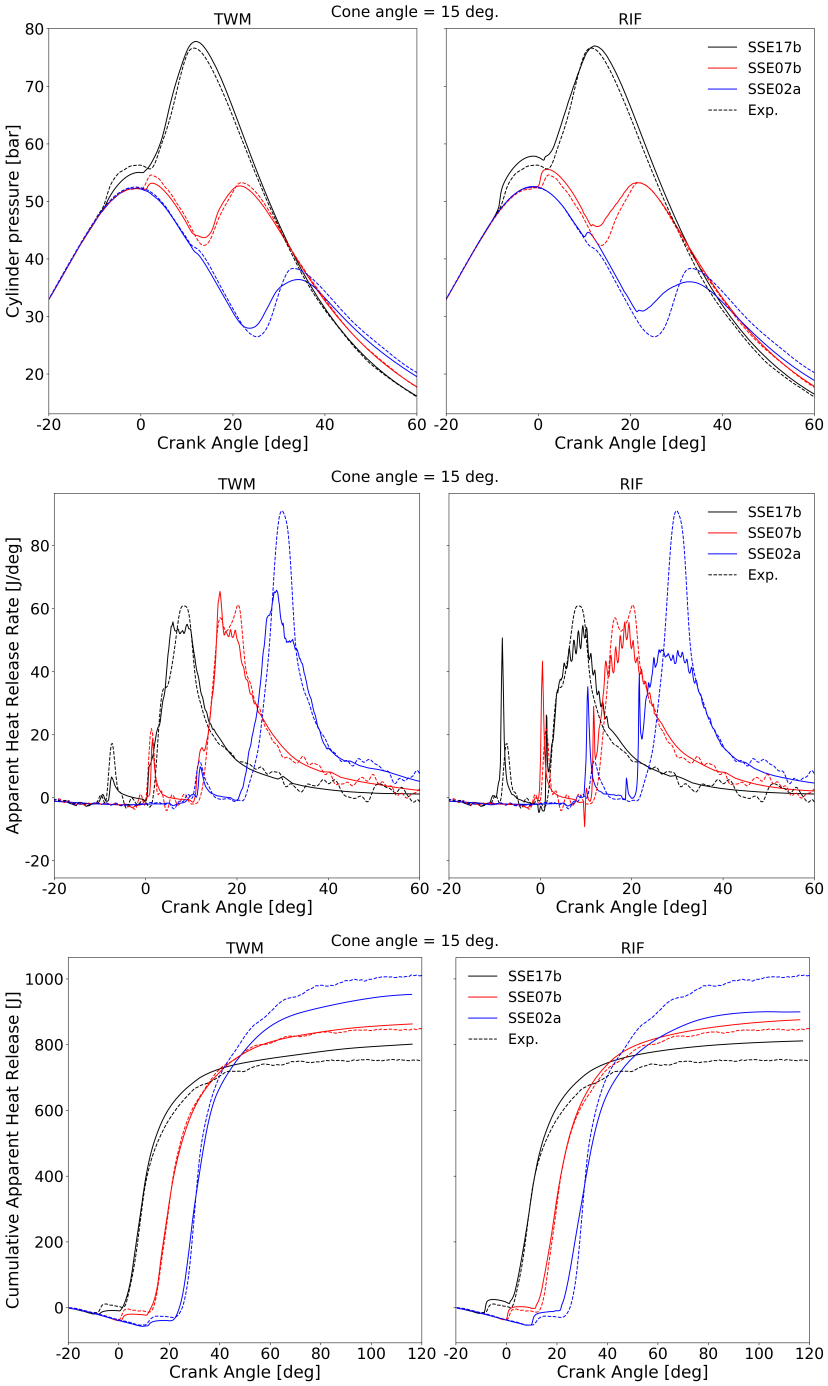

Figure 4.18: *Effect of injection timing on the performances of TWM and RIF combustion models, with the standard k-ε turbulence model - (a): In-cylinder pressure traces - (b): apparent heat release rate - (c): Cumulated aHRR.*

Also for TWM combustion model some considerations can be made. In first place, heat release rate during pilot combustion is underestimated for the SSEp17b testing case, which is again a consequence of the inhibition of chemical kinetics in fuel-rich regions. Regarding combustion of fuel from main injection, ignition delay is slightly underestimated for all injection timings, but the ramps of aHRR are reproduced fairly well. TWM combustion model seems to achieve rather good results in the SSEp02a testing case, even if the peak aHRR is still under-predicted. Figure 4.19 shows the flame structure for this operating case, and the propagation of premixed flame during the ramp of aHRR. It is clearly visible the propagation of the flame, starting from the region where the jet interacts with the hot gases from pilot combustion, and extending to the whole premixed region. The reasons why the experimental maximum aHRR is not reached could be the lower ignition delay, which means that fuel had less time to mix with air, the higher reactivity of n-heptane with respect to DPRF58, or the underestimation of mixing-controlled combustion.

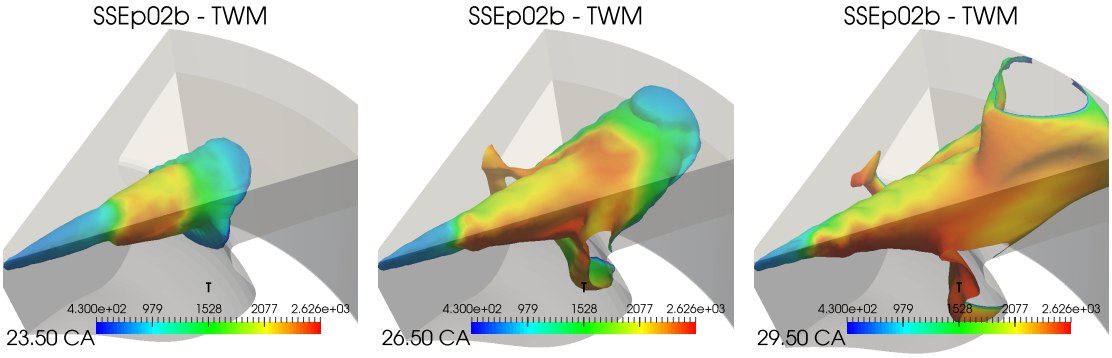

Figure 4.19: *Propagation of premixed flame during main combustion in SSEp02a testing case, predicted by the TWM combustion model. The images show the evolution of the stoichiometric iso-surface, colored by temperature to highlight flame propagation.*

When simulating the first two injection timings, really similar levels of mixing-controlled combustion are experienced by the both combustion models, as it can be seen from the shapes of aHRR curves during main combustion. This behavior could suggest that adoption of k-ε turbulence model leads to reduced sensitivity to jet-wall interaction, which is the main phenomenon affected by injection timing. This could be justified by the highly dissipative nature of k-ε turbulence model, which predicted quite high dissipation of mean-flow momentum into turbulence, and a widely spread distribution of turbulent kinetic energy. This means that when the jet reaches the bowl rim, it has seen a sensible reduction of momentum and it is fairly dispersed from the axis of the spray. Thus reducing the sensitivity

of the jet-wall interaction phenomenon with respect to injection timing.

Finally, the post-injection phase of combustion seems to be predicted to an acceptable degree by both combustion models in all operating conditions, as the shape of aHRR and cumulated aHRR curves match fairly well those from experimental measurements, even though a different final value of cumulated aHRR is obtained.

4.3.2 RNG k-ε turbulence model

Figure 4.20 summarized the performances of the RNG k-ε model in combination with the two combustion models in the three injection timings, in terms of cylinder pressure (a), apparent heat release rate (b), and cumulated aHRR (c).

In first place, let us discuss the results of the RIF combustion model. Combustion of pilot injection shows the same peculiarities observed for the k-ε turbulence model, i.e., progressively under-prediction of ignition delay with diminishing of bulk gas temperature at start of injection, and persistent overestimation of peak aHRR, although less severe than with the other turbulence model. The lower peak value predicted RNG k-ε model is probably induced by its lower turbulent diffusivity, which involves that a smaller amount of premixed charge has formed at the onset of pilot combustion.

As already seen with the standard k-ε model, ignition delay of fuel injected during main injection is progressively under-estimated when SOI is delayed. Likewise hypothesis before, the possible origins of this issue are the higher reactivity at low temperature of the surrogate fuel with respect the real one, and the increasing amount of premixed combustion. Moreover, as predictable, also in this case the RIF combustion moded achieves rather poor performances describing main combustion in the SSEp02a testing scenario. On the other hand, when simulating the the SSEp17b testing case with this turbulence model sensible differences in aHRR are observed during main combustion. Figure 4.21 depicts the the flame development during the main combustion for this injection timing. When compared with the results of the intermediate-injection case (Fig. 4.14), it is evident that in this testing case the numerical model is subjected to sensibly reduced numerical instabilities. To understand the reason of the higher stability of the early-injection case, figure 4.22 gives a comparison of the in-cylinder conditions at ignition for the two injection timings. In particular, a lower level of premixed combustion is observed for the SSEp17b injection timing, which was inferred to be one of the triggering factors for the observed numerical instabilities.

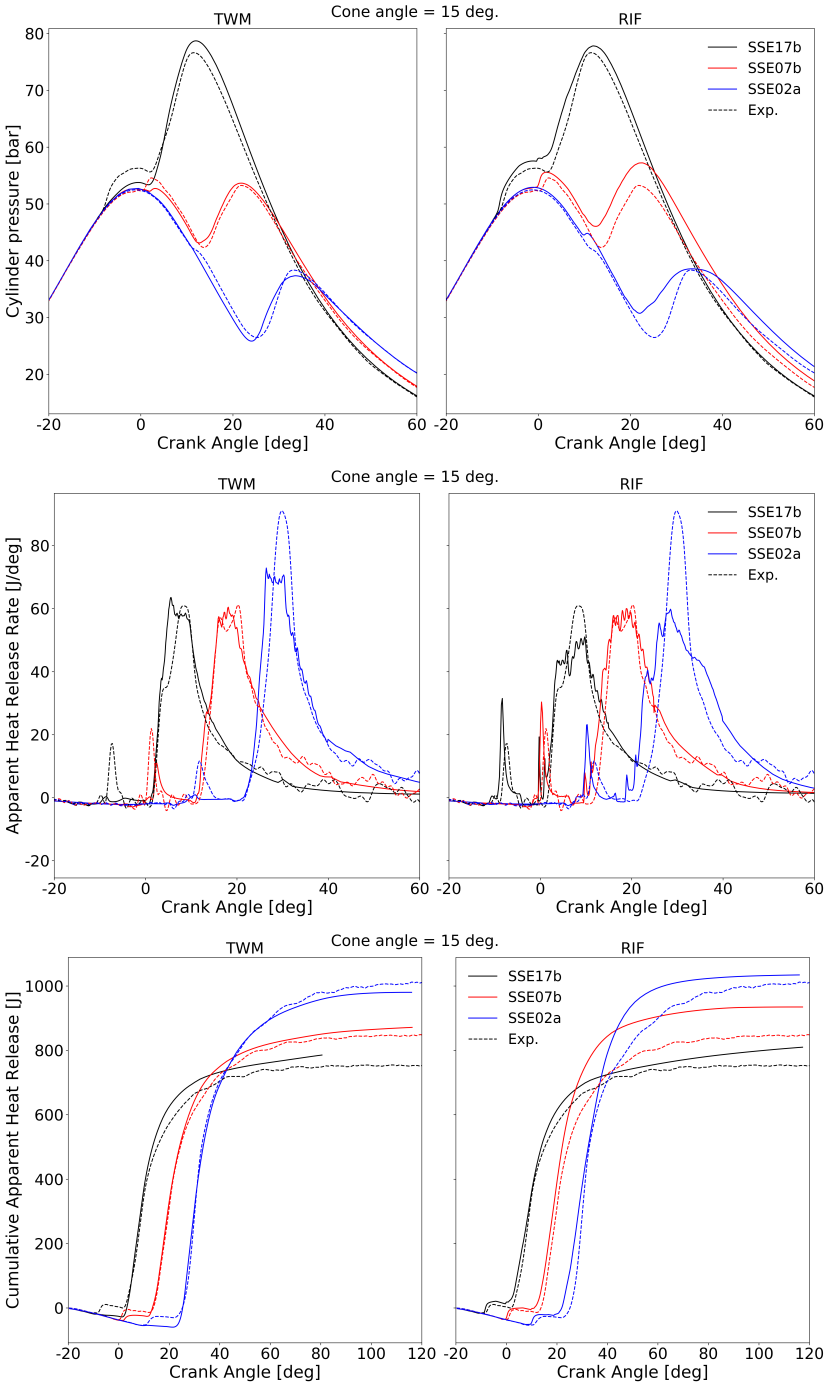

Figure 4.20: *Effect of injection timing on the performances of TWM and RIF combustion models, with the RNG k-ε turbulence model - (a): In-cylinder pressure traces - (b): apparent heat release rate - (c): Cumulated aHRR.*

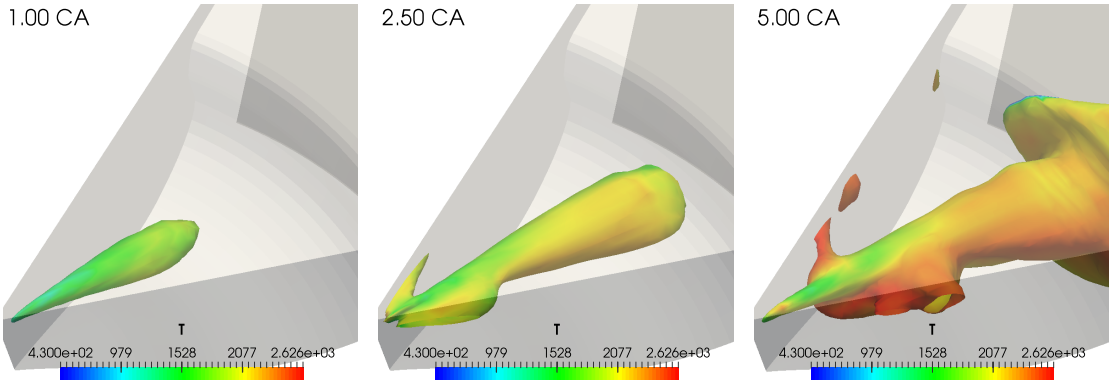

Figure 4.21: *Development of numerical instabilities due to combined use of RIF and RNG k-ε models, in the SSEp02a testing case. The images show the evolution of the stoichiometric iso-surface, colored by temperature, in the instants following the ignition of main injection.*

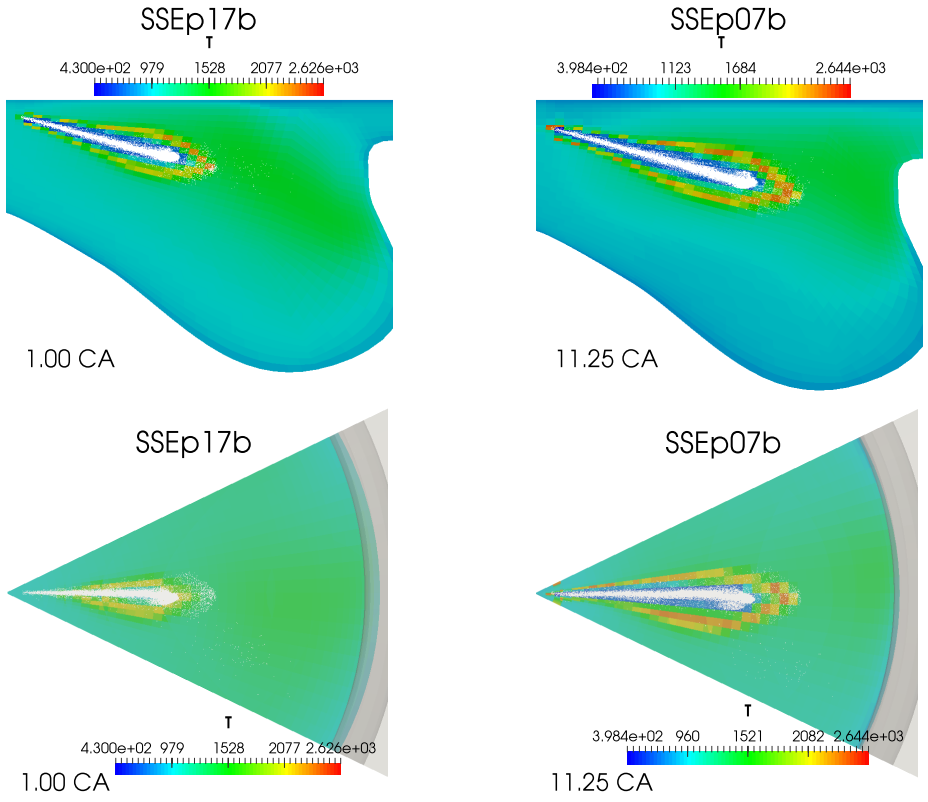

Figure 4.22: *Comparison of spray penetration at ignition of main injection, between SSEp17b and SSEp07b testing cases. The images show the Lagrangian spray and temperature distribution predicted by RIF model at ignition of fuel from the main injection event.*

Thanks to the lower intensity of unstable phenomena, the results in this operating conditions are thought to be quantitatively more reliable. Another peculiarity of the aHRR curve for the SSEp17b case is its temporary drop in the middle of the main combustion. Looking at the evolution of the diffusive flame, depicted in figure 4.23, it can be noticed that adjacent jets start to interact in that time interval. Therefore, it is likely that the reduction of aHRR is associated with the sudden reduction in surface area of the diffusive flame.

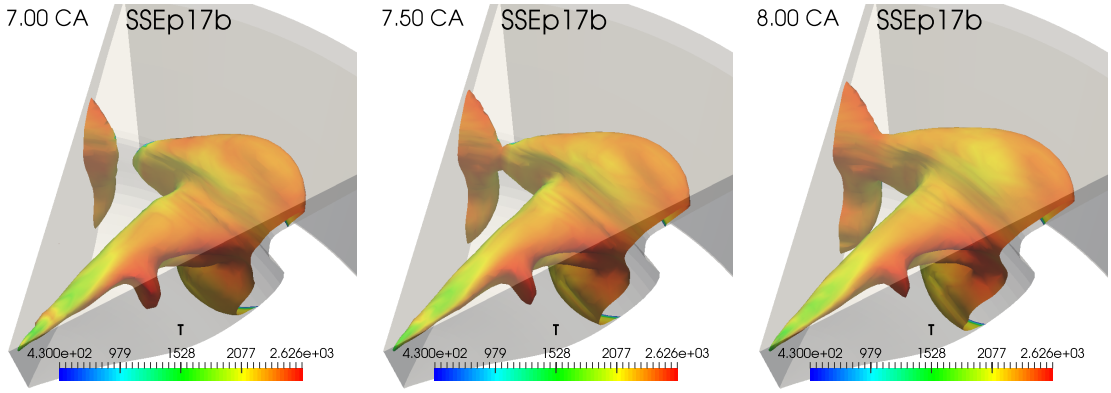

Figure 4.23: *Jet-to-jet interaction during main combustion for SSEp17b testing case. The images show the evolution of stoichiometric iso-surface, colored by local charge temperature.*

For what concerns the TWM combustion model, the issue regarding ignition of fuel from pilot injection is further worsened in the other two cases, to the point of having charge misfire. This could be a consequence of the lower bulk-gas temperature at start of pilot injection, which leads to a reduction of the reaction rate. Due to almost absent temperature increase during pilot combustion, in this case the TWM model predicts delayed ignition with respect to the RIF combustion model. However, even though pilot injection did not experience complete combustion, ignition of fuel introduced during main injection takes place in the same region (Fig. 4.24), thanks to the presence of partially oxidized compounds that increase local mixture reactivity. Therefore, at least partially, the overall combustion dynamics of main injection are preserved.

Also with the RNG k-ε turbulence model, the TWM model shows rather satisfactory results when used to simulate the late-injection scenario. The increased peak of heat release showed in figure 4.20b is presumed to be a consequence of miss-fire during pilot injection, which leads to a slower development of the flame. Moreover, really good agreement with experimental results is observed in the re-

gion after the end of main injection, as shown by the cumulated aHRR curves in figure 4.20c.

Generally speaking, the RNG combustion model seems to show higher sensitivity to the injection timing, especially in combination with the RIF combustion model. This could be induced by the lower dissipation of spray momentum, thanks to the lower turbulence intensity predicted by this turbulence model, which could make more important the jet-wall interaction in determining the mixing intensity. Miss-fire of fuel from pilot injection could make this effect less evident with the TWM combustion model, because it increases the degree of premixed combustion during main injection.

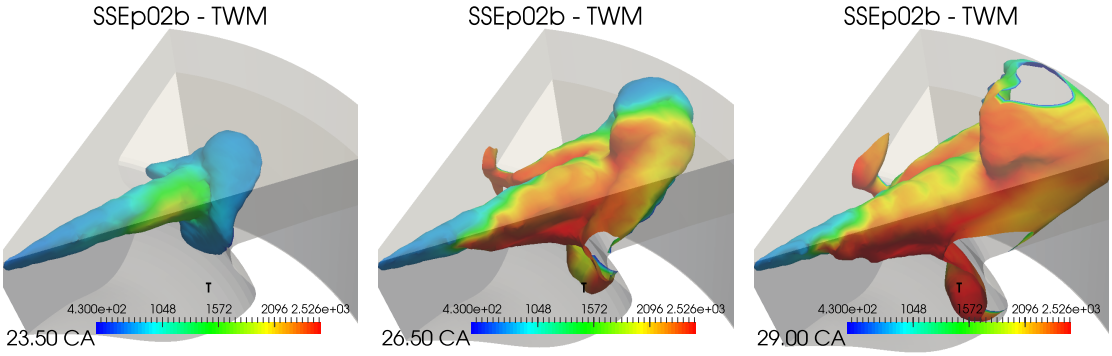

Figure 4.24: *Ignition and propagation of premixed flame during main combustion in SSEp02a testing case, predicted by the TWM combustion model. The images show the evolution of the stoichiometric iso-surface, colored by temperature to highlight flame propagation. It can be seen that ignition takes place in the same location, even though pilot injection does not ignite.*

4.4 Sensitivity to spray cone angle

Once that the behavior of the turbulence and combustion models was better understood, along with their performances in multiple injection conditions, it was chosen to investigate their sensitivity to some relevant parameters that are expected to affect the dynamics of the diesel combustion strategy studied in this work.

As mentioned in section 3.2.3, even though in the literature many models have been proposed to estimate the spray spreading angle at the outlet of the injector orifice [18], in this thesis it was decided not to use any of these correlation in the spray model. This choice was driven mainly by the following reasons:

- Usually these models are based on empirical correlations, and do not consider the effect of the specific shape of injector nozzle, which was shown to have a sensible impact on the spray structure [16, 52];
- In this study the thermophysical properties of conventional Diesel fuel were used for the liquid phase, according to the model proposed by Sazhin [50], which have some dissimilarities from those of DPRF58. Therefore, correlations are not expected to reproduce the real spray opening angle, having discrete sensitivity to the fuel density;
- The predicted spray cone angle can sensibly change depending on the specific correlation used.

Thus, a constant spray cone angle was used, which is an independent variable of the problem, so that its impact on the overall combustion dynamics can be separately assessed. This was done by reducing the spray spreading angle from 15° to 10°, and simulating the three injection strategies previously described. In this section a detailed investigation on the sensitivity of each turbulence and combustion model to this parameter is reported. Moreover, this can be used as a measure of the capability of each model to appreciate changes in spray structure and injector design.

Before moving on the discussion of the results, it is worth briefly describing how changing of the spray spreading angle is expected to affect the development of air-fuel mixture and the overall combustion process, assuming that all the other injection parameters and the bulk gas conditions are fixed.

First of all, if liquid parcels are concentrated in a narrower region close to the spray axis, the momentum of liquid phase is less dispersed and a smaller amount of gas phase interacts with the liquid droplets. Thus the gas interacting with the

spray undergoes a higher acceleration, while lower reduction in momentum is experienced by the liquid droplets. Hence, the reduced radial dispersion of momentum and lower drag forces acting on the liquid phase are expected to lead to an overall enhancement of the liquid and vapor fuel penetration. Moreover, having a more collimated spray and a lower relative velocity between liquid and gas phases, it is expected that the amount of air entrained in the spray is reduced. Therefore, there could be a lower radial dispersion of mixture fraction, with increased equivalence ratio in the core of the spray, and reduced spray evaporation.

Hence, a reduction in the spray spreading angle is expected to lead to a lower degree of premixed combustion and an increment of the heat released during the mixing-controlled stage of combustion.

Similarly to past section, the discussion is developed separately for the two turbulence models, studying for each of them the sensitivity of the TWM and RIF combustion models.

4.4.1 k-ε turbulence model

First, the sensitivity is investigated with the conventional k-ε turbulence model. Figures 4.25, 4.26 and 4.27 report the performances of the TWM and RIF combustion models for the three injection strategies - SSEp17b, SSEp07b and SSEp02a respectively - with a spay spreading angle of 10° and 15°.

By looking at the behavior of both combustion models in the three testing conditions, it appears that the spray spreading angle plays a really marginal role in the combustion process, when turbulence is modeled with the conventional k-ε closure. To better understand the reason of these results, it is required a deeper analysis on the underlying processes that determine the combustion dynamics.

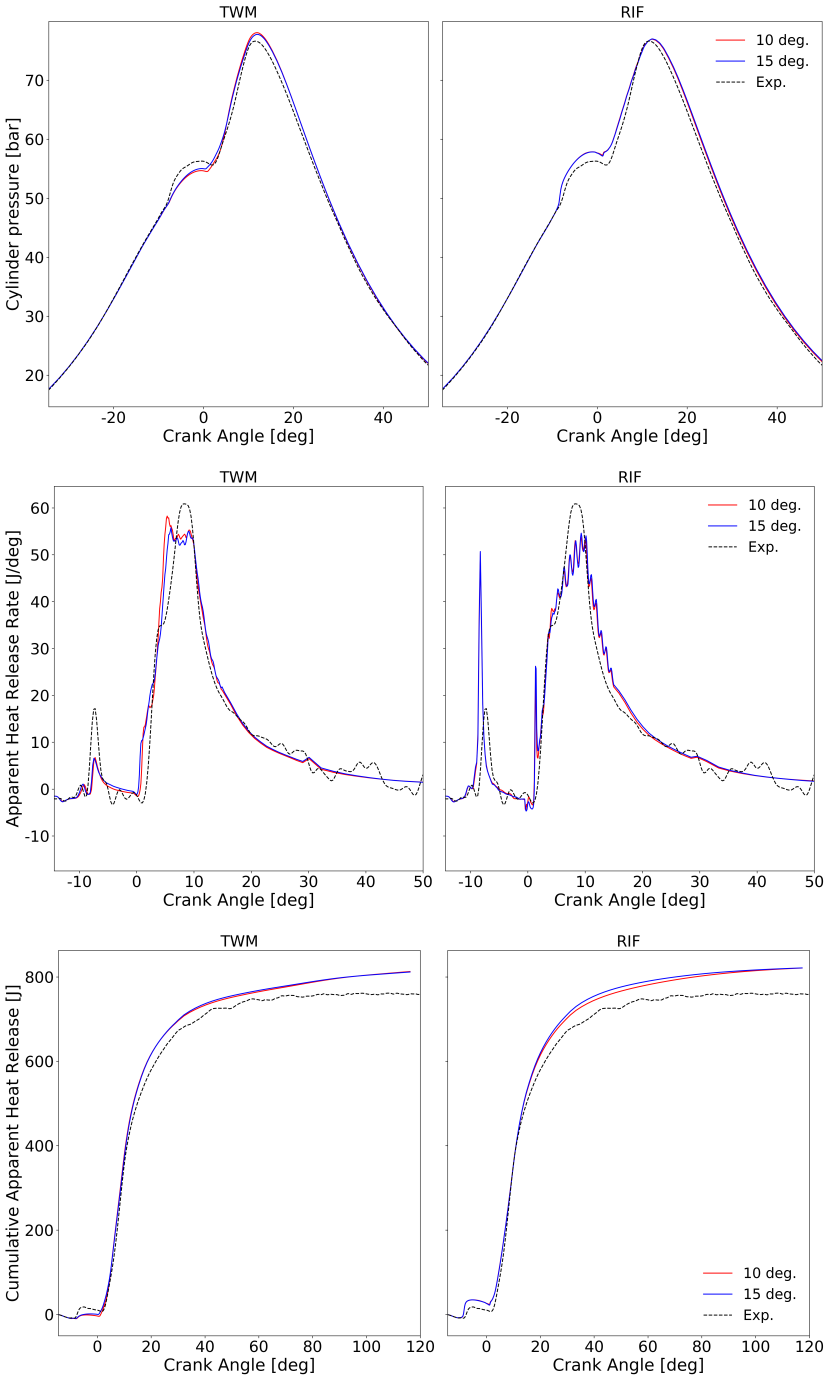

Figure 4.25: *Sensitivity to spray cone angle of TWM and RIF combustion models, with the standard k-ε turbulence model, in the SSEp17b testing case - (a): In-cylinder pressure traces - (b): apparent heat release rate - (c): Cumulated aHRR.*

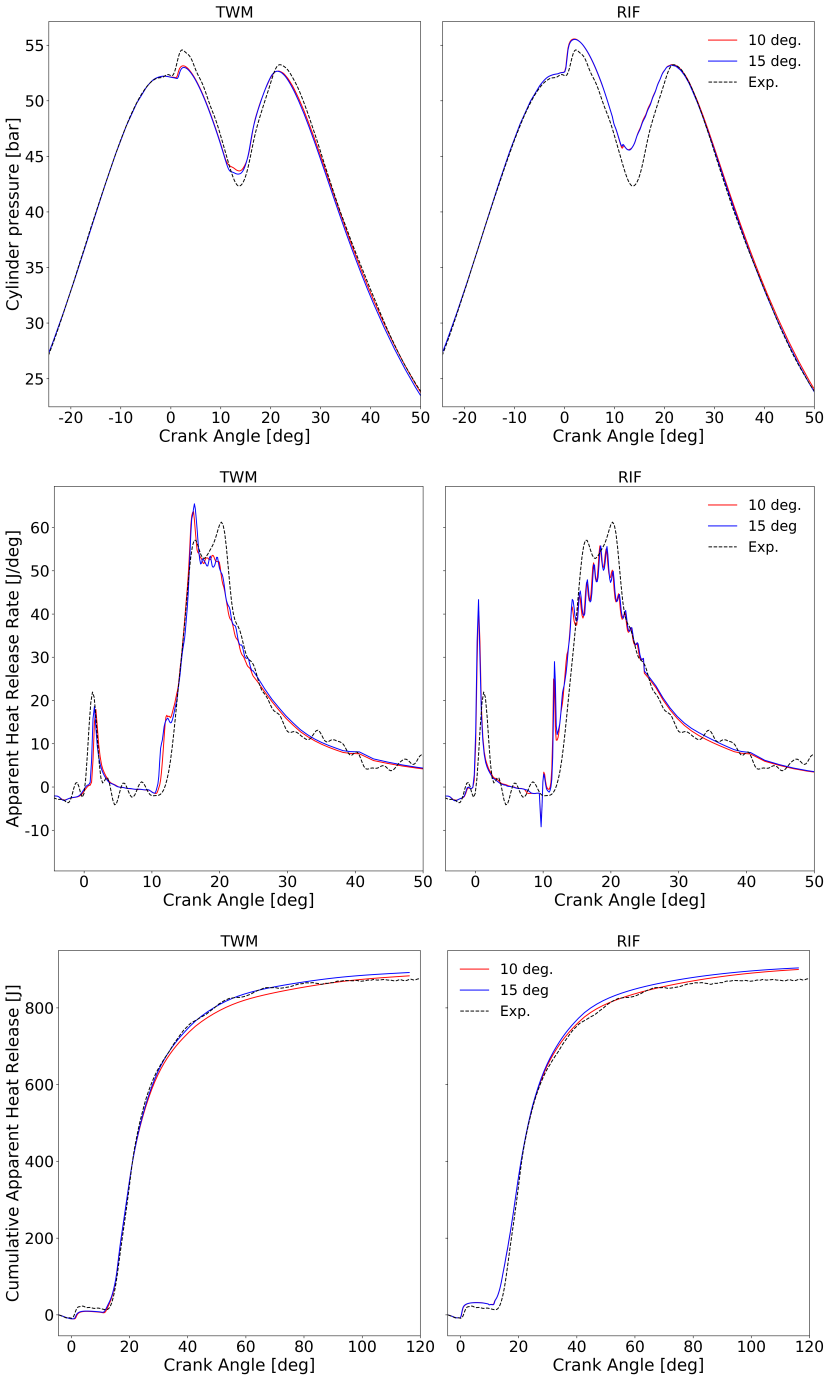

Figure 4.26: *Sensitivity to spray cone angle of TWM and RIF combustion models, with the standard k-ε turbulence model, in the SSEp07b testing case - (a): In-cylinder pressure traces - (b): apparent heat release rate - (c): Cumulated aHRR.*

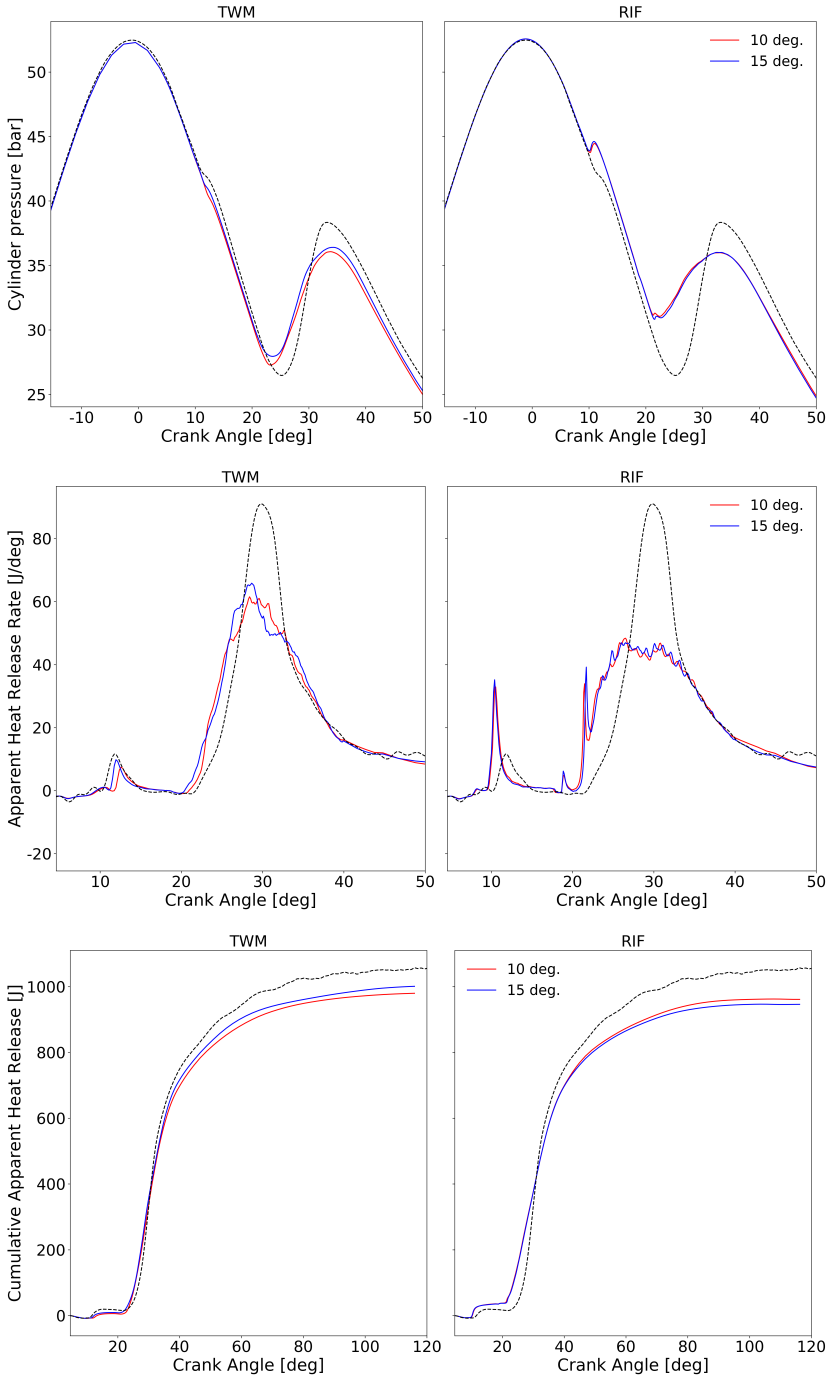

Figure 4.27: *Sensitivity to spray cone angle of TWM and RIF combustion models, with the standard k-ε turbulence model, in the SSEp02a testing case - (a): In-cylinder pressure traces - (b): apparent heat release rate - (c): Cumulated aHRR.*

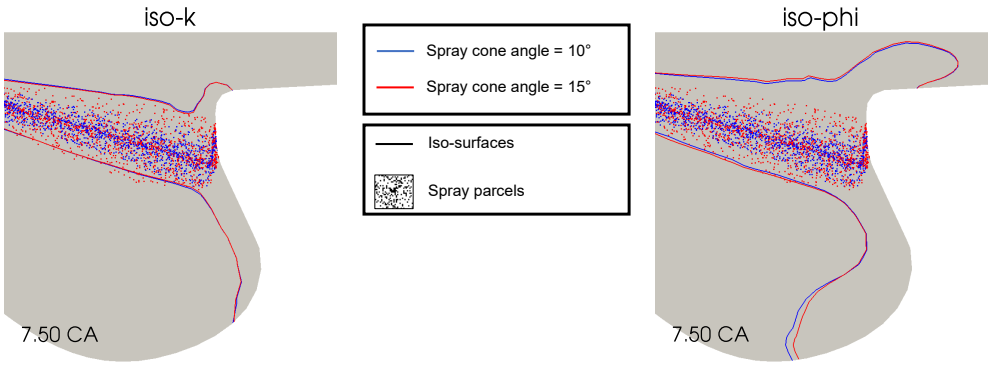

(a) **(b)**

Figure 4.28: *Effect of spray cone angle on turbulence, spray structure and mixing, with standard k-ε turbulence model, RIF combustion model, in the SSEp17p injection strategy. - (a): Iso-surfaces where TKE is a quarter of its maximum in that given instant - (b): Iso-surfaces where mixture is at stoichiometric conditions ($\phi = 1$).*

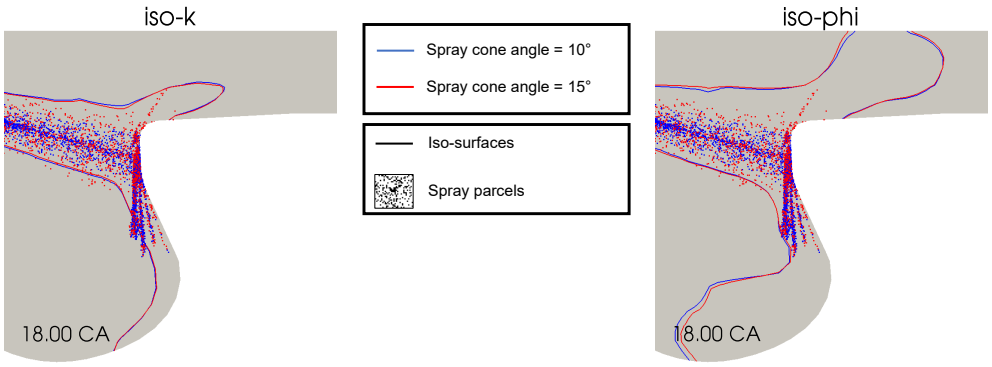

(a) **(b)**

Figure 4.29: *Effect of spray cone angle on turbulence, spray structure and mixing, with standard k-ε turbulence model, RIF combustion model, in the SSEp07p injection strategy. - (a): Iso-surfaces where TKE is a quarter of its maximum in that given instant - (b): Iso-surfaces where mixture is at stoichiometric conditions ($\phi = 1$).*

To this end, the results were post-processed to investigate the development of Lagrangian spray, turbulence distribution and air-fuel mixing with the two spreading angles investigated. For the simulations with the RIF combustion model, fig-

ures 4.28 and 4.29 show a comparison of these quantities, for the SSEp17b and SSEp07b injection timings respectively, in the following manner:

- To have a measure of the dispersion of spray momentum due to turbulence, the distribution of turbulent kinetic energy is visualized through the iso-surfaces delimiting the region where TKE is more than a quarter of the instantaneous maximum value, reported in figures 4.28a and 4.29a;
- The effect of spray spreading angle on air-fuel mixing is visualized through the iso-surfaces where the mixture is at stoichiometric conditions ($\phi = 1$), shown in figures 4.28b and 4.29b;
- For the sake of comparison, the distributions of the Lagrangian spray parcels with the two spreading angles are reported in every image.

As expected, it is clearly visible that the spray with an imposed spreading angle of 10°, colored in blue, is less dispersed radially. However, it seems that both spray angles lead to the same distribution of turbulent kinetic energy. This is in agreement with the past studies in the literature and the results of section 4.2, where that k-ε turbulence model showed to predict significant dispersion of TKE and poor description of shear flows. Hence, even though the liquid spray is confined closer to the spray axis, the mean-flow momentum experiences a radial diffusion due to turbulence similar to the one with the larger spreading angle. For these reasons, the radial spreading of mixture fraction due to turbulent diffusion is almost unchanged, and a really small increase in fuel vapor penetration is observed.

For the sake of completeness, it should be noted that slight changes are observed in the curve of apparent heat release rate with the TWM combustion model, in the late-injection case.

The changes in ignition delay and peak aHRR during pilot combustion are still associated with the inhibition of reaction rate in the fuel-rich regions. This condition is worsened with reduction of the spray spreading angle, due to the lower fuel diffusion and increased equivalence ratio in the spray region. It is presumed that this injection timing is the only one showing noticeable sensitivity because the in-cylinder temperature is significantly lower to the others, meaning that the thermodynamic conditions are already critical for fuel ignition.

Concerning main injection, the slightly increased ignition delay is assumed to be a consequence of the lower combustion efficiency of pilot injection, while the different shape of aHRR curve is induced by changes in mixture fraction diffusion and mixing intensity. However, these differences are negligible, as the overall dynamics of combustion phenomena are preserved.

4.4.2 RNG k-ε turbulence model

The effect of the RNG k-ε turbulence model is then investigated. The performances of the TWM and RIF combustion models are reported in figures 4.25, 4.26 and 4.27, for the SSEp17b, SSEp07b and SSEp02a injection strategies respectively, for the two spray spreading angles assessed. In this case, the results of the simulations show noticeable sensitivity with respect to the spray cone angle imposed at the outlet of injector nozzle.

For what concerns the RIF combustion model, it can be observed that the results are sensibly improved by reducing the spreading angle, especially for the first two injection timings, both in terms of pressure trace and apparent heat release rate. For both SSEp17b and SSEp07b testing cases, the shape of aHRR curve during main combustion is significantly changed:

- The first peak, which was inferred to be a consequence of the numerical instabilities, is partially smoothed out. This behavior is justified by the fact that a more collimated spray is expected to reduce the intensity of premixed combustion, which was hypothesized to be one of the driving factor for the numerical instabilities;
- As expected, with a reduced spreading angle the peak of mixing-controlled combustion is sensibly increased, showing also good agreement with the experimental measurements.

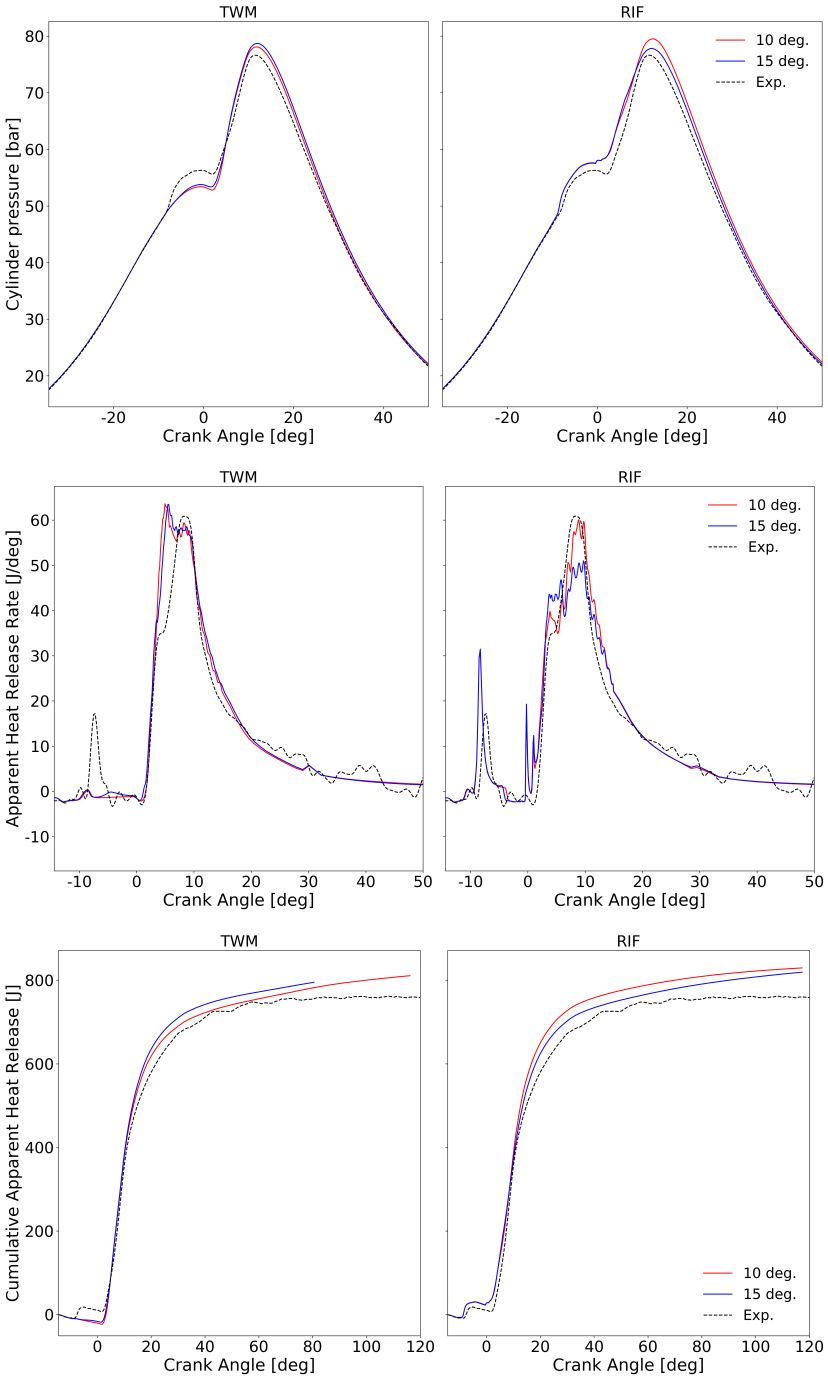

Figure 4.30: *Sensitivity to spray cone angle of TWM and RIF combustion models, with the RNG k-ε turbulence model, in the SSEp17b testing case - (a): In-cylinder pressure traces - (b): apparent heat release rate - (c): Cumulated aHRR.*

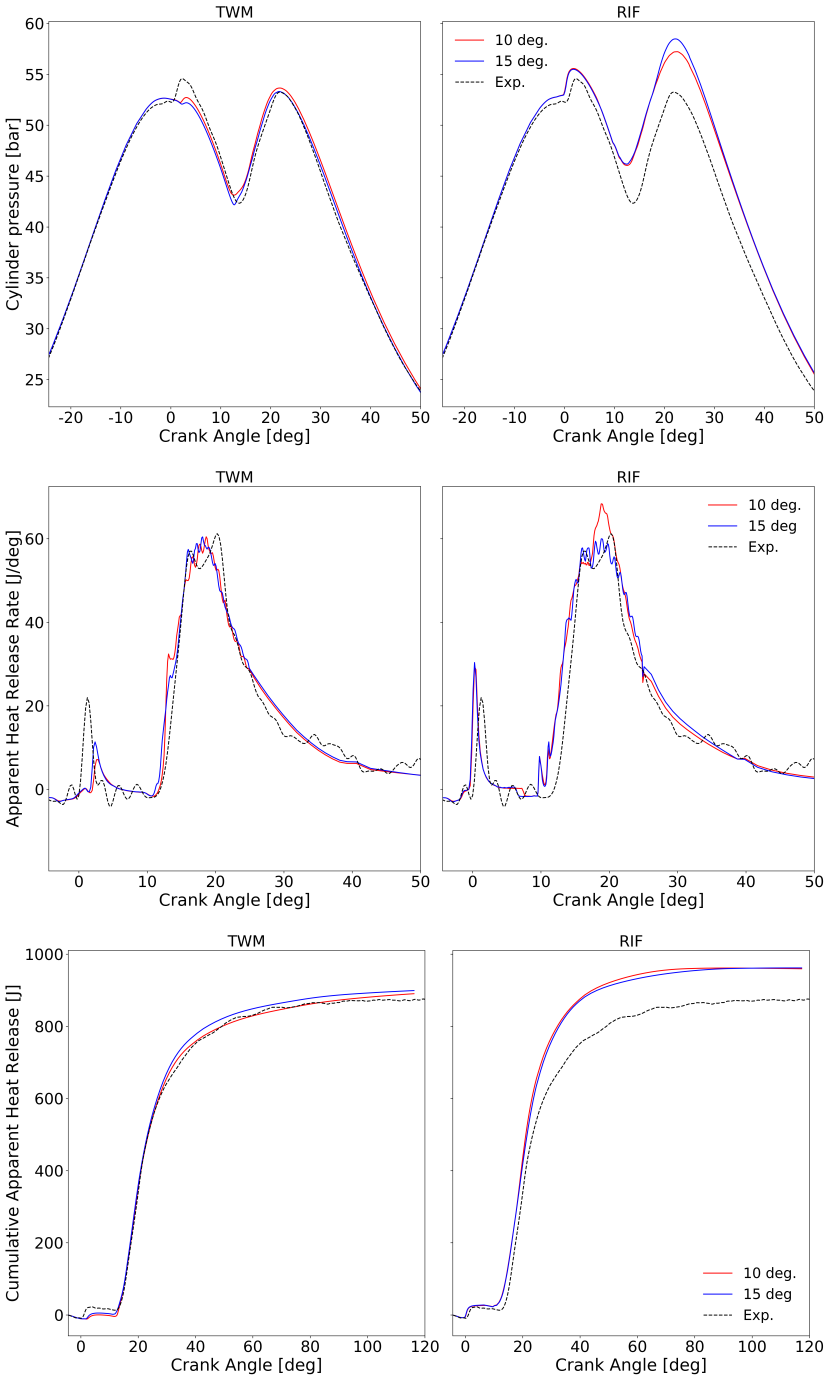

Figure 4.31: *Sensitivity to spray cone angle of TWM and RIF combustion models, with the RNG k-ε turbulence model, in the SSEp07b testing case - (a): In-cylinder pressure traces - (b): apparent heat release rate - (c): Cumulated aHRR.*

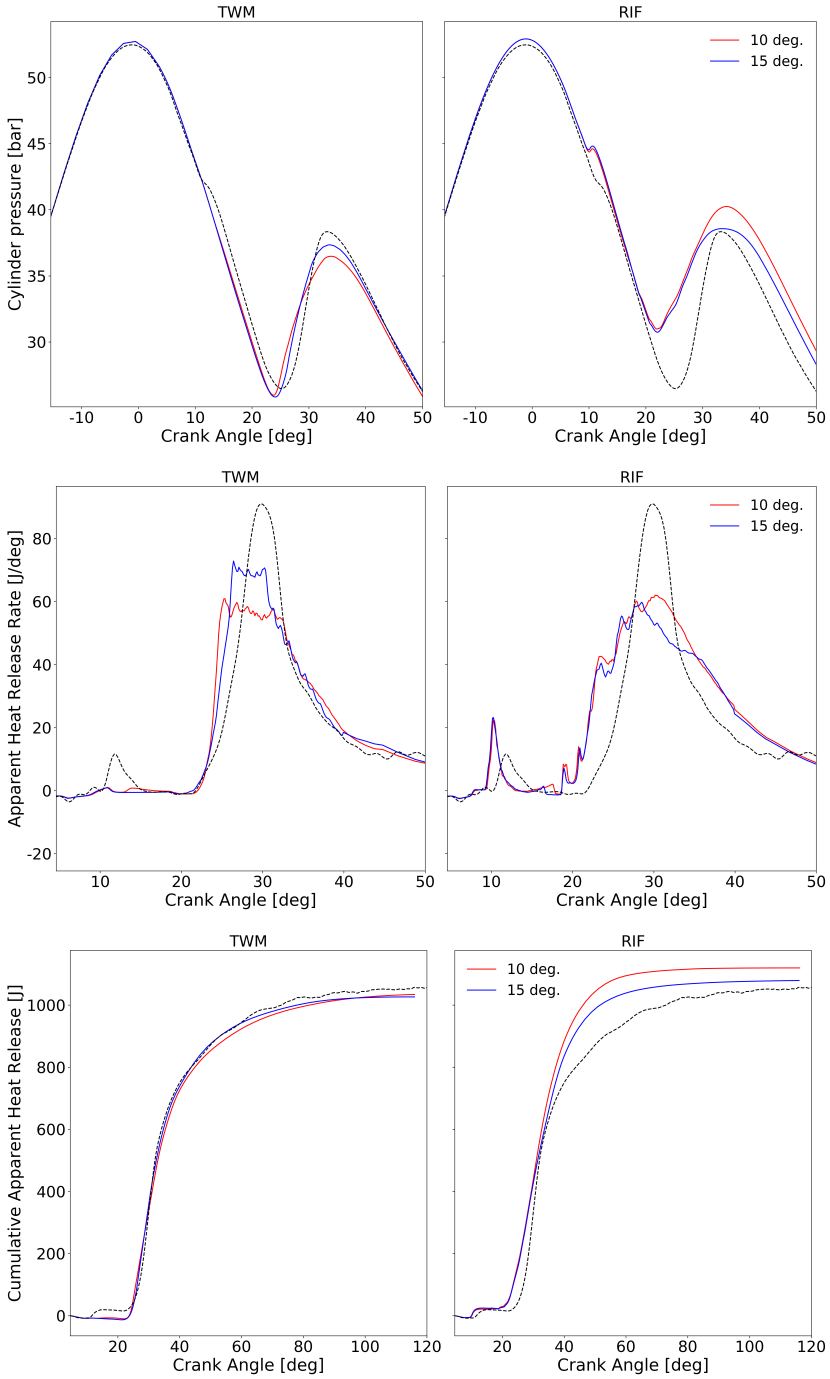

Figure 4.32: *Sensitivity to spray cone angle of TWM and RIF combustion models, with the RNG k-ε turbulence model, in the SSEp02a testing case - (a): In-cylinder pressure traces - (b): apparent heat release rate - (c): Cumulated aHRR.*

Like it was done for the other turbulence model, this behavior can be better understood by post-processing the results of the simulations in terms of Lagrangian spray structure, turbulence distribution and air-fuel mixing, as reported in figures 4.33 and 4.34.

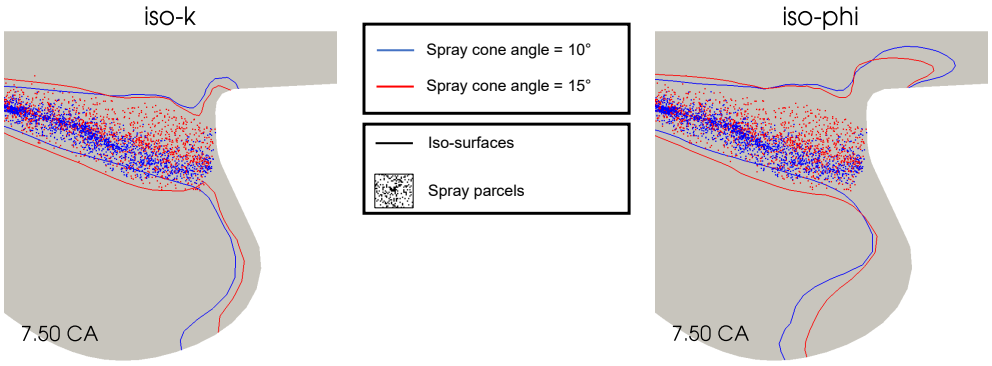

(a) **(b)**

Figure 4.33: *Effect of spray cone angle on turbulence, spray structure and mixing, with RNG k-ε turbulence model, RIF combustion model, in the SSEp17p injection strategy. - (a): Iso-surfaces where TKE is a quarter of its maximum in that given instant - (b): Iso-surfaces where mixture is at stoichiometric conditions ($\phi = 1$).*

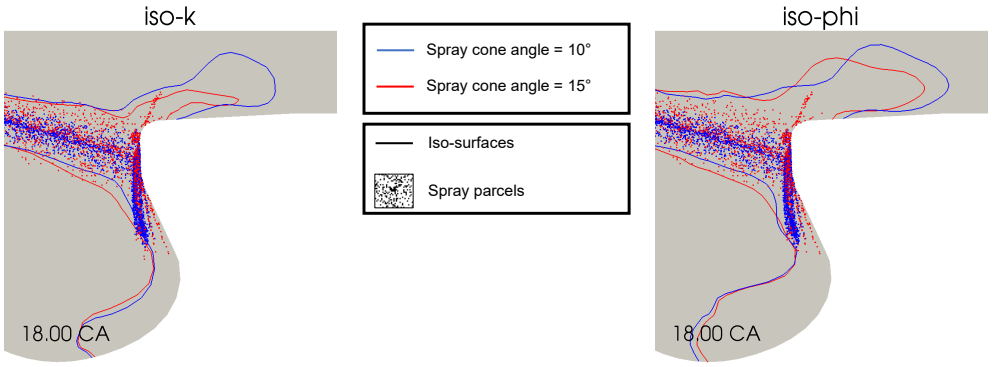

(a) **(b)**

Figure 4.34: *Effect of spray cone angle on turbulence, spray structure and mixing, with standard k-ε turbulence model, RIF combustion model, in the SSEp07p injection strategy. - (a): Iso-surfaces where TKE is a quarter of its maximum in that given instant - (b): Iso-surfaces where mixture is at stoichiometric conditions ($\phi = 1$).*

As expected, with an imposed spray angle of 10° the spray parcels are less dispersed, likewise for the previous turbulence model. However, with the RNG k-ε turbulence model, also turbulent kinetic energy distributions show sensible changes as well. In particular, TKE is less spread from the spray axis and experiences increased penetration, either inside the bowl or towards the squish region, depending on the injection timing. Hence, the fuel vapor is less spread out from the jet boundary due to turbulence diffusion, and it experiences higher penetration and stronger mixing. Therefore, this turbulence model shows to be capable to predict variations in jet penetration and turbulent dissipation of mean flow momentum, as a consequence of changes in spray structure. These results are a further evidence of the good capability of RNG k-ε turbulence model to describe shear flows.

Moreover, some improvements are observed also in the post-injection stage of combustion, as shown by the curves of cumulated aHRR. This behavior is thought to be a consequence of the lower dissipation of mean-flow momentum. In fact, this involves that the turbulent flow structures generated during main injection are of stronger intensity and require more time to be dissipated by viscous forces. Thus, combustion of the remaining products of partial oxidation is promoted by enhanced mixing during expansion stroke.

For the late-injection testing condition, slight improvement are observed in the pressure trace and aHRR curve, shown in figures 4.32a and 4.32b respectively, but RIF combustion model still shows overall poor performances with such delayed injection timing.

Regarding the results of the simulations with the TWM combustion model, smaller sensitivity is observed with respect to the spray spreading angle imposed at the injector orifice. For every testing condition, the issues found in ignition and combustion of fuel during pilot injection are even worsened, which is coherent with the results with the other turbulence model. As previously explained, this is driven by the reduction in turbulent diffusion and air entrainment, thus increasing the equivalence ratio in the spray region.

For what concerns main combustion, only the SSEp02a injection timing shows discrete sensitivity to spray spreading angle. In this case, a faster rise in aHRR curve is experienced with a 10° spreading angle, along with advanced establishment of mixing-controlled combustion with lower heat release rate. To understand the origin of these differences, the flame structure during mixing-controlled combustion is shown in figure 4.35, for both values of spray spreading angle investigated. Therefore, the reduction in aHRR associated to a diminished spray spreading angle can be justified by the following phenomena:

- The flame lift-off length is sensibly increased, which is probably due to the reduction of air entrainment and lower dispersion of mean-flow momentum;
- The air-fuel mixture is less spread out from the spray axis, which reduces the overall flame surface area, where most of heat is released during combustion;
- The reduced dispersion of momentum does not show visible increase of mixing intensity, as almost all of the fuel is directed towards the squish region, where it hits nearly perpendicularly the cylinder walls.

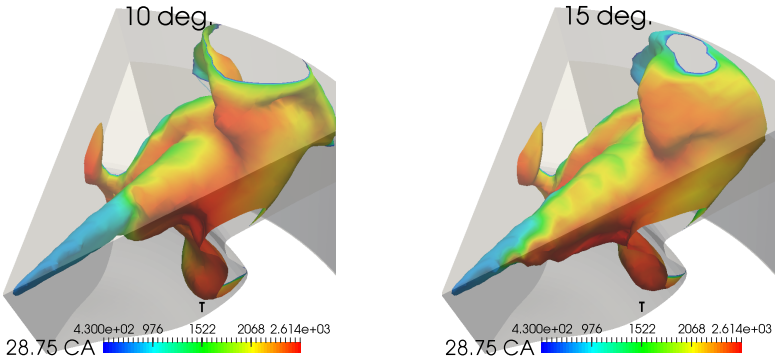

(a) **(b)**

Figure 4.35: *Effect of spray spreading angle on flame structure when simulating SSEp02a injection timing with the TWM combustion model. (a) and (b) show the stoichiometric iso-surfaces colored according to the temperature fields, for an imposed spreading angle of 10° and 15° respectively.*

For the other two injection timings, the analysis of the in-cylinder distributions of the main Eulerian fields did not show sensible variations between the simulations with the two values of spreading angles investigated. Although it is presumed that this result could be induced by neglecting of turbulence-chemistry interaction in the TWM combustion model, no significant reason for these similarities could be deduced from these investigations. Therefore, further investigations are to be performed in future works to fully understand the origin of these results.

4.5 RIF: sensitivity to number of flamelets

It is well known in the literature that the capability of the RIF combustion model to correctly describe the combustion process, and the flame structure in burning sprays, is sensibly affected by the number of flamelet domains used to describe the evolution of the overall fuel injected [28, 45, 14]. Hence, for the sake of completeness, it was chosen to investigate if the performances of RIF model can be improved by using multiple flamelet domains.

This assessment was performed for both turbulence models in the SSEp07b injection timing, with an imposed spray spreading angle of 10°, as in the previous section it showed better agreement with the experimental results. Multiple simulations were performed in this testing condition, where the number of flamelet domains used to model the main-injection event was progressively increased. A single-flamelet model was still used for the pilot injection, as increasing the number of domains for this injection event was not expected to improve the results of the simulations, due to the following reasons:

- Duration of pilot injection is extremely short and the mass introduced is quite small, which means that the flamelet from pilot injection covers a relatively small portion of the overall CFD volume. Therefore, small spacial variations of the scalar dissipation rate are expected over the flamelet volume;
- The long ignition delay compared to the injection duration suggests that most of the fuel is already evaporated and partially premixed at the onset of combustion. Therefore, it is expected that most of the fuel from pilot injection ignites simultaneously, with limited flame diffusion;
- As fuel ignites significantly after the end of pilot injection, flame stabilization phenomenon does not take place during pilot combustion.

Figures 4.36 and 4.37 show the impact of the number of flamelet domains used during main injection on the pressure trace, aHRR curve, and its cumulated, with the standard k-ε turbulence model and its RNG variant respectively. The graphs compare the results with one, six and twenty flamelets. The number of domains was not further increased, as the simulations would have required excessively long computational time[3].

[3]Simulations with 20 flamelet domains required nearly 4 days, running in parallel on a 8 dedicated processors Intel® Xeon® CPU E5-2630 v3 @ 2.40GHz.

It can be noticed that the standard k-ε model does not show any remarkable change when number of flamelet domains is increased. Differently, when turbulence is modeled with the RNG k-ε instead, some sensitivity is observed in the region of maximum aHRR, i.e., during mixing-controlled stage of combustion.

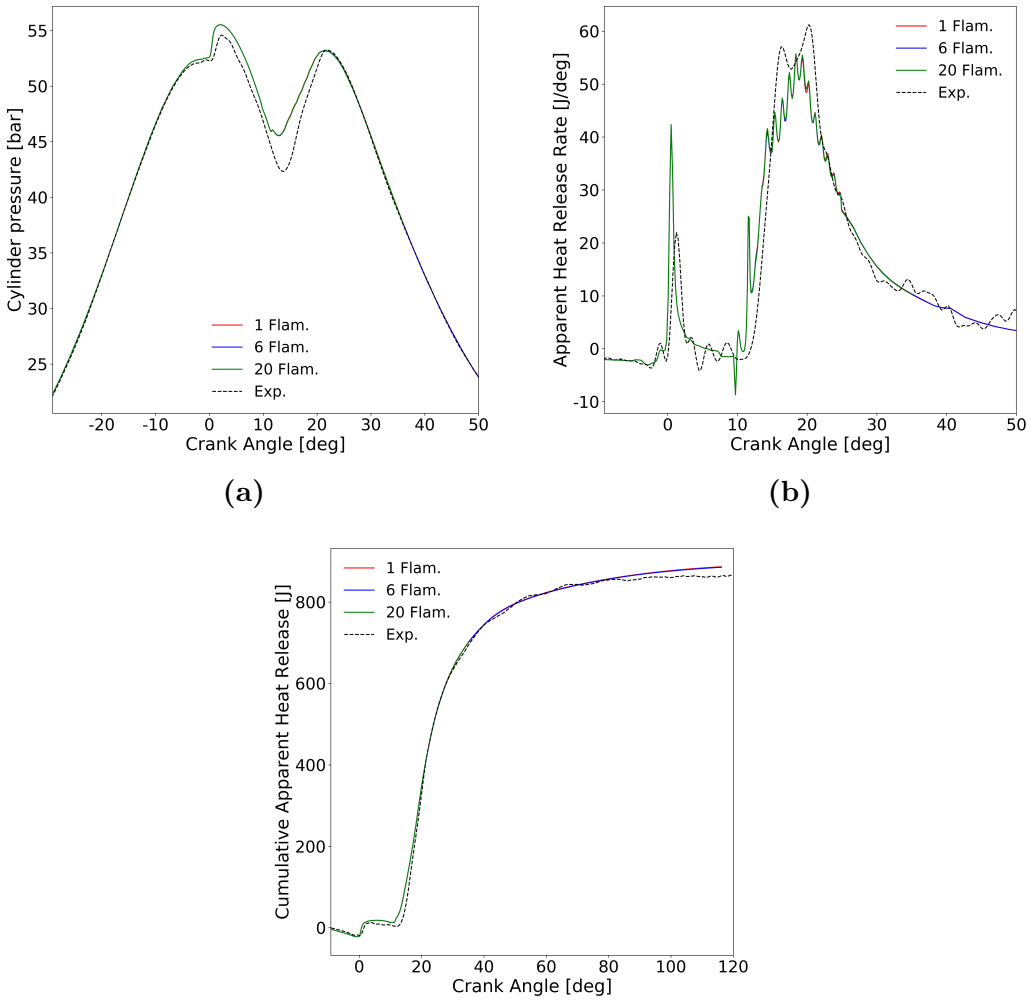

Figure 4.36: *Sensitivity of RIF model to the number of flamelet domains for fuel introduced during the main injection (standard k-ε model, SSEp07b testing case, 10° cone angle) - (a): In-cylinder pressure traces - (b): apparent heat release rate - (c): Cumulated aHRR.*

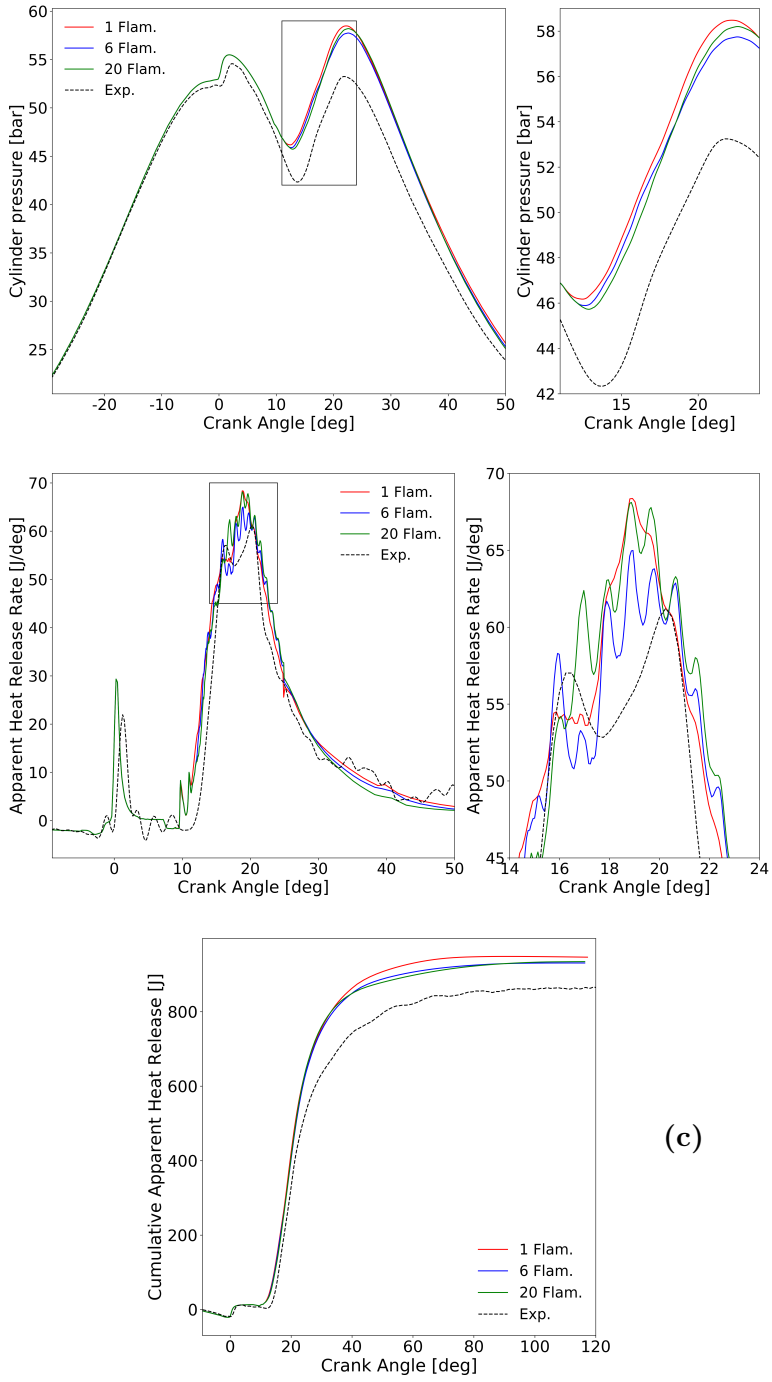

Figure 4.37: *Sensitivity of RIF model to the number of flamelet domains for fuel introduced during the main injection (RNG k-ε model, SSEp07b testing case, 10° cone angle) - (a): In-cylinder pressure traces - (b): apparent heat release rate - (c): Cumulated aHRR.*

As highlighted in figures 4.37a and 4.37b, the beginning of pressure rise is slightly postponed and the first of the two peaks of aHRR is smoothed out, while the second one is nearly unaffected. To better understand this behavior, figure 4.38 shows a comparison between the case with single-flamelet and 20 flamelets, in terms of the development of flame structure during the main injection.

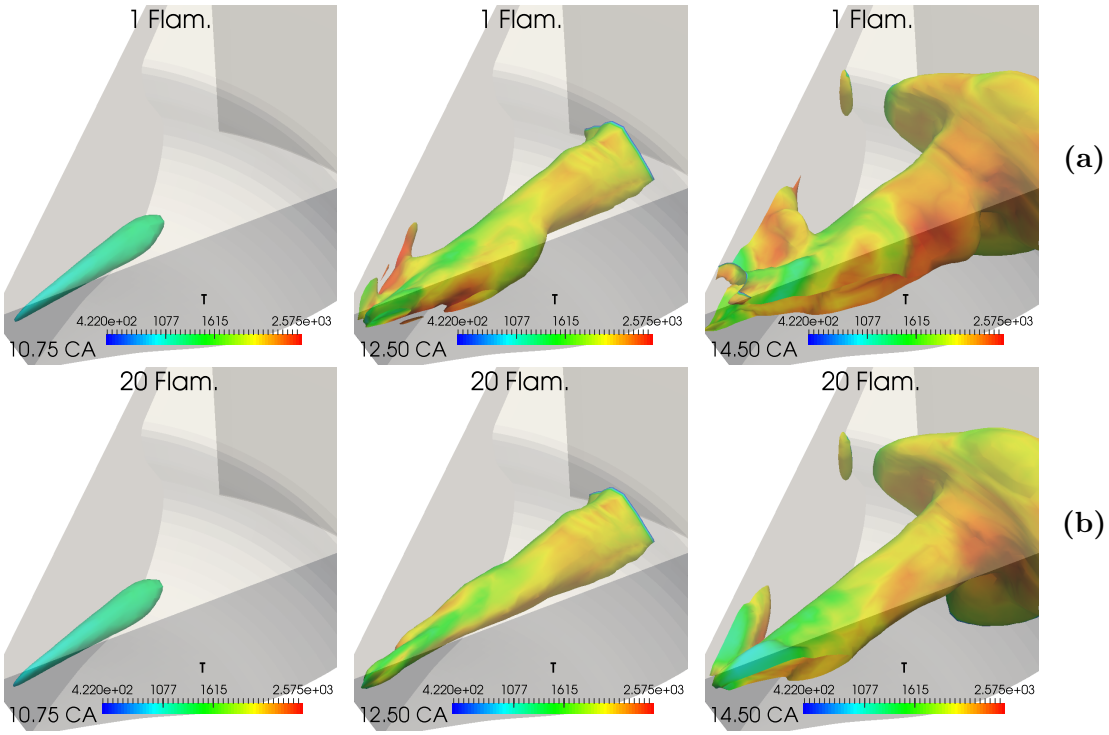

Figure 4.38: *Effect of the number of flamelet domains on the intensity of numerical instabilities with the RNG k-ϵ turbulence model. (a) and (b) show the development of the stoichiometric iso-surfaces during main injection, with coloring based on the temperature field, in case of 1 and 20 flamelet domains respectively.*

From these images, two main observations can be pointed out:

- Increasing the number of flamelets seems to be effective in reducing the numerical instabilities that are experienced when using the RNG k-ε turbulence model;
- Even with 20 flamelet domains, the stabilization phenomenon is not reproduced, as the flame is still really close to the injector orifice.

Diminishing of numerical instabilities is consistent with the mechanism at the origin this phenomenon that was proposed in section 4.2. Even thought flame

stabilization is not predicted, combustion seems to be partially inhibited at the very root of the fuel spray, probably thanks to the capability of multiple flamelets to account on the locally high scalar dissipation rate. Therefore, air-fuel mixture burns and expands more gradually, inducing lower perturbations in the mean-velocity field in the region close to the injector.

As the overall shape of the aHRR curve and its maximum value remain nearly unchanged with diminishing of the intensity of numerical instabilities, it can be deduced that their impact on the overall combustion dynamics is limited to the additional peak in aHRR. Hence, even though numerical instabilities are present, the results of single-flamelet simulations can be considered reliable in terms of overall combustion dynamics.

To understand the reasons why flame stabilization is not predicted even splitting the main injection among 20 flamelet domains, it should be reminded that when a new flamelet domain is generated, its temperature and composition in the Z-space are initialized by cloning the state of the previous one. This choice is mainly driven by the following requirements:

1. Prediction of the in-cylinder pressure trace;
2. Correct description of the flame structure (lift-off);
3. Limitation of the overall computational load, as a consequence of increasing the number of flamelet domains.

Initializing the flamelets with the temperature and composition of the unburned gases would lead to good description of the stabilized flame, but aHRR curve would experience several spikes during mixing-controlled combustion due to repeated self-ignition of flamelets, which is non-physical. To allow a correct prediction of both flame structure and pressure trace, a really high number of flamelets would be required. On the other hand, cloning the previous flamelet would mitigate these oscillations, but it requires that the new flamelets are introduced before ignition of the previous one, to have independent development of each flamelet.

However, due to the interaction with the hot gases from pilot combustion, the fuel introduced during main injection experiences sensibly shorter ignition delay, as shown in figure 4.39a. Hence, even with 20 flamelet domains, the time-span between generation of two consecutive flamelets is not short enough, and the new domains are initialized when the previous one is already ignited (Fig. 4.39b). According to these results, it can be presumed that the number of domains should

be almost doubled, to have initialization of the second flamelet before ignition of the first one.

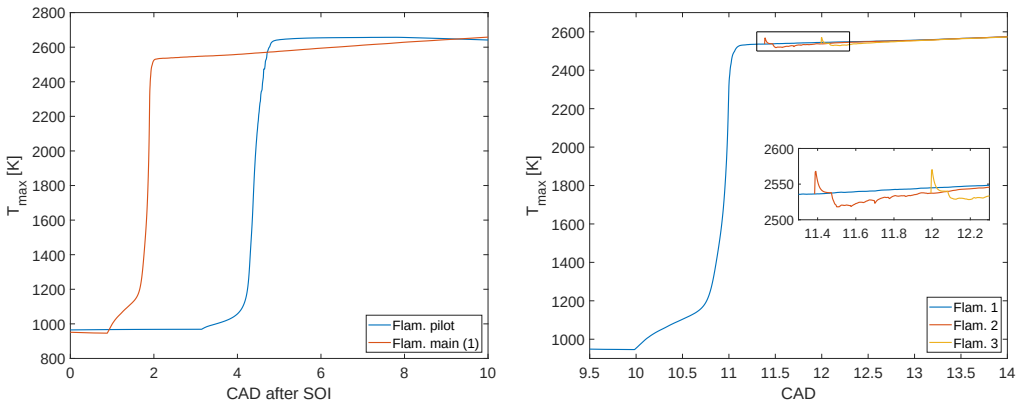

(a) **(b)**

Figure 4.39: *Maximum temperature in flamelet domains - (a): comparison between flamelets of pilot and main injection (first one), phased with respect their SOIs, to highlight their ignition delay - (b): behavior of the first three flamelets introduced during main injection.*

Moreover, there is another aspect that could compromise the capability of the combustion model to predict flame stabilization with the current simulation setup. As previously mentioned, when setting up the simulation with the mRIF combustion model, the following conflicting requirements were to be met in terms of flamelet-to-flamelet interaction:

- To correctly predict ignition delay during main injection, it is necessary to consider the interaction of the fuel from main injection with the cloud of hot gases generated during main injection [12];
- Isolated-spray simulations showed that flame stabilization phenomenon can be predicted by mRIF model only if interaction among flamelet domains is not taken into account [44].

Therefore, it was chosen to allow heat and mass transfer due to turbulent mixing only among overlapping flamelets associated to distinct injection events, as it was presumed to be a fair trade-off among these two opposing requirements.

However, even though flamelet domains associated with main injection do not directly interact among each other, the presence of the flamelet from pilot injection could potentially induce indirect heat and mass transfer among them. Figure 4.40 shows a schematic of this process:

1. At the beginning of main injection, heat is transferred due to turbulent mixing from the flamelet of the pilot injection to the first one of the main injection, thus promoting its ignition (Fig. 4.40a);

2. Once the first flamelet of main injection reaches the stoichiometric flame temperature, the direction of heat flow among the two flamelets is reversed, as almost all of the fuel from pilot injection is expected to be burnt, and some heat was previously lost during flamelet-to-flamelet interaction;

3. When the flamelet of pilot injection starts overlapping also with other flamelets from the main injection, they start exchanging heat and mass due to turbulent mixing. Therefore, as described by the schematic in figure 4.40b, the flamelet of pilot injection allows indirect transfer of heat and mass between those of main injection.

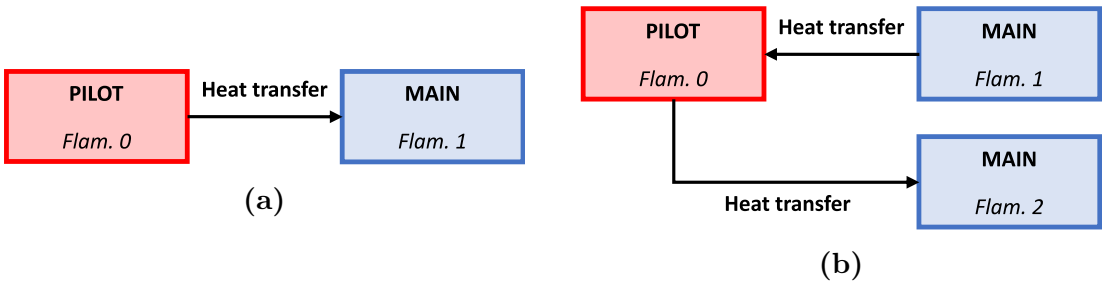

Figure 4.40: *Schematics of indirect interaction between flamelets of main injection - (a): At the beginning of main injection, heat is transfered from the flamelet of pilot injection to the first one of main injection, promoting its ignition - (b): After ignition of main injection, heat flow changes direction as fuel combustion starts in flamelet 1, and the flamelet of pilot injection allows indirect transfer of heat and mass between flamelets of main injection.*

However, the importance of this phenomenon in preventing capability of predicting flame stabilization could not be quantified in this work, as the new flamelets already ignited due to the temperature field initialization. However, it is known that in the Attack interaction model, the intensity of mixing among two flamelets is proportional to their level of overlapping [44, 12]. Therefore, it can be deduced that the intensity of indirect interaction ($Q_{i,j}$) induced by flamelet 0 among two generic flamelets i and j will be proportional to the product of their markers:

$$Q_{i,j} \propto M_0 \cdot M_i \cdot M_j$$

Figure 4.41 gives a measure of this product, for the first two flamelets of main injection, with increasing magnitude for coloring moving from blue to red. From this figure it can be deduced that this indirect-interaction effect could have a significant impact on capability to predict flame stabilization, as it is expected to have the highest intensity close to the region of stoichiometric air-fuel mixture.

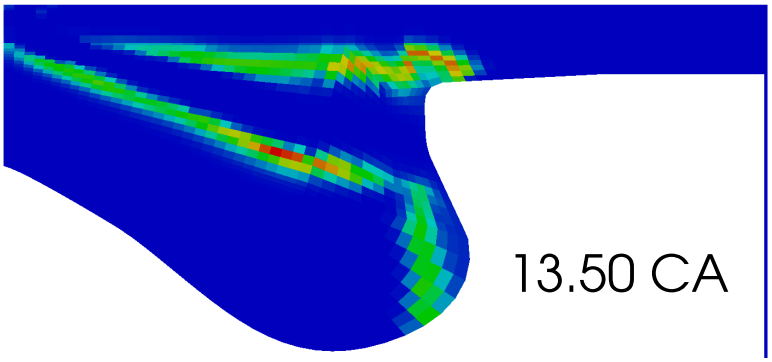

Figure 4.41: *Qualitative measure of the product $M_0 \cdot M_1 \cdot M_2$, during main injection, on a vertical cross section. Magnitude of the product increases with coloring moving from blue to red.*

The importance of this indirect-interaction mechanism should be further investigated in future works, along with possible modifications to the flamelet-to-flamelet interaction model to prevent this issue (for example, inhibition of interaction after ignition of the first flamelet, as it is required only to describe the beginning of main combustion).

Chapter 5

Conclusions and future work

In the present thesis, an extensive investigation was performed to establish the impact of turbulence and combustion modeling on describing the combustion process in mixing-controlled Diesel combustion, with a multiple-injection strategy. Specifically, turbulence was modeled with the standard k-ε turbulence closure and its RNG variant, while combustion was described through the Representative Interactive Flamelet model and the Well-Mixed model with off-line tabulation of chemical kinetics.

The setup of the simulations was based on the small-bore, light-duty, optical Diesel engine of Sandia National Laboratiories, for which a wide and well-documented experimental database is available on the Engine Combustion Network website [2]. The tested conditions were a part load, mid-range, conventional Diesel combustion mode, with a split-injection strategy, for three different injection timings. Validations were performed in terms of in-cylinder pressure traces and apparent heat release rate.

The engine geometrical parameters had to be adapted, due to the non negligible compressibility of the piston-connecting rod assembly. To this end, a tuning methodology was proposed, which allowed to fit the experimental in-cylinder pressure trace.

First of all, the effect of each model on the combustion dynamics were deeply analyzed in a baseline testing condition, to identify their peculiarities, and their performances in describing the combustion dynamics have been compared. Then, they were tested in several operating conditions, to assess their sensitivity to the injection timing and the spray spreading angle imposed at the outlet from injector orifice. Moreover, for the RIF combustion model, the sensitivity with respect to the number of flamelet domains used to describe main fuel injection was investigated.

From the analyses of chapter 4, the following main results were obtained:

- Both combustion models showed discrete capability to describe the overall combustion process, in the early and intermediate injection timing. In the late injection timing the RIF model performed rather poorly, due to the high degree of premixed combustion with such long ignition delay, which cannot be described by this combustion model;
- The inhibition of the reaction rate in fuel-rich mixture regions with the TWM combustion model showed to be sensibly detrimental during pilot combustion, probably due to the small injected mass and long ignition delay, which often led to misfire or sensible under-predicted peak of aHRR;
- It was showed that to correctly predict the ramp of aHRR during main injection, and its double-peak shape, the combustion model should be capable of describing the flame propagation in the premixed region and its stabilization. Therefore, this behavior could be reproduced only by the TWM model, which captured the first peak of aHRR;
- The standard k-ε model experienced negligible sensitivity with respect to injection timing and spray spreading angle, as a consequence to the strong dispersion of turbulent kinetic energy from the spray axis predicted by this model. This proved the poor performances of this model in describing shear flows;
- Even with multiple flamelet domains, the RIF combustion model could not predict flame stabilization during the main injection event, as a consequence of the really short ignition delay of the main combustion.

The overall best results were obtained with the combination of the RNG k-ε turbulence model and the RIF combustion model, with a 10° spray spreading angle. However, some issues due to numerical instabilities were observed with these two models; the origin of this phenomenon was investigated, and it was deduced that their impact on the overall combustion dynamics should be marginal.

In conclusion, this study showed that to correctly describe the combustion dynamics, and the impact of design choices (injection timing and geometry of piston bowl and injector nozzle), it is required to correctly predict the mean-flow and turbulence fields in the spray region, and being capable of describing premixed flame propagation. Moreover, the RIF model showed higher sensitivity with respect to changes in the flow field, suggesting that accounting on turbulence-chemistry

interaction is required to correctly predict aHRR in mixing-controlled combustion. Therefore, future studies should focus on development and investigation of combustion models including all of these aspects.

Moreover, in this study several assumptions were made in the case setup, and further studies should be performed to investigate the following aspects:

- Quantification of the error introduced by modeling the fuel with n-heptane, especially in the late-injection condition, which was shown to have differences in ignition and combustion properties from the real fuel, with lowering of the bulk-gas temperature [21];
- Consolidation of the results through full-cycle simulations, as it was shown that the sector-mesh approach has limitations in describing the evolution of the swirl-vortex and does not account on jet-to-jet differences [25];
- Investigations should be performed also in terms of capability to predict formation of pollutants, such as NOx and particulate matter, as it is among the most relevant aspects in development of next-generation internal combustion engines.

Bibliography

[1] 2019 outlook for energy: A perspective to 2040, exxonmobil. https://corporate.exxonmobil.com/-/media/Global/Files/outlook-for-energy/2019-Outlook-for-Energy_v4.pdf. Accessed: 08/06/2021.

[2] Engine combustion network, piston bowl geometry study. https://ecn.sandia.gov/engines/small-bore-diesel-engine/experimental-data/piston-bowl-geometry-study/. Accessed: 08/06/2021.

[3] Openfoam website. https://www.openfoam.com/. Accessed: 08/06/2021.

[4] Comolli A. Cfd modeling of diesel combustion with tabulated kinetics based on homogeneous reactor assumption. Master's thesis, Politecnico di Milano, Piazza Leonardo da Vinci, 32, Milano, Italy, 4 2017. Online: http://hdl.handle.net/10589/139901.

[5] Maghbouli A., Lucchini T., D'Errico G., and Onorati A. Effects of grid alignment on modeling the spray and mixing process in direct injection diesel engines under non-reacting operating conditions. *Applied Thermal Engineering*, 91:901–912, 2015.

[6] Mcbride B., Gordon S., and Martin Reno A. Coefficients for calculating thermodynamic and transport properties of individual species. 1993.

[7] Petersen B., Ekoto I., and Miles P. An investigation into the effects of fuel properties and engine load on uhc and co emissions from a light-duty optical diesel engine operating in a partially premixed combustion regime. *SAE International Journal of Engines*, 3:38–55, 05 2010. DOI: 10.4271/2010-01-1470.

[8] Pope S. B. *Turbulent Flows*. Cambridge University Press, 2000. DOI: 10.1017/CBO9780511840531.

[9] Wang B.-L., Miles P., Reitz R. D., Han Z., and Petersen B. Assessment of rng turbulence modeling and the development of a generalized rng closure model. *SAE 2011 World Congress and Exhibition*, 04 2011. DOI: 10.4271/2011-01-0829.

[10] Angelberger C., Poinsot T., and Delhay B. Improving near-wall combustion and wall heat transfer modeling in si engine computations. 1997.

[11] Bae C. and Kim J. Alternative fuels for internal combustion engines. *Proceedings of the Combustion Institute*, 36(3):3389–3413, 2017. Online: `https://www.sciencedirect.com/science/article/pii/S1540748916304850`, DOI: https://doi.org/10.1016/j.proci.2016.09.009.

[12] Felsch C., Gauding M., Hasse C., Vogel S., and Peters N. An extended flamelet model for multiple injections in di diesel engines. *Proceedings of the Combustion Institute*, 32(2):2775–2783, 2009. Online: `https://www.sciencedirect.com/science/article/pii/S1540748908002538` , DOI: https://doi.org/10.1016/j.proci.2008.05.053.

[13] Sahoo D., Miles P., Trost J., and Leipertz A. The impact of fuel mass, injection pressure, ambient temperature, and swirl ratio on the mixture preparation of a pilot injection. *SAE International Journal of Engines*, 6:1716–1730, 05 2013. DOI: 10.4271/2013-24-0061.

[14] Santanu De, Avinash Agarwal, Swetaprovo Chaudhuri, and Swarnendu Sen. *Modeling and Simulation of Turbulent Combustion*. 12 2017. DOI: 10.1007/978-981-10-7410-3.

[15] Dec J. E. A conceptual model of dl diesel combustion based on laser-sheet imaging. *SAE Transactions*, 106:1319–1348, 1997.

[16] Brusiani F., Bianchi G. M., Falfari S., Onorati A., Lucchini T., and Di Gioia R. Influence of cylindrical, k, and ks diesel nozzle shape on the injector internal flow field and on the emerging spray characteristics. *SAE Technical Papers*, 1, 04 2014. DOI: 10.4271/2014-01-1428.

[17] Colban W. F., Kim D., Miles P. C., Oh S., Opat R., Krieger R., Foster D., Durrett R. P., and Gonzalez D. M. A. A detailed comparison of emissions and combustion performance between optical and metal single-cylinder diesel engines at low temperature combustion conditions. *SAE International Journal of Fuels and Lubricants*, 1(1):505–519, 2009.

[18] Dos Santos F. and Le Moyne L. Spray atomization models in engine applications, from correlations to direct numerical simulations. *Oil & Gas Science and Technology–Revue d'IFP Energies nouvelles*, 66, 09 2011. DOI: 10.2516/ogst/2011116.

[19] Perini F., Dempsey A., Reitz R. D., Sahoo D., Miles P., and Petersen B. A computational investigation of the effects of swirl ratio and injection pressure on wall heat transfer in a light-duty diesel engine. volume 2, 04 2013. DOI: 10.4271/2013-01-1105.

[20] Perini F., Miles P. C., and Reitz R. D. A comprehensive modeling study of in-cylinder fluid flows in a high-swirl, light-duty optical diesel engine. *Computers & Fluids*, 105:113–124, 2014. Online: `https://www.sciencedirect.com/science/article/pii/S004579301400348X`, DOI: https://doi.org/10.1016/j.compfluid.2014.09.011.

[21] Perini F., Sahoo D., Miles P., and Reitz R. D. Modeling the ignitability of a pilot injection for a diesel primary reference fuel: Impact of injection pressure, ambient temperature and injected mass. *SAE International Journal of Fuels and Lubricants*, 7:48–64, 04 2014. DOI: 10.4271/2014-01-1258.

[22] Perini F., Zha K., Busch S., Kurtz E., Peterson R. C., Warey A., and Reitz R. D. Piston geometry effects in a light-duty, swirl-supported diesel engine: Flow structure characterization. *International Journal of Engine Research*, 19(10):1079–1098, 2018. Online: `https://doi.org/10.1177/1468087417742572`, DOI: 10.1177/1468087417742572.

[23] Perini F., Zha K., Busch S., Miles P., and Reitz R. D. Principal component analysis and study of port-induced swirl structures in a light-duty optical diesel engine. In *SAE Technical Papers*, 04 2015. DOI: 10.4271/2015-01-1696.

[24] Perini F., Busch S., , and Reitz R. Comparison of linear, non-linear and generalized rng-based k-epsilon models for turbulent diesel engine flows. In *SAE Technical Papers*, 03 2017. DOI: 10.4271/2015-01-1696.

[25] Perini F., Busch S., Kurtz E., Warey A., Peterson R., and Reitz R. D. Limitations of sector mesh geometry and initial conditions to model flow and mixture formation in direct-injection diesel engines. In *SAE Technical Papers*, 04 2019. DOI: 10.4271/2019-01-0204.

[26] Perini F., Busch S., Zha K., Reitz R. D., and Kurtz E. Piston bowl geometry effects on combustion development in a high-speed light-duty diesel engine. In *SAE Technical Papers*, 09 2019. DOI: 10.4271/2019-24-0167.

[27] White F.M. *Viscous Fluid Flow. 3rd Edition.* McGraw-Hill, Boston, 2006.

[28] D'Errico G., Lucchini T., Onorati A., and Hardy G. Computational fluid dynamics modeling of combustion in heavy-duty diesel engines. *International Journal of Engine Research*, 16(1):112–124, 2015. Online: `https://doi.org/10.1177/1468087414561276`, DOI: 10.1177/1468087414561276.

[29] D'Errico G., Lucchini T., Contino F., Jangi M., and Bai X.-S. Comparison of well-mixed and multiple representative interactive flamelet approaches for diesel spray combustion modelling. *Combustion Theory and Modelling*, 18(1):65–88, 2014. Online: `https://doi.org/10.1080/13647830.2013.860238`, DOI: 10.1080/13647830.2013.860238.

[30] Ferrari G. *Motori a combustione interna.* Società editrice Esculapio, 2016.

[31] Kalghatgi G. Is it really the end of internal combustion engines and petroleum in transport? *Applied Energy*, 225, 05 2018. DOI: 10.1016/j.apenergy.2018.05.076.

[32] Litrico G., Puduppakkam K., Liang L., and Meeks E. Predicting the combustion behavior in a small-bore diesel engine. In *SAE Technical Papers*, 04 2021. DOI: https://doi.org/10.4271/2021-01-0508.

[33] Woschni G. A universally applicable equation for the instantaneous heat transfer coefficient in the internal combustion engine. *SAE Transactions*, 76:3065–3083, 1968. Online: `http://www.jstor.org/stable/44562845`.

[34] Barths H., Hasse C., and Peters N. Computational fluid dynamics modelling of non-premixed combustion in direct injection diesel engines. *International Journal of Engine Research*, 1(3):249–267, 2000. DOI: 10.1243/1468087001545164.

[35] Curran H.J., Gaffuri P., Pitz W.J., and Westbrook C.K. A comprehensive modeling study of n-heptane oxidation. *Combustion and Flame*, 114(1):149–177, 1998.

[36] Beale J. and Reitz R. D. Modeling spray atomization with the kelvin-helmholtz/rayleigh-taylor hybrid model. *Atomization and Sprays*, 9:623–650, 11 1999. DOI: 10.1615/AtomizSpr.v9.i6.40.

[37] Agarwal A. K. Biofuels (alcohols and biodiesel) applications as fuels for internal combustion engines. *Progress in Energy and Combustion Science*, 33(3):233–271, 2007. Online: `https://www.sciencedirect.com/science/article/pii/S0360128506000384`, DOI: https://doi.org/10.1016/j.pecs.2006.08.003.

[38] Zha K., Busch S., Warey A., Peterson R. C., and Kurtz E. A study of piston geometry effects on late-stage combustion in a light-duty optical diesel engine using combustion image velocimetry. *SAE International Journal of Engines*, 11(6):783–804, 2018. Online: `https://www.jstor.org/stable/26649130`.

[39] Zha K., Busch S., Miles P., Wijeyakulasuriya S., Mitra S., and Senecal P. Characterization of flow asymmetry during the compression stroke using swirl-plane piv in a light-duty optical diesel engine with the re-entrant piston bowl geometry. *SAE International Journal of Engines*, 8, 01 2015. DOI: 10.4271/2015-01-1699.

[40] Lešnik L., Kegl B., Torres-Jimenez E., and Cruz-Peragon F. Why we should invest further in the development of internal combustion engines for road applications. *Oil & Gas Science and Technology*, 75:56, 01 2020. DOI: 10.2516/ogst/2020051.

[41] Bianchi G. M., Cantore G., and Fontanesi S. Turbulence modelling in cfd simulation of ice intake flows: The discharge coefficient prediction. *SAE Transactions*, 111:1901–1918, 2002. Online: http://www.jstor.org/stable/44743206.

[42] A. Moiz, Som S., Bravo L., and Lee S.-Y. Experimental and numerical studies on combustion model selection for split injection spray combustion. In *SAE 2015 World Congress & Exhibition*. SAE International, apr 2015. ISSN: 0148-7191, Online: `https://doi.org/10.4271/2015-01-0374`.

[43] Nordin P. A. N. Complex chemistry modeling of diesel spray combustion. pages 1–55, 01 2001.

[44] Colombi P. Development and validation of a cfd model for combustion simulations in direct injection diesel engines based on detailed chemistry and the unsteady diffusion flamelet assumption. Master's thesis, Politecnico di Milano, Piazza Leonardo da Vinci, 32, Milano, Italy, 12 2012. Online: http://hdl.handle.net/10589/71852.

[45] Lakshminarayanan P. and Aghav Y. *Modelling Diesel Combustion*. Springer Netherlands, 2010. DOI: 10.1007/978-90-481-3885-2.

[46] Zhou Q., Lucchini T., D'Errico G., Maes N., Somers L.M.T., and Lu X. Computational modeling of diesel spray combustion with multiple injections. In *SAE Int. J. Adv. & Curr. Prac. in Mobility*, 04 2020. DOI: 10.4271/2020-01-1155.

[47] Busch S., Zha K., Kurtz E., Warey A., and Peterson R. Experimental and numerical studies of bowl geometry impacts on thermal efficiency in a light-duty diesel engine. In *SAE Technical Papers*, 04 2018. DOI: 10.4271/2018-01-0228.

[48] Busch S., Zha K., Perini F., Reitz R. D., Kurtz E., Warey A., and Peterson R. Bowl geometry effects on turbulent flow structure in a direct injection diesel engine. In *SAE Technical Papers*, 09 2018. DOI: 10.4271/2018-01-1794.

[49] Busch S. and Miles P. Parametric study of injection rates with solenoid injectors in an injection quantity and rate measuring device. *Journal of Engineering for Gas Turbines and Power-transactions of The Asme*, 137(10), 2014. DOI: https://doi.org/10.1115/1.4030095.

[50] Sazhin S. S. Advanced models of fuel droplet heating and evaporation. *Progress in Energy and Combustion Science*, 32(2):162–214, 2006.

[51] Singh S., Reitz R. D., and Musculus M. Comparison of the characteristic time (ctc), representative interactive flamelet (rif), and direct integration with detailed chemistry combustion models against optical diagnostic data for multi-mode combustion in a heavy-duty di diesel engine. *SAE Transactions*, 115:61–82, 2006.

[52] Som S., Ramirez A. I., Longman D. E., and Aggarwal S. K. Effect of nozzle orifice geometry on spray, combustion, and emission characteristics under diesel engine conditions. *Fuel*, 90(3):1267–1276, 2011. Online: `https://www.sciencedirect.com/science/article/pii/S0016236110005880`, DOI: https://doi.org/10.1016/j.fuel.2010.10.048.

[53] Tonini S., Gavaises M., and Theodorakakos A. Modelling of high-pressure dense diesel sprays with adaptive local grid refinement. *International Journal of Heat and Fluid Flow*, 29(2):427–448, 2008. Online: `https://www.sciencedirect.com/science/article/pii/S0142727X07001609`, DOI: https://doi.org/10.1016/j.ijheatfluidflow.2007.11.009.

[54] Lucchini T., D'Errico G., Onorati A., Frassoldati A., Stagni A., and Hardy G. Modeling non-premixed combustion using tabulated kinetics and different

fame structure assumptions. *SAE International Journal of Engines*, 10:593–607, 03 2017. DOI: 10.4271/2017-01-0556.

[55] Lucchini T., D'Errico G., and Ettorre D. Numerical investigation of the spray–mesh–turbulence interactions for high-pressure, evaporating sprays at engine conditions. *International Journal of Heat and Fluid Flow*, 32(1):285–297, 2011. Online: `https://www.sciencedirect.com/science/article/pii/S0142727X10001323`, DOI: https://doi.org/10.1016/j.ijheatfluidflow.2010.07.006.

[56] Aronsson U., Solaka H., Lequien G., Andersson O., and Johansson B. Analysis of errors in heat release calculations due to distortion of the in-cylinder volume trace from mechanical deformation in optical diesel engines. *SAE International Journal of Engines*, 5:1561–1570, 01 2012. DOI: 10.4271/2012-01-1604.

[57] Yakhot V. and Orszag S. A. Renormalization group analysis of turbulence. I - Basic theory. *Journal of Scientific Computing*, 1(1):3–51, January 1986.

[58] Yakhot V., Orszag S.A., Thangam S., Gatski T., and Speziale C. Development of turbulence models for shear flows by a double expansion technique. *Physics of Fluids A Fluid Dynamics*, 4, 08 1992.

[59] Ekoto I. W., Colban W. F., Miles P. C., Park S., Foster D. E., and Reitz R. D. Sources of uhc emissions from a light-duty diesel engine operating in a partially premixed combustion regime. *SAE International Journal of Engines*, 2(1):1265–1289, 2009.

[60] Han Z. and Reitz R. D. Turbulence modeling of internal combustion engines using rng k-ε models. *Combustion Science and Technology*, 106(4-6):267–295, 1995. DOI: 10.1080/00102209508907782.

Appendices

Appendix A

Computation of apparent heat release rate

To make comparisons in terms of thermodynamic performances between the experimental data and the results of simulations, it is necessary to estimate in the same way their heat release rates. Therefore, the apparent heat release rates, and their cumulated functions, were computed from the pressure traces through a simplified single-zone thermodynamic model. The instantaneous heat release rate can be expressed with respect to the wall heat-loss Q_w and the in-cylinder average pressure p_{cyl} through the first law of thermodynamics:

$$\frac{dQ_{hr}}{d\theta} = \frac{dQ_w}{d\theta} + \frac{\gamma p_{cyl} \frac{dV}{d\theta} + V \frac{dp_{cyl}}{d\theta}}{\gamma - 1} \tag{A.1}$$

Where$V$ is the instantaneous in-cylinder volume and θ is the crankshaft angular position. γ is the specific heat ratio, which is computed assuming the working fluid to be a perfect mixture of ideal gasses with constant composition (intake air), and computing the temperature-dependent constant-pressure specific heat capacity of each specie $c_{p,i}(T)$ thorough its polynomial expansion:

$$\begin{gathered} c_{p,i}(T) = \hat{A}_{0,i} + \hat{A}_{1,i}\ T + \hat{A}_{2,i}\ T^2 + \hat{A}_{3,i}\ T^3 + \hat{A}_{4,i}\ T^4 + \hat{A}_{5,i}\ T^5 \\ c_p = \sum_i (y_i c_{p,i}) \\ \gamma = \frac{c_p}{c_p - R^*} \end{gathered} \tag{A.2}$$

Where $\hat{A}_j$ are the NASA polynomial coefficients of each chemical specie [6] and R^* is the mass-specific gas constant of the mixture. The convective wall-heat loss is computed as follows:

$$\frac{dQ_w}{d\theta} = \frac{A_{cyl}h}{60 \cdot n}\left(T - T_w\right) \tag{A.3}$$

Where A_{cyl} is the crank angle dependent surface area. n is the engine speed expressed in rpm, T is the average in-cylinder temperature, computed through the ideal-gas law, and T_w is the wall temperature. The convective heat transfer coefficient h is computed through the Woschni's correlation [33]:

$$h = C_1 \cdot D^{-0.2} \cdot p_{cyl}^{0.8} \cdot T^{-0.53} \cdot u_w^{0.8} \tag{A.4}$$

Where D is the cylinder bore, while u_w is computed as follows:

$$u_w = \left(C_2 + 0.308R_s\right) u_m \tag{A.5}$$

Where u_m is the mean piston speed. In this work no tuning of the C_1 and C_2 coefficients were performed, since the aHRR curves were only required to compare the experimental and numerical results, and aiming to a quantitatively accurate computation of the heat released during combustion was out of the scope of this thesis. Therefore, the following "reasonable" values where used in this work:

$$\begin{aligned} C_1 &= 8 \\ C_2 &= 2.28 \end{aligned} \tag{A.6}$$